

Deciphering Biomass Fragmentation using Millisecond Micro-Reactor Kinetics

A DISSERTATION
SUBMITTED TO THE FACULTY OF
UNIVERSITY OF MINNESOTA
BY

SAURABH MADUSKAR

IN PARTIAL FULFILLMENT OF THE REQUIREMENTS
FOR THE DEGREE OF
DOCTOR OF PHILOSOPHY

Adviser: Paul J. Dauenhauer

MAY 2018

Acknowledgements

First and foremost, I would like to thank my advisor, Paul Dauenhauer, who guided me throughout my Ph.D. and provided mentorship in research and professional development. His excitement and creativity towards solving challenging problems motivated me to complete the research projects. The work culture in Dauenhauer research group helped me accomplish both professional and personal goals in my graduate life.

I would like to thank Dauenhauer group alumni Andrew Teixeira, Christoph Krumm, Alex Paulsen, Luke Williams for their support, mentoring, and guidance during initial years of my PhD. I would also like to thank my current lab mates Kristeen Joseph, Katherine Vinter, Omar Abdelrehman, Greg Fracas, Vineet Mallikal for their continued support and encouragement. I specially thank my batchmates Kristeen and Katie for baring with me throughout the long journey of graduate school.

I would like to thank the department of Chemical Engineering and Materials Science, University of Minnesota and the department of Chemical Engineering, University of Massachusetts Amherst for giving me an opportunity to work as a research assistant and graduate student with some of the brightest people I have known. I would like to thank the professors and mentors I have had at both the universities, continually igniting that spark of curiosity, forcing me to work harder.

Finally, I would like to thank my family, and friends; without their support, I undoubtedly would not have made it to this point today.

Dedication

This thesis is dedicated to my *aai*

Abstract

Pyrolytic conversion of lignocellulosic biomass utilizes high temperatures to thermally fragment biopolymers to volatile organic compounds. The complexity of the degradation process includes thousands of reactions through multiple phases occurring in less than a second. The underlying chemistry of lignocellulose decomposition has been studied for decades, and numerous conflicting mechanisms and kinetic models have been proposed. The fundamental science of biomass pyrolysis is still without detailed chemical kinetics and reaction models capable of describing the chemistry and transport in industrial reactors. The primary goal of this thesis was to develop mechanistic insights of biomass pyrolysis with the focus on fragmentation of cellulose using two novel microreactor systems, **a. Quantitative Carbon Detector (QCD) b. Pulse Heated Analysis of Solid Reactions (PHASR).**

Current research of complex chemical systems, including biomass pyrolysis, requires analysis of large analyte mixtures (>100 compounds). Quantification of each carbon-containing analyte by existing methods (flame ionization detection) requires extensive identification and calibration. An integrated microreactor system called the Quantitative Carbon Detector (QCD) for use with current gas chromatography techniques for calibration-free quantitation of analyte mixtures was designed. Combined heating, catalytic combustion, methanation and gas co-reactant mixing within a single modular reactor fully converts all analytes to methane (>99.9%) within a thermodynamic operable regime. Residence time distribution of the QCD reveals negligible loss in chromatographic resolution consistent with fine separation of complex mixtures including pyrolysis products.

The requirements are established for measuring the reaction kinetics of high temperature (>400 °C) biomass pyrolysis in the absence of heat and mass transfer limitations. Experimental techniques must heat and cool biomass samples sufficiently fast to elucidate the evolution of reaction products with time while also eliminating substantial reaction during the heating and cooling phases, preferably by measuring the temperature of the reacting biomass sample directly. These requirements were described with the

PHASR (Pulsed-Heated Analysis of Solid Reactions) technique and demonstrated by measuring the time-resolved evolution of six major chemical products from Loblolly pine pyrolysis over a temperature range of 400 °C to 500 °C. Differential kinetics of loblolly pine pyrolysis were measured to determine the apparent activation energy for the formation of six major product compounds including levoglucosan, furfural and 2-methoxyphenol.

Levoglucosan (LGA), a six-carbon oxygenate, is the most abundant primary product from cellulose pyrolysis with LGA yields reported over a wide range of 5–80 percent carbon (%C). In this study, the variation of the observed yield of LGA from cellulose pyrolysis was experimentally investigated. Cellulose pyrolysis experiments were conducted in two different reactors: the Frontier micropyrolyzer (2020-iS), and the pulse heated analysis of solid reactions (PHASR) system. The reactor configuration and experimental conditions including cellulose sample size were found to have a significant effect on the yield of LGA. Four different hypotheses were proposed and tested to evaluate the relationship of cellulose sample size and the observed LGA yield including (a) thermal promotion of LGA formation, (b) the crystallinity of cellulose samples, (c) secondary and vapor-phase reactions of LGA, and (d) the catalytic effect of melt-phase hydroxyl groups. Co-pyrolysis experiments of cellulose and fructose in the PHASR reactor presented indirect experimental evidence of previously postulated catalytic effects of hydroxyl groups in glycosidic bond cleavage for LGA formation in transport-limited reactor systems.

PHASR experiments were performed to measure apparent kinetic parameters of cellulose fragmentation. The LGA formation step was decoupled from the initiation reactions by identifying cellobiosan as a chemical surrogate for cellulose pyrolysis intermediate melt phase. Kinetics of LGA formation step was measured using $^{13}\text{C}_1$ cellobiosan samples to track the contribution of glucose monomer in cellobiosan. The activation energy E_a calculated from the slope of the Arrhenius plot was 26.9 ± 1.9 kcal/mol and the preexponential factor k_0 calculated from the intercept was $4.2 \times 10^7 \text{ sec}^{-1}$. These kinetic parameters were found to be lower than the corresponding values for the previously proposed mechanisms of LGA formation calculated from DFT studies indicating a possibility of new, catalyzed mechanism of LGA formation.

Contents

List of Tables	vii
List of Figures.....	viii
Chapter 1 Introduction.....	1
Chapter 2 Thesis Outline.....	4
2.1 Thesis Objectives	4
2.1.1 Novel reactor-analysis system	4
2.1.2 Mechanistic interpretations of experimental results	6
2.2 Thesis Scope	8
Chapter 3 Quantitative Carbon Detector	10
3.1 Introduction.....	10
3.2 QCD Design and Performance Evaluation	13
3.2.1 Mechanical Design.....	13
3.2.2 Evaluation of Thermodynamics of QCD	15
3.2.3 Evaluation of QCD Residence Time Distribution.	18
3.3 Application of QCD for Cellulose Pyrolysis	21
3.3.1 Comparison of GC-QCD and GC-FID.	22
3.3.2 QCD for Complex Mixtures.	25
Chapter 4 Pulse Heated Analysis of Solid Reactions (PHASR)	28
4.1 PHASR Design	28
4.2 PHASR Performance Evaluation	30
4.2.1 Small biomass sample length scale.....	30
4.2.2 Temperature measurement and thermal control.....	32
4.2.3 Temperature ramp during heating (i.e., heating rate).....	33
4.2.4 Online detection and Temperature ramp during cooling (cooling rate).....	37
4.2.5 Sweep Gas Flow Rate	45
Chapter 5 Kinetics of Biomass Pyrolysis	47
5.1 Experimental methods	47
5.1.1 Biomass Characterization	47
5.1.2 Sample Preparation	49
5.1.3 PHASR Experiments	49
5.2 Results.....	51

5.2.1	Pyrolysis Product Distribution	51
5.2.2	Effect of Biomass Particle Size.....	54
5.2.3	Time-Resolved Evolution of Pyrolysis Products	55
5.2.4	Apparent Kinetics for product formation.....	56
Chapter 6 Cellulose Fragmentation in PHASR		58
6.1	Levoglucosan yield from cellulose pyrolysis.....	59
6.2	Effect of Sample size on LGA yield	65
6.2.1	Hypothesis I: Thermal Promotion of LGA Formation.....	67
6.2.2	Hypothesis II: Crystallinity of Cellulose.....	70
6.2.3	Hypothesis III: Secondary and Gas-Phase Reactions	73
6.2.4	Hypothesis IV: Catalytic Promotion of LGA with Reactive Hydroxyl Groups	75
Chapter 7 Mechanism of Levoglucosan Formation.....		78
7.1	Overview of Cellulose Fragmentation	78
7.2	Experimental Methods	81
7.2.1	Sample Preparation.	81
7.2.2	PHASR kinetics of cellulose.....	85
7.2.3	Kinetics of $^{13}\text{C}_1$ cellobiosan	87
7.3	Results and Discussion	89
7.3.1	Apparent kinetics of cellulose pyrolysis	89
7.3.2	Intermediates from cellulose pyrolysis	94
7.3.3	$^{13}\text{C}_1$ Cellobiosan: a kinetic surrogate	95
7.3.4	Kinetics of $^{13}\text{C}_1$ LGA formation from $^{13}\text{C}_1$ Cellobiosan	98
Chapter 8 Conclusions.....		103
8.1	Future work.....	105
Chapter 9 Bibliography.....		107

List of Tables

Table 4-1 Pyrolysis Reactor Performance and Thermal Limitations.....	37
Table 4-2 Experimental conditions and reaction parameters used to calculate operating points.....	42
Table 4-3 Characteristics of High Temperature Biomass Pyrolysis Reactors	46
Table 5-1 Characterization of Loblolly Pine Biomass.....	48
Table 5-2 Product yields for parity plots in Figure 5-4A-B.....	55
Table 6-1 Compilation of reported LGA yield from cellulose pyrolysis.....	61
Table 6-2 Thickness of Cellulose Samples. Thickness of powder samples in Frontier ...	66

List of Figures

Figure 2-1 Composition of Lignocellulosic Biomass	5
Figure 3-1 Design & Integration of Quantitative Carbon Detector	12
Figure 3-2 Thermodynamic Regimes of Operable QCD Parameters	15
Figure 3-3 Residence Time Distributions in FID and QCD Detectors	19
Figure 3-4 Individual Compound Parity of QCD and Conventional FID Quantification.....	23
Figure 3-5 Collective Parity of QCD and Conventional FID Quantification	24
Figure 3-6 Response Factors of Conventional FID (Red) and QCD (Blue)	25
Figure 3-7 GC-QCD of Complex Mixtures Derived from Cellulose Pyrolysis.....	26
Figure 3-8 Conventional FID (red) and Polyarc QCD (blue) response factors for 14 silylated compounds	27
Figure 4-1 PHASR reactor diagram and method	28
Figure 4-2 Pyrolysis Transport Map	31
Figure 4-3 Kinetics of cellulose initiation.....	35
Figure 4-4 Required Heating Rate for Biomass Sample Pyrolysis	36
Figure 4-5 Disparity in time scales of polymer reactions and conventional analytical techniques	39
Figure 4-6 Design requirements for a coupled reactor-detector system	41
Figure 4-7 Cooling Rate Requirement of Kinetic Biomass Pyrolysis Reactor	44
Figure 5-1 PHASR Reactor: heating, temperature control and cooling at millisecond timescale .	50
Figure 5-2 Three dimensionally arranged GC-QCD/FID chromatograms	52
Figure 5-3 Time-resolved evolution of six major chemical products from Loblolly pine pyrolysis	53
Figure 5-4 Comparison of product distribution from pyrolysis with varying sample particle size	54
Figure 5-5 Arrhenius plots of six different products forming from pyrolysis of Loblolly pine	57
Figure 6-1 Reported Levoglucosan Yield from Cellulose Pyrolysis	60
Figure 6-2 Cellulose Sample Loading: Key Descriptor for Levoglucosan yield.....	67
Figure 6-3 Pyrolysis Temperature and LGA yield.....	69
Figure 6-4 Crystallinity of Cellulose and Cyclodextrin Samples	71
Figure 6-5 X-ray diffraction (XRD) spectrum of thin film cellulose samples and calculation of crystallinity index.....	72

Figure 6-6 Co-Pyrolysis of Cellulose and Levoglucosan	74
Figure 6-7 LGA Yield from Co-Pyrolysis of Cellulose and Small Oxygenates	76
Figure 7-1 Simplified Reaction Scheme for Cellulose Fragmentation	78
Figure 7-2 Synthesis of $^{13}\text{C}_1$ LGA from $^{13}\text{C}_1$ glucose	82
Figure 7-3 ^1H NMR of the sample.	82
Figure 7-4 ^{13}C NMR of the sample.	83
Figure 7-5 ^1H NMR of the sample provided by Omicron Biochemicals	84
Figure 7-6 ^{13}C NMR of the sample provided by Omicron Biochemicals.....	85
Figure 7-7 Schematic of PHASR-GC-polyarc/MS.....	86
Figure 7-8 Temperature profile of thin film samples of $^{13}\text{C}_1$ cellobiosan.....	88
Figure 7-9 Sample Chromatogram of cellulose pyrolysis through PHASR at 500 °C.	89
Figure 7-10 Millisecond-scaled evolution profile for LGA from cellulose at 400-500 °C at 50- 2000 milliseconds.	90
Figure 7-11 PHASR kinetics of α -cyclodextrin. Conversion of α -cyclodextrin at temperatures 385 to 505 °C.	92
Figure 7-12 Apparent kinetics of LGA formation	93
Figure 7-13 Anhydropolysaccharides: Surrogate for cellulose intermediate.....	95
Figure 7-14 Ion fragmentation pattern of LGA peak from cellobiosan fragmentation over 40 < m/z < 300.	96
Figure 7-15 Sample GC Chromatogram of LGA isotopic mixture.....	97
Figure 7-16 Parity plot validating MS-CI quantification method.....	98
Figure 7-17 Sample GC Chromatogram of $^{13}\text{C}_1$ Cellobiosan pyrolysis at 380C.....	99
Figure 7-18 Mass spec fragmentation pattern of the LGA isotopic mixture after pyrolysis of cellobiosan (top) and $^{13}\text{C}_1$ cellobiosan (bottom).	99
Figure 7-19 Arrhenius plot for the $^{13}\text{C}_1$ LGA formation from $^{13}\text{C}_1$ cellobiosan	100
Figure 7-20 Proposed Mechanisms of LGA formation from Cellobiosan.....	101

Chapter 1 Introduction

As global populations grow and living standards improve, the world faces the challenge of meeting rising energy demand which is expected to grow by 25% by the year 2040. Fossil fuels such as coal, petroleum, and natural gas are the major source of energy accounting for approximately 95 percent of the world's energy consumption. Dwindling reserves of fossil fuels and environmental impacts related to production and usage of fossil fuels have made the need for renewable feedstock and sustainable energy one of the major challenges in the world.

Biomass is a clean, renewable energy source that can be converted to transportation fuels and commodity chemicals. Research efforts have recently been intensified to find viable pathways for unlocking the vast energy reserves in biomass¹. Thermochemical conversion of biomass is an attractive process to make renewable fuels and chemicals^{2,3,4}. From high^{5,6} (>700 °C) to moderate⁷ (~500 °C) to low temperatures⁸ (<400 °C), lignocellulosic biomass can be gasified^{9,10}, pyrolyzed^{11,4} or torrefied^{12,13} for heat, liquids, gases, or solid fuels, respectively. Fast pyrolysis of biomass is one of the most promising approaches for production of liquid fuels^{7,14,15}. The International Energy Agency has a goal for biomass derived fuels, also termed as “biofuels”, to meet more than a quarter of world demand for transportation fuels by 2050 to reduce dependence on petroleum and coal¹⁶. In fast pyrolysis, solid biomass is heated up to high temperatures (400-600 °C) in the absence of oxygen to produce a short-lived intermediate liquid phase, which ultimately breaks down to form organic volatiles, permanent gases, and residual solid char^{17,18}. Vapour products are condensed to form bio-oil which can be upgraded catalytically to renewable liquid fuels or chemicals¹⁹.

Considering the difference between the prices of the raw material and that of the final products, there is a clear economic incentive to convert low value carbon (\$0.1/lb_m carbon) in biomass to high value carbon (\$0.5/lb_m carbon) in fuels and chemicals. Biomass fast pyrolysis has already been commercialized however, there is a great scope for development and optimization of different aspects of the technology. For example, very little is known about the underlying physical and chemical processes during the

transformation of solid biomass to liquid bio-oil. The knowledge of fundamental chemistry is necessary to develop micro-kinetic model for the pyrolysis process to tune the properties and stability of bio-oil.

The underlying chemistry of lignocellulose decomposition has been studied for decades, and numerous conflicting mechanisms and kinetic models have been proposed^{20,21,22,23,24}. The fundamental science of biomass pyrolysis is still without detailed chemical kinetics and reaction models capable of describing the chemistry and transport in industrial reactors. Additionally, the problem of determining detailed kinetics is compounded by the wide range of variability inherent in the composition of biomass feedstocks²⁵. In a recent evaluation of the key challenges of pyrolysis, Mettler et al. identified the primary challenge as a lack of understanding of the underlying chemistry of biopolymer decomposition²⁶. For example, there remains debate regarding the global pathways of cellulose decomposition between direct and indirect lumped mechanisms^{27,28}; even more debate continues on the specific chemical reaction mechanisms leading to volatile organic compounds from biopolymers^{29,30,31,32}.

The inability to determine the reaction chemistry and kinetics of biomass pyrolysis derives from the absence of advanced experimental techniques. Chemical mechanisms have traditionally been supported with kinetic evidence in the form of reaction rate expressions (i.e., reaction rate orders)³³, kinetic isotope effects^{34,35}, and comparison of measured apparent activation energies with computation³⁶. However, these measurements have until recently been unobtainable by current experimental methods. As previously stated²⁶, thermal decomposition of lignocellulose is a multiphase process with convoluted biopolymer chemistry, solid heat transfer³⁷, and organic compound diffusion. This transformation occurs on the time scale of milliseconds evolving hundreds of organic compounds, thereby excluding the use of conventional experimental reaction systems and associated analytical instruments.

To propel the continued development of pyrolysis models, new experimental techniques must be developed to analyze the kinetics of high temperature biomass pyrolysis. The techniques should overcome the challenges of measuring elemental reaction kinetics by deconvoluting competing transport processes and secondary reactions. The

kinetic parameters extracted from such techniques can be directly compared with the computational studies of much debated mechanisms of reactions involved.

Chapter 2 Thesis Outline

2.1 Thesis Objectives

There are two major objectives of this thesis, **a.** To develop and validate novel reactor-analytical system to analyze the complex, millisecond timescale chemical transformation during biomass transformation. **b.** To measure kinetics of biomass transformation and obtain mechanistic insight from the experimental data.

2.1.1 Novel reactor-analysis system

Lignocellulosic biomass has complex macromolecular structures which consist primarily of three interacting biopolymers namely cellulose, hemicellulose, and lignin. Cellulose, a straight chain polymer of glucose units with β -1-4 linkages, constitutes to about 40-60% of lignocellulosic biomass. Hemicellulose is a branched heteropolysaccharides comprising mainly of D-glucose, D-mannose, D-xylose, and L-arabinose. These two carbohydrate polymers interact with highly aromatic, partially oxygenated polymer of phenylpropane units called as lignin. The linkages between these polymers, also known as lignin-carbohydrate complexes, leads to the complex structure of biomass³⁸. Apart from these three, biomass also contains other polysaccharides such as extractives and pectin. Figure 2-1 Composition of Lignocellulosic Biomass Figure 2-1 shows a typical composition of lignocellulosic biomass with chemical structures of the three main biopolymers. During pyrolysis, these large biopolymers fragment to form hundreds of smaller molecules. These transformations occur in milliseconds time scale and involve solid-liquid, liquid-vapor interactions. The resultant mixture with hundreds of gaseous and vapor products, short lived intermediates at high temperatures pose a complex analytical challenge.

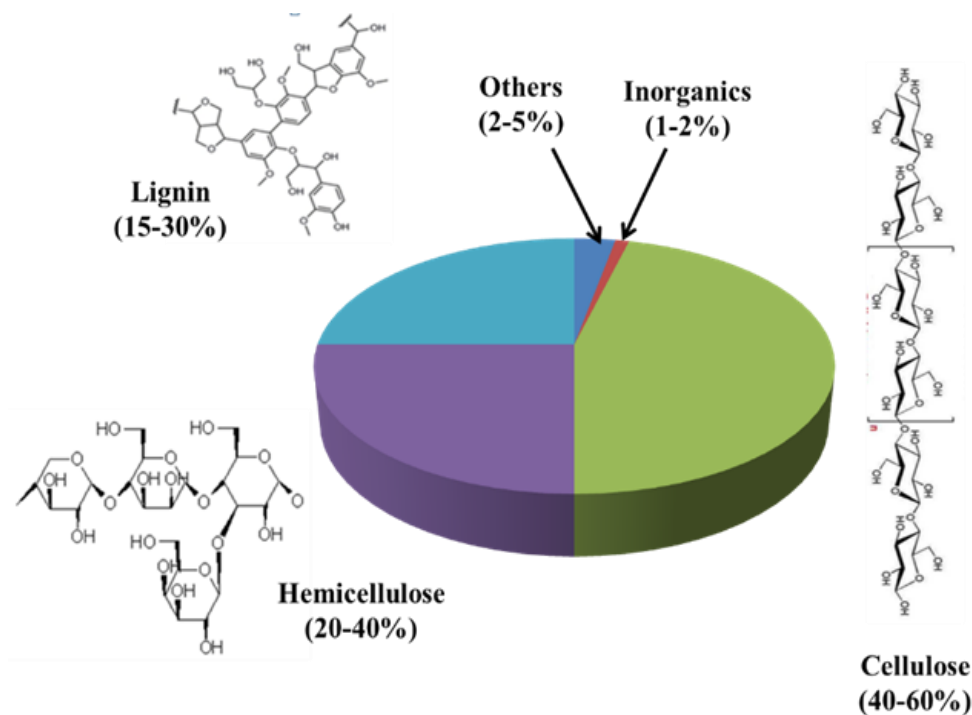


Figure 2-1 Composition of Lignocellulosic Biomass

Current analytical pyrolysis techniques include single-shot drop furnaces and thermogravimetric analyzers (TGA), which are commonly coupled with a gas chromatograph and mass spectrometer for quantification and identification of gas and volatile products. Quantification of unresolved, complex mixture of pyrolysis product using gas chromatography is typically resource expensive. Each component present in the mixture needs to be identified and calibrated separately using the corresponding standards which need to be purchases, isolated or synthesized.

The conventional techniques provide useful product compositions at 100% biomass conversion but have limited potential for evaluating the intrinsic kinetics of high temperature chemistry. Even with decades of research, the timescales for the hundreds of reactions that transform biomass to products have not been experimentally measured. Thermogravimetric analysis^{39,40} (TGA) measures the weight change of a biomass sample exposed to a temperature ramp. However, the

maximum ramp rate less than 200°C /min limits the TGA method to only low temperature conditions. Alternative techniques including the CDS Pyroprobe^{TM,41,42,43,44}, the Frontier Micropyrolyzer^{TM,45,46,47,48}, and the wire-mesh reactor^{49,50,51} overcome this limitation by enhancing the heating rate. Biomass particles exposed to a heated chamber, wire-mesh, or tube are rapidly heated resulting in particle decomposition and complete conversion to organic vapors, gases, and solid char product. Additionally, the biomass samples analyzed in the conventional reactor systems are generally in the millimeter length scale and have temperature and concentration gradient due to disparity in the heat and mass transfer rate versus the reaction rate in the reacting sample. The temperature measurement and control are also not capable enough to capture the thermal profile accurately. Recently, Mettler et al developed a new technique called thin film pyrolysis, in which a micrometer scale ‘thin-film samples’ are prepared by evaporative deposition method⁵². In thin film samples, the heat and mass transport rates are high enough to yield isothermal, reaction kinetics limited experimental results. This approach identifies the impact of heating rate, reaction temperature and virgin composition on the product distribution, but the absence of temporal control and kinetic information inhibits mechanistic evaluation.

An order of magnitude disparity of the timescales between pyrolysis reactions (milliseconds), competing transport processes, and analytical systems (kilo seconds) along with the complexity in quantification necessitates development of novel reactor-analytical systems for kinetic measurements.

2.1.2 Mechanistic interpretations of experimental results

Cellulose pyrolysis is a complex process involving coupled reaction pathways. In 1970s, the first simplistic, lumped kinetic model describing cellulose decomposition known as, the Broido-Shafizadeh model, postulated three main chemical pathways to products referred to as chars (solids), volatiles or tars (condensable organics), and gases (non-condensable organics)⁵³ based on TGA kinetics data. Since then, through various experimental and theoretical analysis,

number of mechanisms have evolved providing additional details about formation of specific intermediates and products. However, there are number of contradictions in different mechanisms proposed.

Most of the existing kinetic models are based on TGA analysis. The TGA data is interpreted by either model-free or mode-fitting methods. In model-fitting kinetic parameters from a proposed mechanism are retro-fitted to the TGA data. In model-free method the activation energy dependency as a function of the conversion degree is evaluated without any previous knowledge of the reaction model. Many concerns and issues were raised on the aptitude of both these methods in determining reliable kinetic parameters. As explained before, TGA itself has experimental limitations of heating rate and temperature measurement to capture kinetic data at higher temperatures. Such shortcomings have led to some of the major questions about biomass pyrolysis unanswered. Even the first step of cellulose chain decomposition, glycosidic bond cleavage, is debated to be occurring via either heterolytic or homolytic bond cleavage. There is broad agreement that the major product of cellulose fast pyrolysis (400–600 °C) is the anhydrosugar levoglucosan (LGA), but it is not clear how LGA forms or why it is the major product. In addition, the formation mechanisms of furans and fragmentation products such as formic acid, which are observed in appreciable quantities, remain under debate. This level of uncertainty underscores the need for microscopic approaches to reveal molecular-level details of biomass pyrolysis chemistry.

2.2 Thesis Scope

This thesis is organized in nine chapters. Chapter three describes an integrated microreactor system called the Quantitative Carbon Detector (QCD) for use with current gas chromatography techniques for calibration-free quantification of analyte mixtures. The chapter is adapted from a paper published in *Lab on a chip* with contribution from co-author Andrew R. Teixeira⁵⁴. The chapter contains an exhaustive description of QCD design and performance evaluation. An experimental evidence of broad applications of QCD technique for carbon quantification for a wide range of species found in liquid-vapor mixtures such as bio-oil is also provided.

Chapter four establishes five requirements for measuring kinetics of biomass pyrolysis such as small sample length scale, temperature measurement and thermal control, temperature ramp during heating and cooling, online detection, and sweep gas flow rate. The performance of a novel kinetic reactor, PHASR (pulse-heated analysis of solid reactions) was compared with the conventional reactors based on the above five requirements. Chapter five outlines kinetic measurements of loblolly pine pyrolysis using PHASR/GC-QCD system. Differential kinetics of loblolly pine pyrolysis were evaluated to determine the apparent activation energy for the formation of six major product compounds including levoglucosan, furfural, and 2-methoxyphenol. Chapters four and five are adapted from a paper published in *ACS Sustainable chemistry and Engineering*⁵⁵.

Chapter six and seven focuses on cellulose fragmentation reactions. Cellulose is the major constituent of biomass and yields valuable products such as Levoglucosan (LGA). LGA, a six membered oxygenate, is the most abundant primary product from cellulose pyrolysis with yields reported over a wide range of 5 – 80 percent carbon. In chapter six, the variation of the observed yield of LGA from cellulose pyrolysis was experimentally investigated. The reactor configuration and experimental conditions including cellulose sample size were found to have a significant effect on the yield of LGA. Co-pyrolysis experiments of cellulose and fructose in the PHASR reactor presented indirect experimental evidence of previously postulated catalytic effects of

hydroxyl groups in glycosidic bond cleavage for LGA formation in transport-limited reactor systems. The chapter six is adapted from a paper published in *ACS Sustainable chemistry and Engineering*⁵⁶.

Chapter seven focuses on mechanistic understanding of LGA formation from cellulose pyrolysis. Apparent kinetics of LGA formation from cellulose were measured which corresponds to convoluted effect of series of reactions and catalysis occurring during the process. Surrogate molecule for cellulose pyrolysis intermediate was identified and used as a kinetic surrogate to understand the chemistry of formation of LGA. The kinetic parameters extracted from the analysis were compared with the corresponding values from computational studies.

Chapter eight summarizes the work presented in the thesis and discusses the future direction of the research.

Chapter 3 Quantitative Carbon Detector

3.1 Introduction

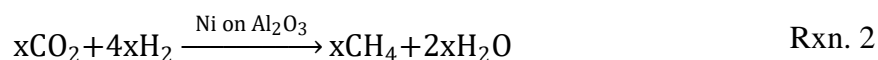
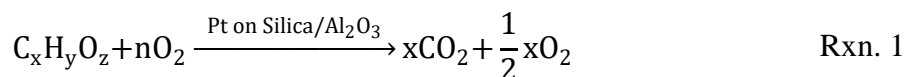
Quantification of unresolved complex mixtures (UCMs) is a major analysis obstacle in a number of emerging chemical and energy applications. For example, development of renewable, biomass-derived fuels has led to increasing complexity of liquid mixtures (10^2 - 10^3 compounds) as refinery feed stocks.^{57,58} Similarly, measured contaminants in wastewater treatment systems are lumped into total organic carbon content as a metric for water safety.⁵⁹ Upwards of 80 wastewater contaminants from pharmaceuticals such as estrogen are difficult to remove and require regular monitoring.⁶⁰ Biodegraded crude oil, present in soils⁶¹ and marine ecosystems,⁶² contains thousands of compounds.⁶³ Additionally, understanding of the health effects from tobacco pyrolysates requires analysis of hundreds of potentially harmful chemicals.⁶⁴ These diverse challenges require demanding analytical techniques that utilize time-consuming calibration; the lack of a robust, fast and reliable analytical technique necessitates new technology for analysis of UCMs.

In the case of fast pyrolysis of biomass, lignocellulosic biomass is thermochemically converted to produce a liquid intermediate called ‘bio-oil’ which can be integrated within the existing fuel infrastructure.^{7,65} Rapid thermal breakdown of lignocellulose occurs through high temperature heating, resulting in biopolymer degradation to a liquid mixture consisting of hundreds of oxygenated compounds with wide-ranging properties.^{1,58} Subsequent hydroprocessing produces reduced hydrocarbons which can be economically converted to liquid fuels including gasoline, diesel or jet fuel.^{66,67} Analytical quantification and identification of UCMs, such as those produced from pyrolysis and subsequent upgrading, remains a limiting research capability. Using the standard methods of gas chromatography / EI-CI mass spectrometry, characterizing this mixture requires identification and quantification of sufficient number of chemical species to close the carbon balance to >90 C%.^{68,69} This analytical approach relies on the ability to identify chemical species, which must then be purchased and injected for calibration of each individual chemical.^{52,70} When mixtures contain several hundred species, this methodology breaks down due to: (i) the

inability to effectively identify every species, (ii) limited potential for purchasing standards, and (iii) excessive time and resources needed for routinely calibrating hundreds of chemical vapors. For these reasons, quantification of bio-oil vapors for molecular-level study remains a significant challenge.

Previous chemical studies have demonstrated the potential of combined oxidation and methanation as a method for calibration-free carbon quantification of alkanes.⁷¹ Further development extended this method for oxygenates and phthalates.^{72,73} In this work, we develop a new design using tandem catalytic oxidation/methanation to provide calibration-free carbon quantification as a drop-in, fully-integrated microreactor. Thermodynamic calculations confirm operability at a wide range of conditions, identify fundamental detection limits, and extend the technology to a variety of analytes. Additionally, characterization of the device residence time distribution allows for optimal peak resolution for analysis of UCMs.

Utilization of an integrated microreactor (Figure 3-1) with additional gas flows controlled with an electronic pressure controller in a gas chromatograph allows for individual species to be converted as they exit a separating GC column by the following reactions: (a) complete oxidation ($X_C > 99.9\%$) converts organic carbon within vapors to CO_2 (Rxn. 1), and (b) the second microreactor converts all CO_2 ($X_{\text{CO}_2} > 99.9\%$) to methane (Rxn. 2).



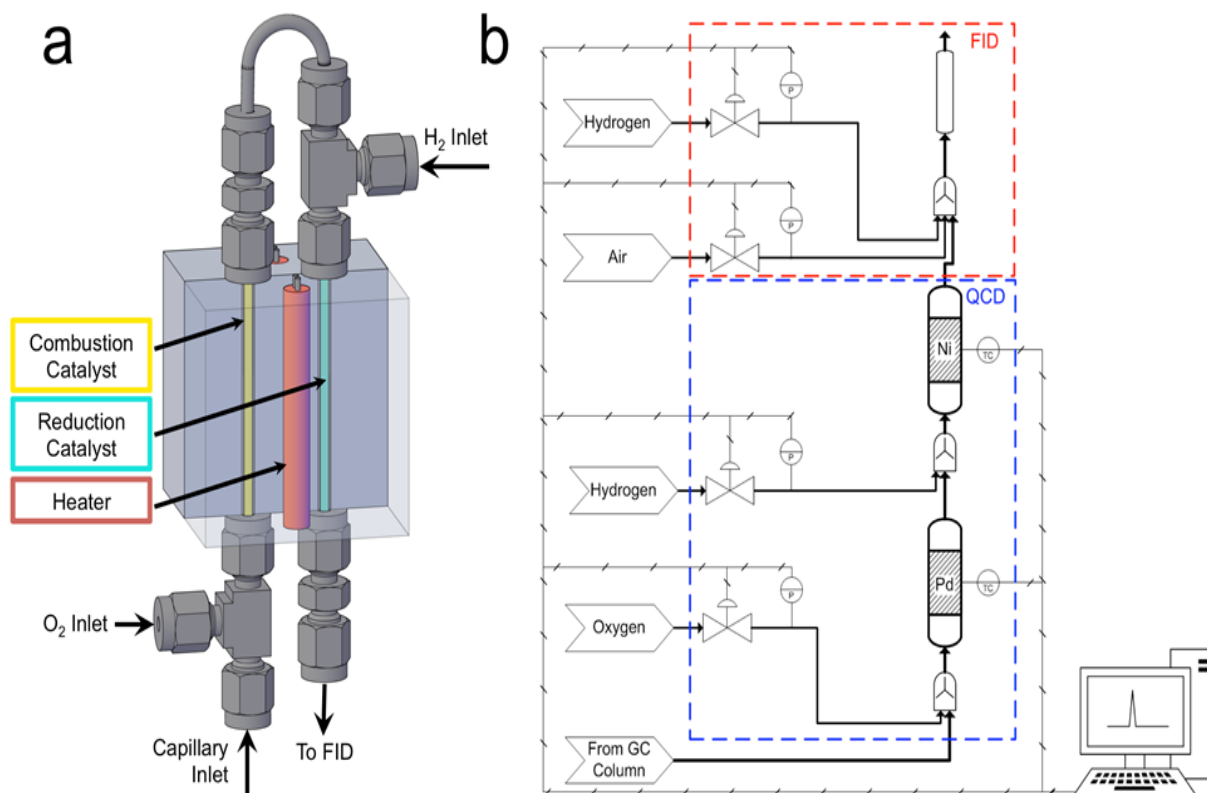


Figure 3-1 Design & Integration of Quantitative Carbon Detector

a) The QCD utilizes two integrated microreactors in series for combustion and methanation to convert 99.9% of hydrocarbons to methane. b) Miniaturization of the QCD allows for drop-in integration with existing analytical tools including gas chromatography.

By this method, all organic vapors exiting a packed/capillary column are converted to methane before entering the GC Flame Ionization Detector (FID); FID response per mole of carbon then remains constant for all organic species. Sufficiently robust system design ensures that all possible carbonaceous species are converted to CO₂, while the integrated reactor minimizes mixing and maintains resolution necessary for analytical separation. Here, we provide experimental evidence that the QCD technique provides broad capability for carbon quantification for a wide range of species found in liquid/vapor mixtures such as bio-oil.

3.2 QCD Design and Performance Evaluation

The QCD was designed for integration within existing gas chromatographs equipped with a capillary column and flame ionization detector (section 3.2.1). Feasibility of the QCD system to fully oxidize and methanate analytes (>99.9%) was shown via thermodynamic calculations (section 3.2.2). Residence time distribution experiments were conducted to demonstrate that the QCD technology does not interfere with chromatographic separation (section 3.2.3). Experiments demonstrated that the QCD output has identical carbon quantification capabilities to conventional FID-calibration methods. Finally, the QCD methodology was utilized in the pyrolysis of cellulose to demonstrate its capability for quantifying complex mixtures with high resolution.

3.2.1 Mechanical Design

The QCD consisted of an insulated, aluminum block (2 in. by 2 in. by 2 in.) with four cylindrical holes machined lengthwise (Figure 3-1). Two holes each contained a cylindrical, electrically-resistive heater (Omega Engineering PN CIR 3021, 100W), which heated the entire assembly to 500 °C. The two remaining holes housed catalytic reactor chambers comprised of 1/8" stainless steel tubing with 1/16" zero dead volume reducing union (Vici Valco PN ZRUF211) on either end. A fifth cylindrical hole was drilled to a depth of 1.0 inch at the center of the block for a thermocouple (Omega Engineering PN TC-GG-K-20-36). Temperature was controlled with an Omega CN7823 PID controller performing a feedback loop measuring the temperature within the heating block and triggering AC pulses (120 V) through a solid-state relay. The first catalytic reactor chamber was utilized for catalytic oxidation. 115 milligrams of 10% Pd/Alumina (Sigma-Aldrich #440086) was packed within the first catalytic reactor chamber. Prior to entering the reactor chamber, a 1/16" zero dead volume reducing tee (Vici Valco P/N# TCEF211) combined the capillary GC column effluent with flowing oxygen (to ensure complete oxidation). Effluent from the catalytic oxidation reactor chamber was transferred to the second catalytic reactor chamber for methanation via a 1/16"

stainless steel capillary transfer line. The transfer line connected to a reducing tee, which combined the effluent of the first catalytic reactor chamber with flowing hydrogen gas (to ensure complete methanation). The second catalytic reactor chamber was packed with 124 milligrams of Nickel catalyst (Agilent Technologies, P/N 5080-8761). Gases exited the second catalytic reaction chamber through a reducing union (VICI Valco PN ZRUF211) into a deactivated capillary column (8 inches long), which directed flow to the existing flame ionization detector (FID). Figure 3-1b includes a detailed schematic of the QCD system.

Implementation of the QCD within a gas chromatograph with an existing flame ionization detector (FID) required two supplementary gas flow lines (oxygen and hydrogen), as shown in Figure 3-1b. Oxygen flow was supplied to the QCD by an electronic pressure controller (EPC, Agilent PN 7890A). Excess oxygen served to ensure complete combustion of GC analytes. Total required oxygen gas flow to guarantee high yield of CO_2 (>99.9%) in the first catalytic reactor chamber of the QCD was determined by the thermodynamic calculations. Implementation of oxygen flow was achieved in the experimental system by varying the oxygen set pressure and measuring the resulting oxygen flow with a bubble column. Oxygen pressure was set in all experiments to maintain oxygen flow at 1.0 sccm.

Hydrogen gas flow was controlled by the existing EPC (Agilent PN 7890A), which adjusts the hydrogen gas pressure at the inlet to the QCD. Hydrogen gas serves two purposes: (i) promotes methanation of CO_2 to CH_4 , and (ii) converts excess O_2 from the combustion reactor to water. Total required hydrogen gas flow to guarantee high yield of methane (>99.9%) was determined by the thermodynamic calculations. Implementation of this flow was achieved in the experimental system by varying the hydrogen set pressure and measuring the resulting hydrogen flow with a bubble column. Hydrogen pressure was set in all experiments to maintain hydrogen flow at 10.0 sccm.

3.2.2 Evaluation of Thermodynamics of QCD

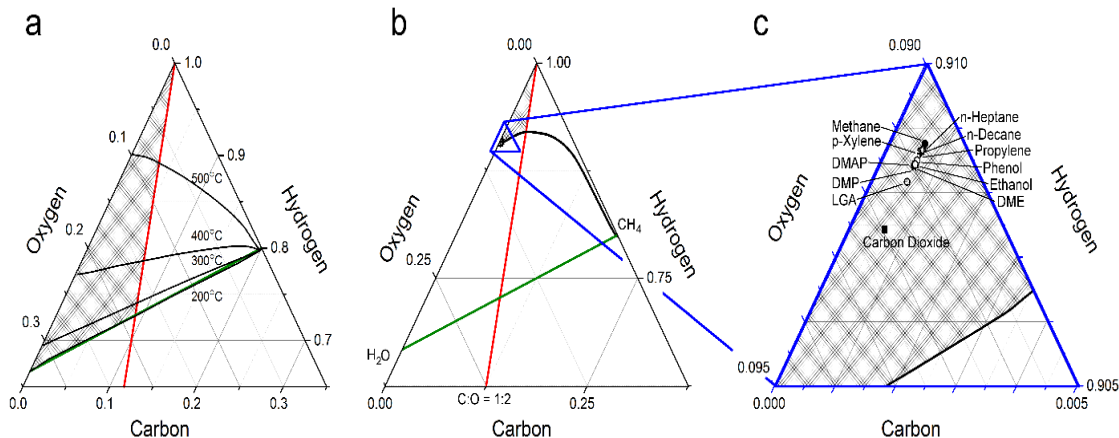


Figure 3-2 Thermodynamic Regimes of Operable QCD Parameters

a) Temperature dependence of thermodynamic feasibility for C:H:O ratios to achieve 99.9% conversion to methane. The shaded region envelops stoichiometric and thermodynamic bounds defining a region of QCD operability. b) At 500 °C, various compounds are plotted under dilute (He:C = 10) conditions. c) All compounds are within the operable region and are converted to methane under reaction conditions (inset).

Thermodynamic ternary maps shown in Figure 3-2 were generated using a Gibbs free energy minimization method within Aspen Plus 7.3. Calculations were performed to determine the amount of supplementary hydrogen flow needed to fully methanate the carbon from the injected sample. The stoichiometry from reactions 1 and 2 was defined as a constraint on the calculations, where the injected carbon was allowed to react with supplementary oxygen and hydrogen to form CO, CO₂, CH₄, H₂O, H₂, or O₂.



Calculations were performed at varying temperature for a fixed pressure of one atmosphere with the constraint of 99.9% conversion of carbon to methane. Property estimations were derived from the Peng-Robinson property method in ASPEN PLUS software, and all calculations were performed using the ‘design

specifications' function. The overall C:H:O ratios so obtained were plotted on ternary maps (Figure 3-2a).

Figure 3-2 depicts the thermodynamics of Rxn. 1, 2 and 3 in the presence of helium carrier gas. ASPEN PLUS calculations were repeated to simulate a helium-to-carbon molar ratio of 10:1 at 500 °C. The helium-to-carbon ratio was chosen to replicate a common injection volume (one microliter) such that the injected moles of carbon divided by the peak width yields a 1:10 ratio with the carrier gas molar flowrate. The same calculations were performed using the same helium-to-carbon ratio for 12 different compounds which are plotted in Figure 3-2.

Figure 3-2a depicts a C-H-O ternary plot, which describes the calculated conditions under which the QCD reactions are thermodynamically favorable; for complete detection and quantification, each analyte must achieve full conversion to methane (>99.9%) within the QCD. Four black lines, each representing a different reaction temperature, envelop the region in which full conversion to methane is achieved for any given combination of molecules at given C-H-O ratios. C-H-O ratios that fall above a line are thermodynamically predicted to achieve >99.9% conversion to methane at the corresponding temperature. In addition, colored lines are drawn to indicate the stoichiometric constraints of the combustion and methanation reactions. The red 'combustion line' indicates a carbon-to-oxygen ratio of one-to-two, which is a requirement for complete combustion. The green 'combustion/methanation line' is drawn between points representing methane and water, indicating the overall stoichiometric requirement of the two combined reactions. The shaded region of Figure 3-2a represents the C-H-O ratios which satisfy both thermodynamic requirements for methane conversion and stoichiometric constraints for the QCD reactions (combustion and methanation), thereby defining a region of operability (shaded, grey).

In Figure 3-2b, the 500 °C boundary from Figure 3-2a is modified to include helium carrier gas flow with a helium-to-carbon molar ratio of 10:1, representative of common operating conditions. The addition of inert carrier gas raises the curve and reduces the region of thermodynamic operability with respect to Figure 3-2a.

Finally, the C-H-O ratios of 12 compounds injected into the GC-QCD are plotted in Figure 3-2c. All 12 compounds exist within the thermodynamically possible regime under considered experimental conditions, indicating that all compounds should achieve high conversion to methane if the combined reactions of catalytic combustion and methane proceed to approach equilibrium.

Thermodynamic calculations predict that there exists a broad region of operability for the QCD across which analytes are completely converted to methane (>99.9). The results of these calculations were validated by the tests conducted to ensure complete conversion in the reactors. Additionally, the absence of catalyst deactivation within the QCD was confirmed by monitoring reactor conversion after 200 sample injections. Experiments were conducted to ensure complete oxidation/methanization and the absence of coking in the combustion and methanization reaction chambers. A range of oxygenated, aromatic, and alkyl compounds were used to simulate likely compounds present in unresolved complex mixtures (UCMs), including: n-heptane, methane, 2,6-dimethoxyphenol (DMP), and 3,4-dimethoxyacetophenone (DMAP). Coking in the combustion reaction chamber was tested by replacing the oxygen flow with an equivalent helium flow and injecting a sample of methane. After the methane peak eluted, the oxygen flow was turned back on. If any coking had occurred, the coke would have been combusted and an additional peak would have been observed. This was not the case, therefore coke was not forming in the combustion reaction chamber. To guarantee that combustion was reaching completion in the first reaction chamber, the flow of hydrogen to the second reaction chamber was replaced with helium and several different samples were injected. If combustion was complete, the injected sample would be converted to CO₂ and no peak would be observed. During tests, no peak was observed, confirming that combustion was indeed complete. The same reaction conditions as those used to test for complete combustion (i.e. replacing hydrogen flow with helium) were used to test for coking in the methanization reaction chamber. CO₂ was injected and enough time to allow CO₂ to exit the QCD had passed, the hydrogen flow was turned back on. No peak was observed,

indicating there was no coking in the reactor. Similarly, to test for complete methanization, separate samples of methane and CO₂ were injected. The two samples produced the same response, which confirmed that methanization was indeed complete.

3.2.3 Evaluation of QCD Residence Time Distribution.

Residence time distribution (RTD) analysis was carried out to verify that the QCD does not significantly reduce chromatographic peak resolution. A tracer of methane gas was injected as a pulse and the resulting detector response was measured with an FID. Equal amount of methane gas (0.5 ml) was injected into the system for four different configurations: (i) a base case with conventional FID only, (ii) QCD reactor with no catalyst packing and no supplementary oxygen or hydrogen, (iii) QCD reactor with catalyst packing and no supplementary oxygen or hydrogen, and (iv) QCD reactor with catalyst packing and oxygen and hydrogen flows. The variance of each RTD curve was calculated and used to characterize the effect of packing and supplementary flows on GC peak resolution. Variance was calculated by first determining the exit age distribution as a function of time (Equation 1).

$$E(t) = \frac{C(t)}{\int_0^{\infty} C(t)dt} \quad (1)$$

The age distribution was then used to calculate the average residence time for each system configuration (Equation 2).

$$\bar{t} = \int_0^{\infty} tE(t)dt \quad (2)$$

Equation 1 and 2 were then used to calculate the variance of each RTD curve (Equation 3).

$$\sigma^2 = \int_0^{\infty} (t - \bar{t})^2 E(t)dt \quad (3)$$

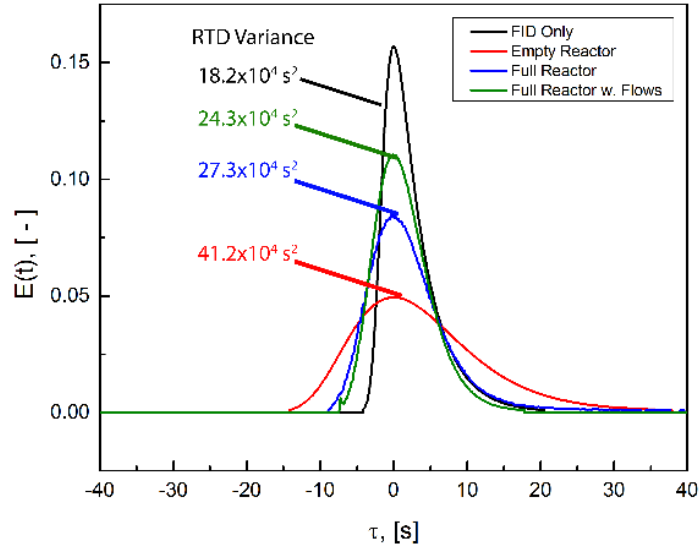


Figure 3-3 Residence Time Distributions in FID and QCD Detectors

RTD analysis shows minimal loss in peak resolution between GC-FID and GC-QCD.

Peak resolution of the QCD is enhanced by the addition of catalyst (red versus blue) and the addition of oxygen and hydrogen flows (blue versus green).

Design of the QCD results in negligible mixing or loss in peak resolution in comparison to a chromatogram obtained by conventional GC-FID. Figure 3-3 depicts the detected residence time distribution (RTD) from an injected pulse of methane for GC-FID and three different GC-QCD configurations. The conventional GC-FID system resulted in a sharp, narrow peak (black line) with variance of $18.2 \times 10^4 s^2$. The RTD obtained from the GC-QCD system with no catalyst (red line) resulted in a shallow, broad peak with an increased variance of $41.2 \times 10^4 s^2$. Introduction of catalyst into the QCD reactor (blue line) decreased the variance ($27.3 \times 10^4 s^2$), while supplementary oxygen and hydrogen flows (green line) further reduced the variance in RTD ($24.3 \times 10^4 s^2$).

RTD studies shown in Figure 3-3 verify that GC-QCD retains peak resolution comparable to GC-FID. Variance calculated from the GC-QCD peak is only slightly higher than that of the GC-FID system, indicating minimal loss in

chromatographic separation. Small values in variance indicate a sharp, narrow peak, which makes separation of complex mixtures less time consuming. In the case of the GC-QCD reactor absent catalyst packing, the variance was more than double the variance with conventional GC-FID, likely due to increased residence time and increased axial mixing within the catalyst reactor chambers. The addition of catalyst and supplementary flows reduces gas residence time and mitigates the effects of the QCD reactor on peak resolution.

3.3 Application of QCD for Cellulose Pyrolysis

The Quantitative Carbon Detector (QCD) is a modular carbon detection microreactor for direct integration with existing GC-FID systems, with a compact design that allows for installation within a GC oven. Modular design makes the catalytic reactor chambers interchangeable, allowing for additional applications such as oxygenate flame ionization detection (O-FID) to detect the moles of oxygen in a sample.⁷⁴ Characterization of the residence time distribution combined with thermodynamic calculation of regions of operability confirms the viability of the design. Response factors of conventional GC-FID and GC-QCD were compared to validate the ability of the QCD to reproduce FID results without prior calibration. Finally, a sample of bio-oil from cellulose pyrolysis was analyzed via GC-QCD to demonstrate negligible loss in chromatographic resolution of the QCD reactor with a complex mixture.

Fifteen chemicals were independently injected into the gas chromatograph splitless inlet at varying concentration (2.0 to 3.0 carbon-millimole per mL solution). Both the QCD and standard Agilent FID were used in separate trials to quantify injected compounds. Fifteen compounds were selected to represent a range of sizes, chemical compositions, and functionalities including: (i) methyl furan, furfural, and levoglucosan, which are representative of compounds derived from cellulose pyrolysis, (ii) carbon dioxide and acetol, which are representative of compounds derived from hemicellulose pyrolysis, (iii) phenol, 2,6-dimethoxyphenol (DMP), and 3,4-dimethoxyacetophenone (DMAP), which are representative of compounds derived from lignin pyrolysis, and (iv) methane, ethanol, dimethyl ether (DME), propylene, p-xylene, n-heptane, and n-decane, which are representative of compounds derived from petroleum processing.

The GC inlet was maintained at 250 °C (320 °C for levoglucosan injections) and 25 psi under splitless inlet conditions. The pressure was selected to achieve a column flow of approximately 1.0 mL/min. The inlet was connected to an HP-5 column (Agilent PN 19091J-102), which connected directly to the QCD. The oven temperature

was increased from 70 °C to 250 °C at a rate of 20 °C/min. Liquid samples were prepared in methanol or water to 5 wt% of the analyte with five injections ranging from 0.2-1.0 µl with an autosampler (Agilent PN 7693, Syringe PN G4513-8021). Gas samples were injected using two mass flow controllers (Brooks, PN 5850E) and a power supply with control module (Brooks, PN 0254). The concentration of analyte gas was controlled by varying the ratio of helium and analyte flow from the two controllers. The combined output from both mass flow controllers was injected into the GC inlet through a six-port switching valve (Vici Valco PN A26WT). Moles of injected compounds quantified by GC-QCD were compared with moles of injected compounds quantified by conventional GC-FID by generating calibration curves for each compound.

To demonstrate the capability of the QCD to analyze complex mixtures, a bio-oil sample from cellulose fast pyrolysis was injected into the GC-QCD system. Bio-oil samples were collected using an ablative fast pyrolysis reactor, where product vapors were collected in a water quench, as previously described.⁷⁵ Microcrystalline cellulose (FMC Biopolymer PN Lattice NT-200) was pyrolyzed under nitrogen flow at 500 °C. The quench was transferred to a 2 mL vial, and 1.0 µl was injected directly into the GC inlet.

3.3.1 Comparison of GC-QCD and GC-FID.

Figure 3-4 depicts parity plots comparing GC-QCD response to GC-FID response for all 15 selected compounds. Micromoles of carbon detected for both the GC-QCD and GC-FID are shown to be nearly identical for each of the identified compounds with the exception of carbon dioxide. While carbon dioxide was not detectable with GC-FID (and normally requires a second detector such as a thermal conductivity detector, TCD), detection within the GC-QCD occurs via conversion to methane. Additionally, carbon monoxide was also quantifiable using the GC-QCD, because it was converted to carbon dioxide within the first catalytic reactor chamber and subsequently converted to methane downstream. Figure 3-5 condenses the data from Figure 3-4 into a single log-scale parity plot for comparison between chemical species. All of the data points in Figure 3-5 collapse

to a single line, further confirming that GC-QCD is capable of duplicating the results of GC-FID without the need for individual calibration.

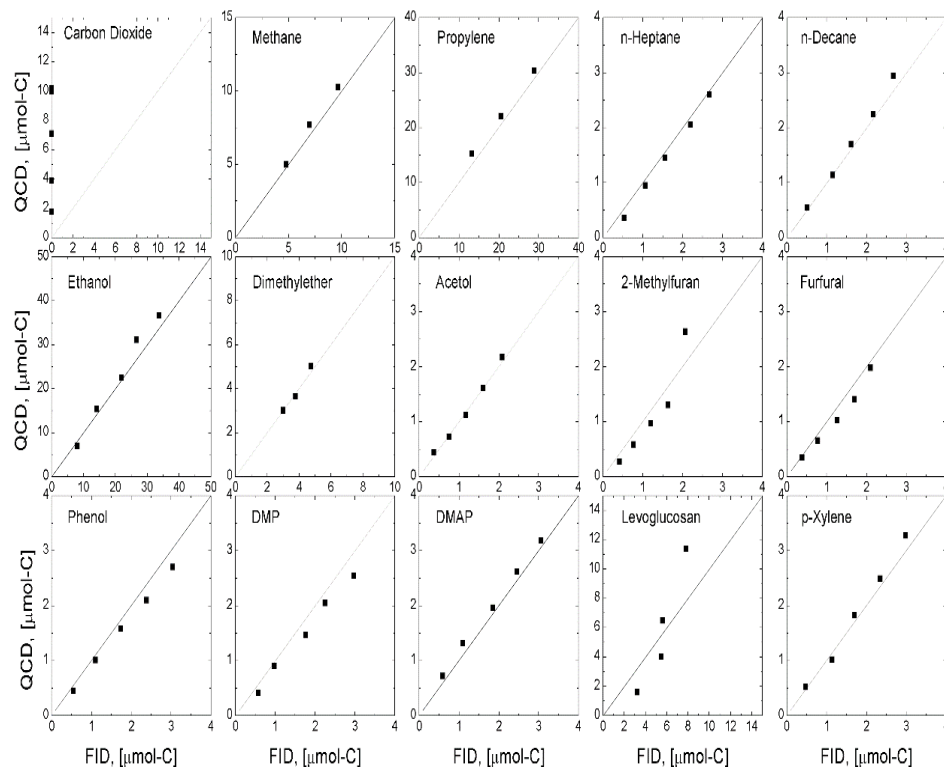


Figure 3-4 Individual Compound Parity of QCD and Conventional FID Quantification
Comparison of molar quantification of identical samples by both QCD and conventional, calibrated FID yield equivalent responses for a range of cellulose-, hemicellulose-, and lignin-derived pyrolysis compounds. Carbon dioxide (first panel) can only be detected by QCD (not FID).

Response factors were determined for each chemical species for the GC-FID and GC-QCD techniques as depicted in Figure 3-6. Response factors were scaled using a methane internal standard to account for day-to-day variability in the FID. GC-FID response factors for all 15 compounds are shown in Figure 3-6 as red bars and vary over an order of magnitude between compounds. In comparison, response factors calculated using GC-QCD are nearly constant across all 15

compounds within experimental error. As demonstrated, an identical GC-QCD response factor across a range of gases and condensable liquids indicates that quantification of a broad range of chemical mixtures can be achieved.

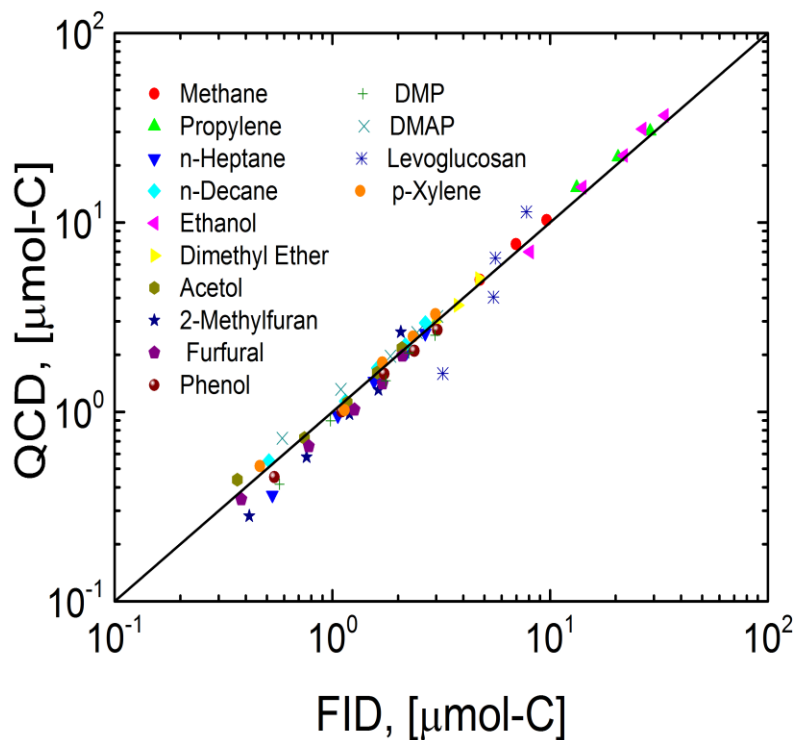


Figure 3-5 Collective Parity of QCD and Conventional FID Quantification

Comparison of molar quantification of identical samples by both QCD and conventional, calibrated FID yield equivalent responses for a wide range of cellulose-, hemicellulose-, and lignin-derived pyrolysis compounds.

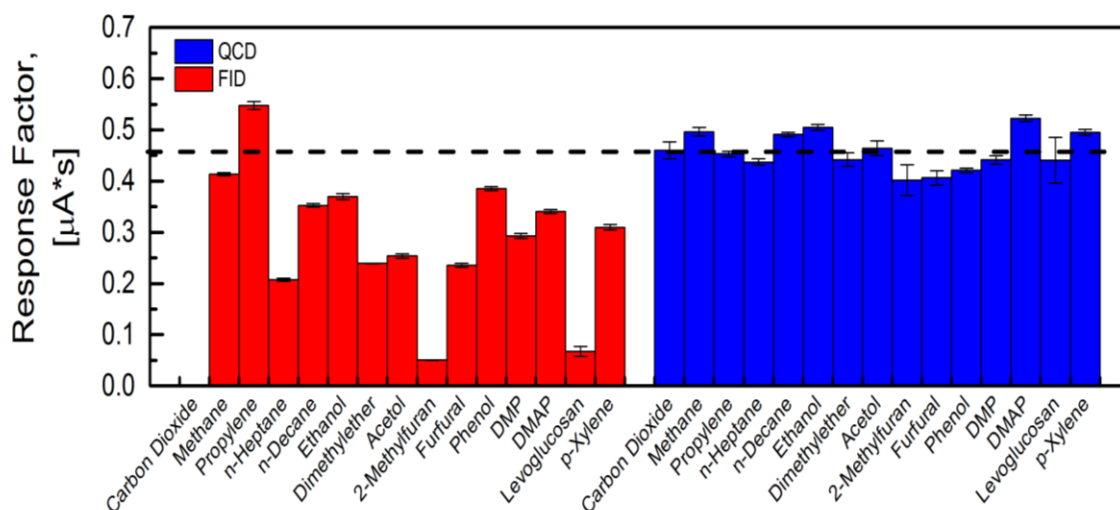


Figure 3-6 Response Factors of Conventional FID (Red) and QCD (Blue)

Compound response factors (scaled using an internal standard of methane) analyzed using GC-FID vary over an order of magnitude, while response factors for compounds using GC-QCD are nearly constant within experimental error.

3.3.2 QCD for Complex Mixtures.

Figure 3-7 depicts a GC-QCD chromatogram of a sample of cellulose fast pyrolysis bio-oil to demonstrate separation of a complex mixture. Separation with sufficient chromatographic resolution to resolve independent peaks was obtained within a 15 minute run. While the compounds in Figure 3-7 are unknown, the total amount of carbon can be rapidly quantified by integrating all peaks individually (multiple integrations) or simultaneously (a single integration), because the response factor for all compounds was the same. Similarly, the total amount of carbon in two overlapping peaks can be determined without complete separation or knowledge of peak identities. Rapid quantification of complex mixtures is also relevant in applications such as two-dimensional gas chromatography (GCxGC), where hundreds of compounds are separated, which makes the QCD an optimal detector for such applications.

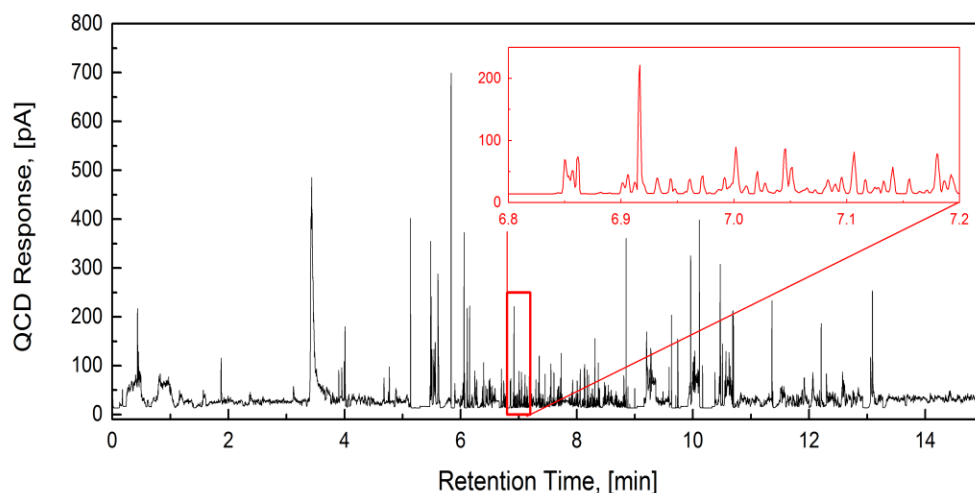


Figure 3-7 GC-QCD of Complex Mixtures Derived from Cellulose Pyrolysis

Chromatographic separation of products from ablative fast pyrolysis of microcrystalline cellulose at 500 °C was achieved for the complex mixture while maintaining peak resolution.

To summarize, the Quantitative Carbon Detector (QCD) is a fully-integrated, drop-in microreactor for calibration-free carbon quantification in gas chromatography. Combination of tandem catalytic oxidation and methanation converts all analyte carbon to >99.9% methane, leading to identical response factors for all separated species. Quantification of carbon eliminates the need to identify and calibrate individual compounds and provides the capability to detect and quantify both carbon monoxide and carbon dioxide. Integrated microreactor design utilized thermodynamic calculations to identify regions of operability that ensured complete conversion of all possible carbonaceous analytes to methane. Microreactor design including flows, catalyst chambers and fittings was characterized via residence time distribution to ensure minimal loss of resolution in analyte separation.

The QCD technique has a wide range of applications for the analysis of unresolved complex mixtures apart from bio-oil. The performance of QCD (now commercialized as Polyarc detector) was evaluated in presence of heteroatoms such as Silicon as shown in

Figure 3-8 and Sulfur typically present in the analysis of consumer products, environmental contaminants, and fossil fuels.

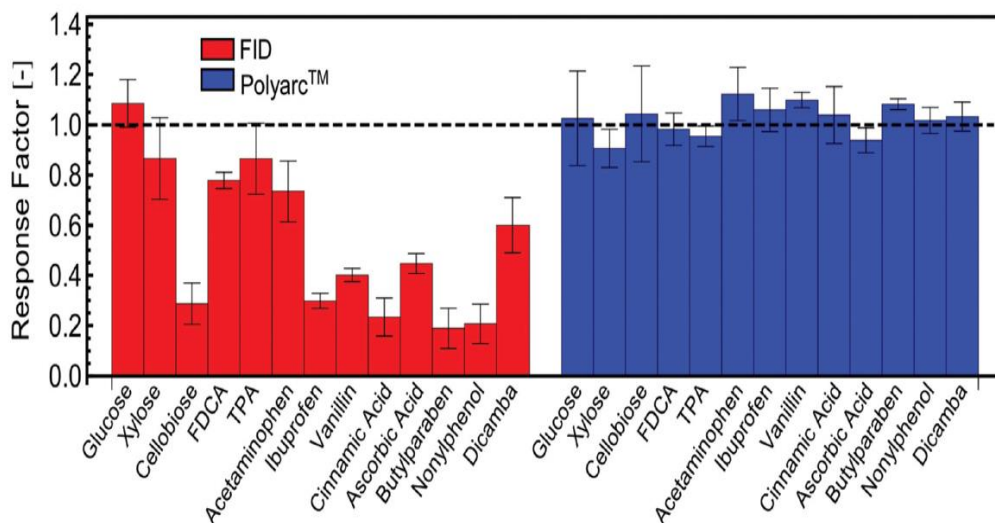


Figure 3-8 Conventional FID (red) and Polyarc QCD (blue) response factors for 14 silylated compounds

Chapter 4 Pulse Heated Analysis of Solid Reactions (PHASR)

4.1 PHASR Design

In the PHASR (Pulse-Heated Analysis of Solid Reactions) method, biomass samples are subjected to rapid thermal pulses of square waves with prescribed temperature and time interval.

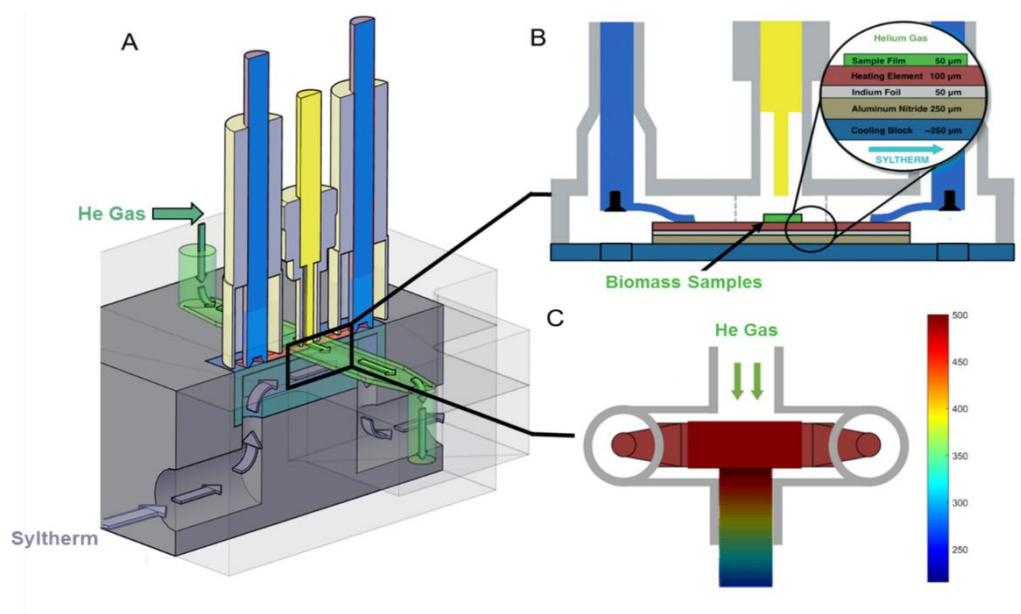


Figure 4-1 PHASR reactor diagram and method

Exploded diagram of the PHASR (pulse-heated analysis of solid reactions) system. Biomass film samples on a heating element are attached to electrical leads within a helium-flow chamber; gas/vapor effluent flows into a gas chromatograph. The lower chamber contains continuously flowing silicon-based coolant. B. Gas flow chamber contains curved metal contacts connecting copper electrical leads and the heating element. Multiple layers of heating element, indium foil, aluminum nitride and a copper micro-channel cooling block transport heat between the gas and liquid chambers. Optical pyrometer in yellow measures the temperature at 1000 Hz. C. Temperature map in PHASR reactor. Vapor products are exposed to high temperature only above the heating element and lower temperatures downstream to minimize secondary reactions.

The PHASR reactor incorporated millisecond heating and cooling of samples within a sealed vessel consisting of two parts as shown in Figure 4-1A: (i) an upper chamber with heating element, biomass sample, temperature measurement by optical pyrometry, and helium sweep gas flow, and (ii) a lower chamber with continuous flow of silicon-based coolant maintained at 3 °C. The reactor housing in the upper chamber includes electrical leads (pass-through copper wired) and a 1000 Hz optical temperature measurement, which form a control loop when integrated with a 2000 Hz PID controller as shown in Figure 4-1B. The upper and lower chambers were thermally connected using a composite layer of: (a) 250 μm copper microstructured heat exchange surface, (b) 250 μm aluminum nitride ceramic, and (c) 100 μm passivated steel resistive heating element. The unique design of PHASR reactor allows heating, temperature control, and cooling of thin film samples in millisecond timescale at the required reaction temperatures. A complete description of the PHASR device is available in prior work²⁸.

4.2 PHASR Performance Evaluation

Five requirements of measuring biomass pyrolysis kinetics were established. PHASR performance was evaluated based on these requirements and was also compared with the conventional reactors typically used to measure kinetics of biomass pyrolysis.

4.2.1 Small biomass sample length scale

Biomass pyrolysis consists of a multi-phase, complex reaction network. Solid- and liquid-phase chemistries are convoluted with transport phenomena (conductive and convective heat transfer as well as liquid-phase diffusion)⁷⁶. It is necessary to conduct experiments with isothermal reacting samples devoid of heat and mass transport limitations. Mettler et al illustrated this requirement by introducing reaction-transport diagrams, as shown in Figure 4-2, which compares the pyrolysis reaction rate with convective and conductive heat transfer rates via dimensionless quantities (pyrolysis numbers, Py^I , Py^{II} and biot number, Bi). Py^I is the ratio of reaction and conduction time scales, Py^{II} compares of reaction and convection time scales, and Bi relates conduction and convection time scales. Pyrolysis experimental techniques traverse two reaction regimes by varying the characteristic length scale of the biomass samples at 500 °C²⁶. For biomass particles, larger than one millimeter, the hot external surface reacts while the inside of the particle remains cold ($Py \ll 1$, $Bi \gg 1$). For experiments utilizing biomass samples with characteristic lengths in the range of 10 μm to 1.0 mm, convection, conduction, and reaction rates are all within two orders of magnitude of one another. Therefore, thin film samples with characteristic length scale (film thickness) smaller than 10 μm are needed for studying isothermal reaction chemistry at pyrolysis temperatures.

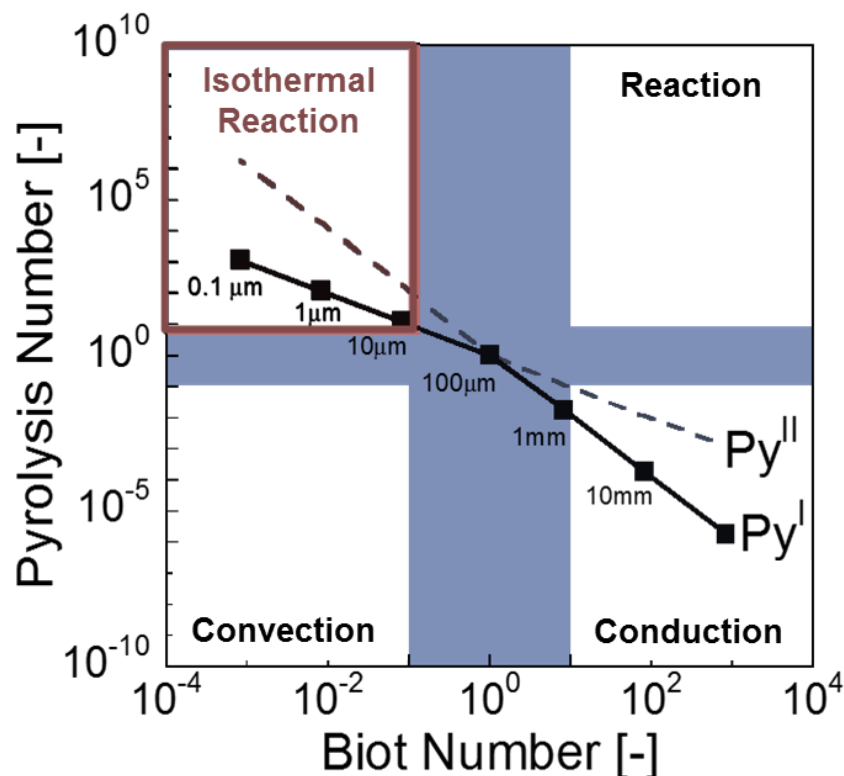


Figure 4-2 Pyrolysis Transport Map

Relative rates of biomass reaction and heat transfer by conduction or convection at 500 °C are compared in terms of Pyrolysis number and Biot number; four pyrolysis regimes are identified (clockwise from top left): isothermal and reaction-limited, reaction-limited, conduction-limited and convection-limited.

The requirement for short length scales on the order of tens of microns was demonstrated experimentally for cellulose pyrolysis chemistry. Long-chain cellulose polymer initially decomposes into shorter polymers and monomer products through primary reactions. These primary products further react in a liquid intermediate phase and vapor phase through secondary reactions. By comparing product yields for powder (millimeter-sized non-isothermal samples which are transport-limited) and thin-film (micrometer-scale films which are isothermal) pyrolysis, it was shown that sample dimension drastically affects reaction pathways. For example, levoglucosan (the most abundant product of cellulose

pyrolysis) yield differs significantly between conventional powder pyrolysis and thin-film pyrolysis (49% for powder; 27% for thin-film at 500 °C)^{68, 52}. The effect of sample length scale on reaction kinetics was further demonstrated by measuring pyrolysis reaction rates for product formation using PHASR with varying sample thickness²⁸. For cellulose samples thicker than 70 µm, the formation rate of products at 500 °C was shown to steadily decrease as the sample thickness increased indicating heat transfer limitations.

4.2.2 Temperature measurement and thermal control

Due to the significant variation in reaction rate due to small changes in temperature, measurement of biomass sample temperature and control is critical for kinetic analysis. For high temperature reactions, such as fast pyrolysis, sensitivity, response and location of temperature measurement must be appropriate to accurately capture reaction temperature. In addition, the method of temperature measurement should not impact reaction chemistry.

In experimental studies using a thermogravimetric analyzer (TGA), the biomass sample temperature is assumed to be the same as the heating source temperature. In a recent review article, Lédé has demonstrated that assuming biomass sample temperature to be the same as the heat source temperature may lead to considerable errors in kinetics experiments⁷⁷. In a conventional TGA, the temperature difference between the heat source and biomass sample significantly increases with heating rate and can theoretically be as large as 100 K⁷⁷. In other commercial micro-reactor systems, such as a furnace pyrolyzer (Frontier Laboratories) and filament pyrolyzer (CDS analytical), sample temperature cannot be measured directly, and it is assumed that the biomass sample temperature matches the furnace/coil heating source temperature. The inability to directly monitor reaction temperature has led to several methods of approximation of effective reaction temperature⁷⁸ which can lead to uncertainties in kinetic analysis.

The PHASR and wire-mesh reactors both use an optical pyrometer to monitor reaction temperature^{28, 49}. This method is fast (response time 180 µs) and

enables temperature measurement at a targeted spot of a biomass sample. In addition, this method was shown to be unaffected by the presence of pyrolysis vapors and aerosols generated during reaction⁷⁹. In the case of the wire-mesh reactor, the biomass sample distribution on the mesh was found to significantly affect temperature gradient in the sample. Even with a uniform distribution of biomass over the entire mesh surface, temperature was found to fluctuate as much as 35 °C⁴⁹. Given the temperature sensitivity of the pyrolysis reaction, this variation can induce significant error in kinetic measurements. In the PHASR reactor, uniform deposition of thin-film samples of biomass on smooth, highly conductive heating elements of carbon steel leads to negligible temperature variation across a sample; this design leads to an accurate temperature measurement within ± 3 °C. In addition, the PHASR reactor has a millisecond temperature control loop. A high frequency pyrometer (1000 Hz) coupled with high frequency PID controlled power supply (2000 Hz) can control heating pulse and reaction progression at the millisecond time scale. By this design, the control system responds at least an order of magnitude faster than the reaction.

4.2.3 Temperature ramp during heating (i.e., heating rate)

To develop an accurate measurement of pyrolysis reaction kinetics, the extent of conversion of the biomass sample during the heating and cooling time should be negligible as compared to the extent of reaction during the isothermal reaction time period.

For a given chemical reaction with known kinetic parameters, the minimum temperature ramp required ($H [=] \text{K sec}^{-1}$) can be calculated at a specific reaction temperature such that total conversion during heating and cooling is minimal (<5 %). Differential conversion dx during heating for a first order reaction can be defined as,

$$\frac{dx}{(1-x)} = A \exp \left\{ -\frac{E_a}{R(T_o + Ht)} \right\} dt \quad (1)$$

where A is the Arrhenius pre-exponential factor; Ea is activation energy; R is universal gas constant; To is initial temperature (room temperature); H is temperature ramp in (K/sec), and t is time in seconds. Integrating equation (1) from $t = 0$ to $t = \frac{(T_{reaction}-T_o)}{H}$, the required value of H for a given T_{reaction} such that conversion $x \leq 5\%$ can be obtained. Using the kinetics of conversion of α -cyclodextrin, a known cellulose surrogate as shown in Figure 4-3⁸⁰, the linear thermal ramp during heating required for limited conversion is calculated from Figure 4-4A for relevant target reaction temperatures ($410 < T < 530$ °C). To study

biomass reactions occurring at 500 °C, the linear temperature ramp of a solid lignocellulose sample must be faster than 7250 °Csec⁻¹.

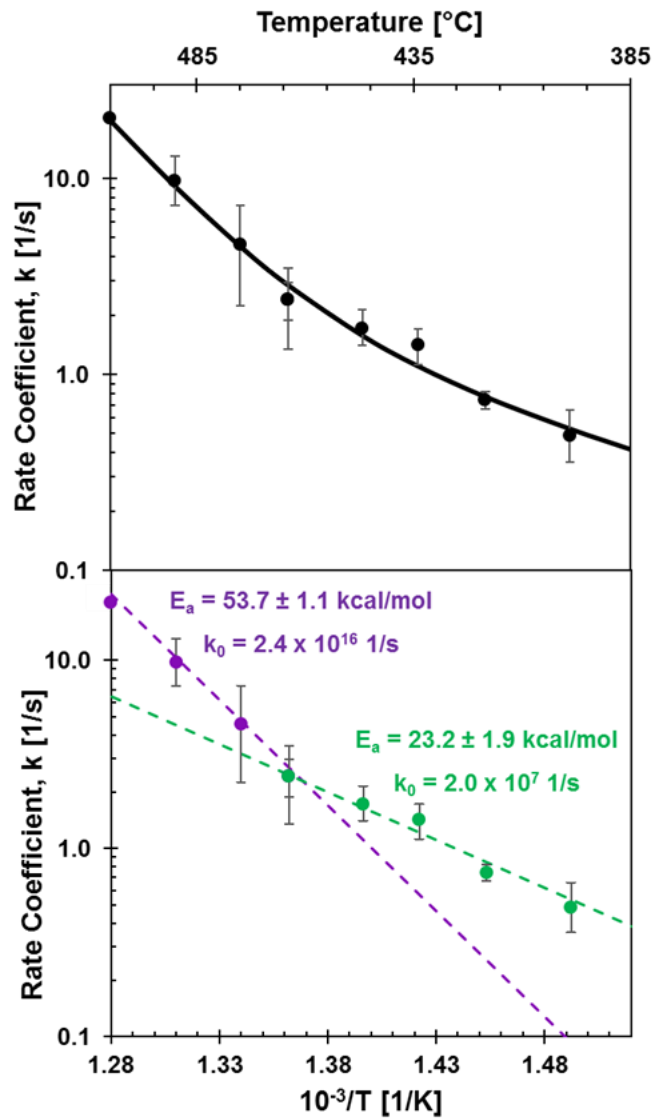


Figure 4-3 Kinetics of cellulose initiation

Data points indicate the first order rate coefficient of the conversion of cellulose surrogate α -cyclodextrin at varying temperature. The conversion of α -cyclodextrin exhibits two kinetic regimes with a transition point around 467 °C, indicative of a change in the mechanism of glycosidic bond cleavage. Error in the apparent activation energy represents a 90% confidence interval.

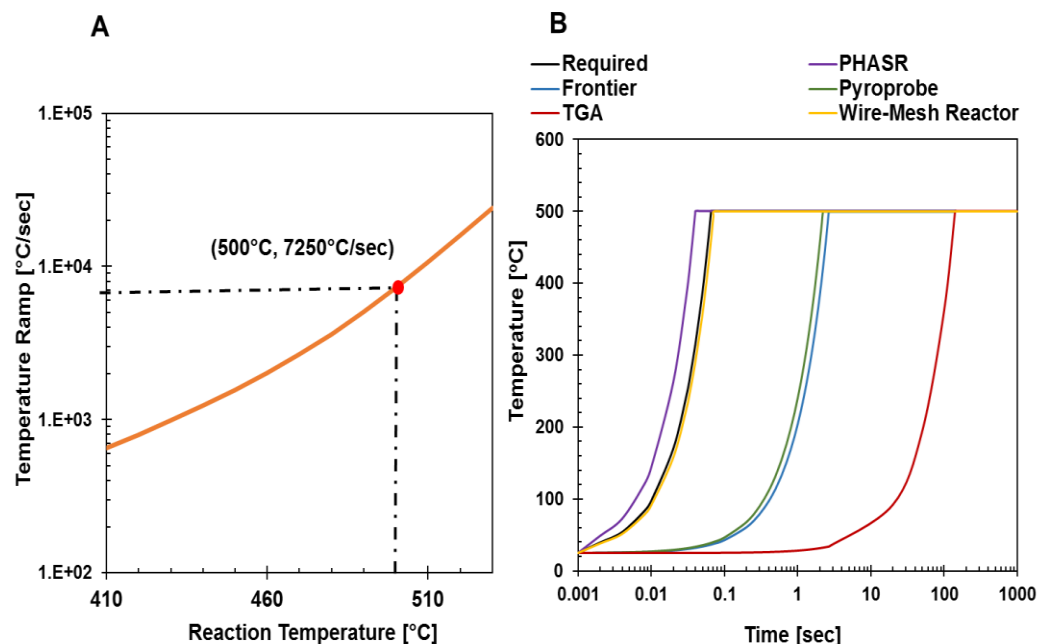


Figure 4-4 Required Heating Rate for Biomass Sample Pyrolysis

A. Required temperature ramp during heating at a given reaction temperature with negligible conversion ($x \leq 5\%$) calculated by equation 1. B. Comparison of biomass sample temperature profile during heating in different pyrolysis reactors

Figure 4-4B compares heating temperature profile of various biomass pyrolysis reactors from $T_o = 25\text{ }^{\circ}\text{C}$ to $T_{\text{reaction}} = 500\text{ }^{\circ}\text{C}$. Thermogravimetric analyzer (TGA) can attain a maximum heating ramp (in red) of $200\text{ }^{\circ}\text{C/min}$, which is three order of magnitude lower than the required heating rate (in black). To characterize the Frontier micropyrolyzer, thermal measurement combined with computational fluid dynamics modeling of the gas flows within the reactor drop-tube furnace was used to determine a maximum temperature ramp of the reactor cup of $200\text{ (}^{\circ}\text{C sec}^{-1}\text{)}$ ⁴⁵. In a similar study evaluating the filament pyrolyzer CDS Pyroprobe 5000, which allows the user to set the nominal heating rate to $20\text{ }^{\circ}\text{C/ms}$ ($20,000\text{ }^{\circ}\text{C/s}$) on the platinum coil, it was found that the heating rate does not represent the heating rate on the sample itself. For a heating rate set point of $20,000\text{ }^{\circ}\text{C/s}$ (in the coil), the fastest measured heating rate at sample center was $216.4\text{ }^{\circ}\text{C/s}$ and the average heating rate was around $131.1\text{ }^{\circ}\text{C/s}$ at atmospheric pressure^{41, 81}. As depicted in

Figure 4-4B, these effective sample thermal ramping rates for Frontier micropyrolyzer (in blue) and CDS pyroprobe (in green) are significantly lower than the required temperature ramp and heating rates. The effective heating rates in resistively-heated wire-mesh (in yellow) and PHASR (in violet) reactor systems are comparable to the required heating rates.

Table 4-1 Pyrolysis Reactor Performance and Thermal Limitations

Three fast pyrolysis reactors (TGA - Thermo-gravimetric analysis, the Frontier Micropyrolyzer, Pyroprobe, and PHASR - Pulse-Heated Analysis of Solid Reactions) expose a sample to a heating ramp rate. The “suitable temperature” is the maximum temperature below which negligible reaction of the biomass sample occurs during the heating phase.

Technique	Heating Ramp Rate [°C/sec]	Suitable Temperature [°C]
TGA	3.34	<212
Frontier	180	<351
Pyroprobe	216.4	<359
PHASR	15,800	<521

Table 4-1 lists experimental reactors used to study biomass pyrolysis and the measured thermal ramp during heating. The maximum operating temperatures meeting this requirement for different systems are well below the pyrolysis temperature, which suggests that at high temperatures significant portion of the overall conversion occurs at a lower temperature than the final desired temperature.

4.2.4 Online detection and Temperature ramp during cooling (cooling rate).

Measurement of the reaction kinetics of solid particles requires the ability to track the progression of reaction with time. While most experimental reactor systems conducting pyrolysis chemistry only allow reactions to progress to

complete conversion, there exist two general experimental approaches to temporally characterize gas and vapor pyrolysis products. By the first method of ‘online detection,’ a pyrolysis reactor is coupled with an online analytical technique such as mass spectrometry; the evolving distribution of chemical species is then quantified in real time. An alternative method quenches the reacting solid sample, thereby limiting the extent of conversion to a pre-set time interval.

For either experimental method, the integrity of the experimental data relies on the ability to effectively measure the time-resolved composition of evolving product species. For the online detection method, the complex evolution of organic vapors and gases must be transferred from the pyrolysis reactor to the detector without significant mixing. Alternatively, experimental methods that quench a reacting solid must cool sufficiently fast to prevent significant low temperature chemistry. Due to the existence of two different experimental methods, the fourth requirement is split into two alternative restrictions, 4A and 4B.

Requirement #4A: Online detection. The challenge associated with online pyrolysis characterization arises from the combination of a pyrolysis reactor with an analytical system capable of quantifying the evolving chemical mixtures. As depicted in Figure 4-5, the time scales of reaction and chemical analysis can be compared for common techniques. While many changes occur on the order of seconds or kiloseconds with conventional heterogeneous catalytic systems, the transient nature of particle pyrolysis occurs in milliseconds. With regards to chemical analysis, gas and liquid chromatography are capable of separating, identifying, and quantifying complex mixtures arising from pyrolysis, but they are too slow ($\tau_{GC} \sim k_s$) to couple with reacting biopolymers. Spectroscopic techniques such as infrared, UV/visible, or nuclear magnetic resonance are faster ($\tau_{spec} \sim s$), but they are incapable of resolving and quantifying 10-100 simultaneous organic compounds. Mass spectrometry techniques such as TOF-MS approaches the time scales of pyrolysis ($\tau_{MS} \sim 50 \text{ ms}$), but it is incapable of scanning a sufficient mass-to-charge (m/z) range at this rate to quantify 50+ organic compounds evolving over 10-50 milliseconds.

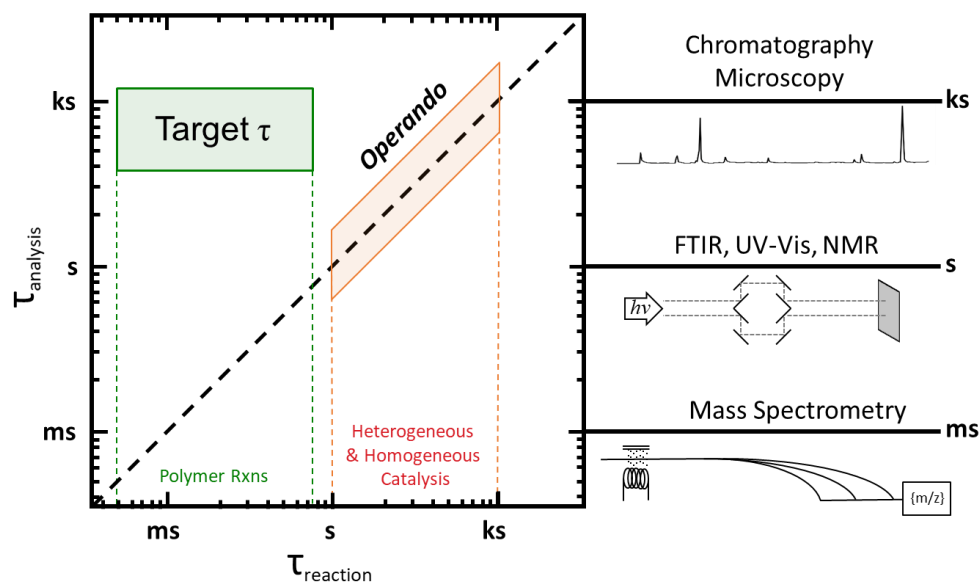


Figure 4-5 Disparity in time scales of polymer reactions and conventional analytical techniques

Temporal characterization of the pyrolysis of biomass can potentially be implemented by combining a high temperature flow reactor with online mass spectrometry ($\tau_{MS} \sim 10$ ms) as shown in Figure 4-6A, provided the time-resolved reactor effluent stream does not mix prior to characterization. This system exhibits three rates relevant to the characterization process: (a) the rate of volatile product formation, (b) the rate of sample mixing, and (c) the rate of transfer between the reactor and the detector. If the rate of volatile product formation and the rate of transfer between reactor and detector is significantly greater than the rate of mixing, the detector will temporally-resolve a composition stream comparable to the rate of reaction. Integrity of the temporal composition stream from the reactor to the detector can be characterized via dimensional analysis. Figure 4-6B compares relative rates of the three processes in terms of ratios of characteristic time constants of reaction to diffusion (x-axis) versus transfer to diffusion (y-axis). The relative rates of the system will depend on reaction characteristics (k , D), and design parameters (l , u), where k is the pyrolysis reaction rate coefficient, D is the axial diffusion coefficient, l is the length of the transfer tube, and u is the velocity of the

fluid in the transfer tube. The time scale of reaction, τ_{rxn} , is characterized by the inverse of the rate coefficient, $k [=] \text{ s}^{-1}$. Solid reactions exhibit complex kinetics which can be approximated as zero, first, or second order systems. Cellulose has been shown to exhibit both first and zero order of furan formation kinetics, with measured rate parameters for initiation reaction as $0.3 < k < 20 \text{ s}^{-1}$ for $380 < T < 500 \text{ }^{\circ}\text{C}$ corresponding to $0.05 < \tau_{\text{rxn}} < 3.3$.

The residence time of the transfer between the reactor and detector, $\tau_{\text{res}} = l \cdot u^{-1}$, is calculated as the transfer line length, l , divided by the transfer fluid (e.g. helium) velocity, u .

Mixing of the temporally-evolving sample of organic products from pyrolysis can occur within the reactor, at the reactor exit, within a tubular transfer line, and at the inlet to the detector. The extent of mixing can be estimated as axial diffusion of vapors within inert gases transferred between the reactor and the detector using diffusion coefficient $D \sim 1 \cdot 10^{-5} \text{ m}^2 \text{ sec}^{-1}$. The time constant of mixing, $\tau_{\text{diff}} = L_c^2 \cdot D^{-1}$, can then be calculated as the ratio of the square of the characteristic length, L_c , divided by the diffusivity, D . The characteristic length of the evolving organic sample is calculated as $L_c = u \cdot k^{-1}$ (for a first order reaction), such that the time constant of mixing is calculated as $\tau_{\text{diff}} = u^2 \cdot D^{-1} \cdot k^{-2}$. A zero order reaction has a characteristic length of the evolving organic sample calculated as $L_c = u \cdot k^{-1} \cdot C_0^{-1}$.

The region of viable operation was identified in Figure 4-6B such that rate of diffusion is at least two orders of magnitude lower than both rate of reaction and rate of product transfer.

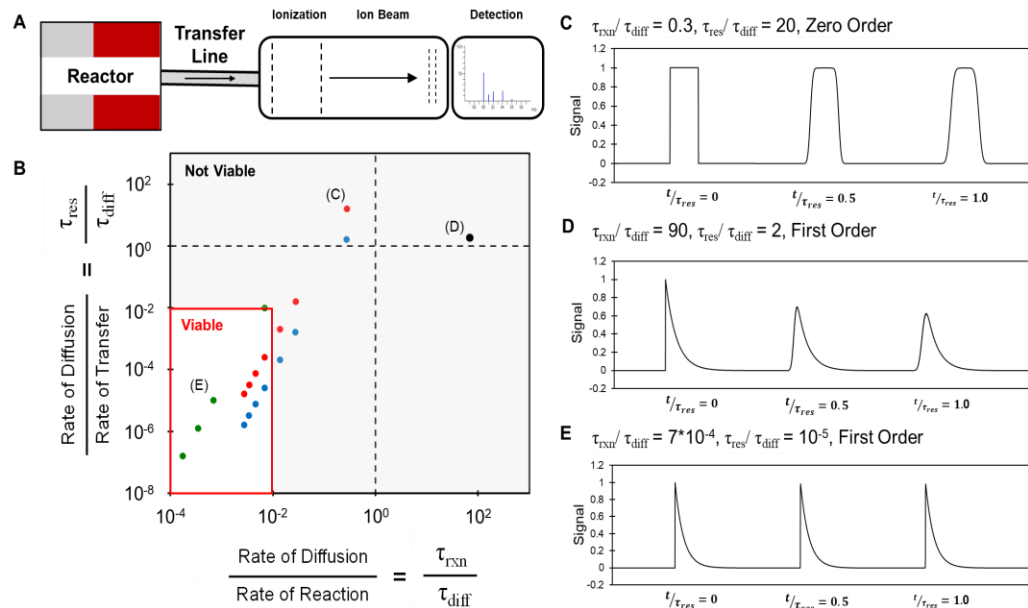


Figure 4-6 Design requirements for a coupled reactor-detector system

A. Schematic of high temperature pyrolysis reactor with online mass spectrometry. B. Comparison of relative time scales of diffusion and residence time within the transfer line (τ_{res}/τ_{diff}) versus diffusion in the transfer line and reaction rate in the reactor (τ_{rxn}/τ_{diff}). The viable region corresponds to the operating conditions such that the rate of diffusion is at least two orders of magnitude lower than both rate of reaction and rate of product transfer between the reactor and detector. Operating points in red, green, and blue are selected for different reaction and design parameters as described in Table 4-2. C. Simulated detector signal for a non-viable operating point C for a zero-order reaction profile. D. Simulated detector signal for a non-viable operating point D for a first-order reaction profile. E. Simulated detector signal for a viable operating point E for a first-order reaction profile.

A set of experimental and reaction conditions (D , u , l , k) correspond to an operating point on Figure 4-6B with coordinates of corresponding relative rates. It is evident from the trend in Figure 4-6B that the operating point can traverse from ‘non-viable’ to ‘viable’ region by decreasing transfer line length (l) and increasing velocity (u). Operating point on Figure 5B can be calculated from the values of experimental operating conditions (u, l) and reaction parameters (k, D). It should be noted that D also depends on temperature and pressure in the transfer line.

- Red series of operating points was generated using following conditions: $D = 1 \cdot 10^{-5} \text{ m}^2 \text{sec}^{-1}$, $k = 12 \text{ sec}^{-1}$, $l = 1 \cdot 10^{-1}$, and $u = 0.02$ to 2 m/sec (For example, 10-100 ml/min flow in 1/8" tube).
- Blue series of operating points was generated using following conditions: $D = 1 \cdot 10^{-5} \text{ m}^2 \text{sec}^{-1}$, $k = 12 \text{ sec}^{-1}$, $l = 1 \cdot 10^{-2}$, and $u = 0.02$ to 2 m/sec . (For example, 10-100 ml/min flow in 1/8" tube).
- Green series of operating points was generated using following conditions: $D = 1 \cdot 10^{-5} \text{ m}^2 \text{sec}^{-1}$, $k = 0.3 \text{ sec}^{-1}$, $l = 1 \cdot 10^{-1}$, and $u = 0.02$ to 2 m/sec (For example, 10-100 ml/min flow in 1/8" tube).

Three different operating points (C, D, and E) were chosen with the conditions in Table 4-2 for simulating the observed response of the detector. Simulated response was calculated by solving the diffusion equation for plug flow in a pipe with axial diffusion, D , for the given initial conditions (e.g. first order, zero order at time zero).

Table 4-2 Experimental conditions and reaction parameters used to calculate operating points

Point	Diffusion Coefficient, D $\text{m}^2 \text{sec}^{-1}$	Velocity, u m/sec	Transfer line, l , meters	First order reaction rate constant, sec^{-1}
C	$1 \cdot 10^{-5}$	$2 \cdot 10^{-2}$	$1 \cdot 10^{-1}$	12*
D	$5 \cdot 10^{-5}$	$2 \cdot 10^{-2}$	$1 \cdot 10^{-1}$	12
E	$1 \cdot 10^{-5}$	$2 \cdot 10^{-1}$	$1 \cdot 10^{-1}$	0.3

*Assumes $C_0=1$

Figure 4-6C, 5D, and 5E depict a simulated response of an online mass spectrometer corresponding to different experimental conditions. Experimental condition points C and D fall in the ‘non-viable’ region and lead to a corrupted compositional profile. For the experimental conditions of point E with viable operating parameters, the reaction profile is retained.

Mixing of the temporally-produced composition profile can derive from many sources and limit the capability of online chemical detection techniques. Composition profiles mix within the reactor, upon the entrance to a sample transfer line, within a transfer line, and at the exit of the transfer line. As depicted in Figure 4-6C and 5D, even minimal mixing can significantly corrupt a kinetic measurement. In particular, sharp transitions in concentration resulting from either zero order (5C) or first order (5D) pyrolysis kinetics rapidly mix with the carrier gas (e.g. helium) and reduce the value of the initial reaction rate. Due to the challenge associated with mixing combined with the requirement of fast chemical characterization, direct coupling of fast pyrolysis at 500 °C ($\tau_{\text{rxn}} \sim 10$ ms) with online chemical analysis is not well suited for the analysis of complex chemical mixtures that evolve faster than the current detection rate.

Requirement #4B: Temperature ramp during cooling (cooling rate). Temporal analysis of pyrolysis products becomes feasible with analytical pyrolysis reactors that have an additional reaction quench process. By stopping the solid chemistry at short time scales, the resulting product gases, vapors, and solid residue (i.e. char) can be characterized with extent of reaction (i.e. time), provided the quench is sufficiently fast. This approach decouples the time scale of reaction (millisecond) from the time scale of analysis (kiloseconds for chromatography).

The required temperature ramp during cooling (i.e. cooling rate) can be identified as the rate that results in negligible feedstock conversion during the quench process. This rate is calculated for a given solid pyrolysis reaction using the method of equation 1. Figure 4-7A shows the required thermal ramp rates during cooling for cellulose pyrolysis at relevant reaction temperatures (400-530 °C). Calculations used kinetic parameters previously measured with cellulose conversion kinetics⁸⁰. It should be noted that the minimum required cooling rate decreases as the reaction progresses due to a decrease in reaction rate with increase in conversion. From Figure 4-7A, it is apparent that the required cooling rate for cellulose that has already achieved 30% conversion is higher than that of cellulose

that has already achieved 40% conversion. Also, at 0% conversion, the required cooling rate is identical to the required heating rate at a given reaction temperature.

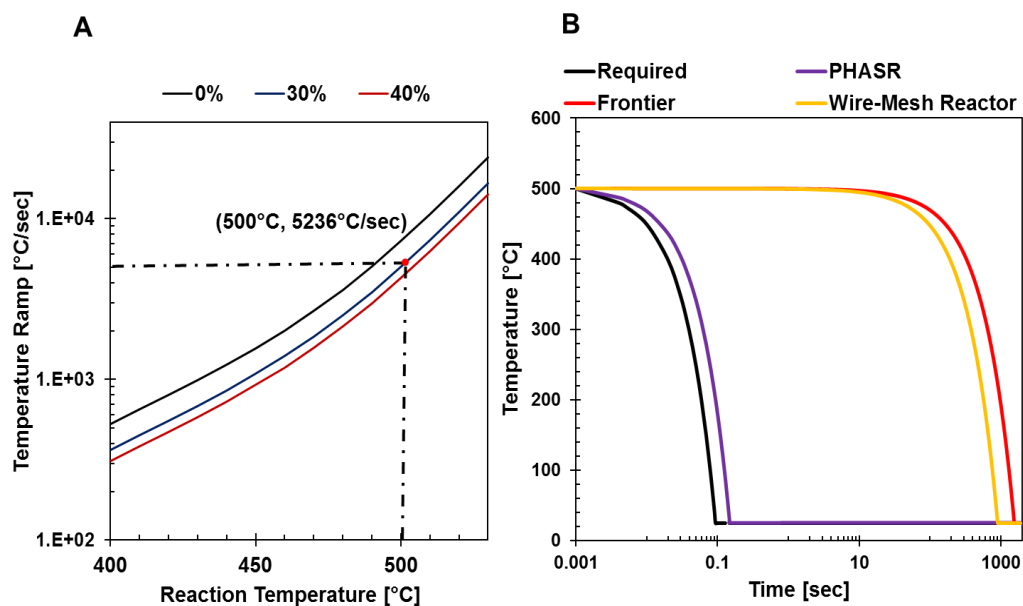


Figure 4-7 Cooling Rate Requirement of Kinetic Biomass Pyrolysis Reactor

A. Required temperature ramp during cooling, at a given reaction temperature and conversion, to achieve negligible conversion during cooling ($x \leq 5\%$) calculated by equation 1. B. Comparison of biomass sample temperature profile during cooling in different pyrolysis reactors.

Figure 4-7B compares temperature profiles during cooling for different reactors from $T_{reaction} = 500^{\circ}\text{C}$ to $T_o = 25^{\circ}\text{C}$. The convective cooling rate achieved with carrier gas in TGA (not shown) and wire-mesh reactors (in red) are extremely low as compared to the required cooling rate for $T_{reaction} = 500^{\circ}\text{C}$ at 30% conversion (in black). In a Frontier micropyrolyzer, the reaction mixture can be cooled using compressed air or Nitrogen circulating through a metallic tube around the furnace tube. The reported cooling rate⁸² of 30 minutes from 600°C to 50°C (in red) is four orders of magnitude lower as compared to required cooling rate. The PHASR system uses high velocity Syltherm heat transfer fluid circulating through a micro-heat exchanger directly in contact with the sample. This unique feature of PHASR

enables rapid cooling rates (in violet) which are comparable to the required cooling rate (in black).

4.2.5 Sweep Gas Flow Rate

In the complex reaction network of cellulose thermal degradation primary products formed by glycosidic bond cleavage can evaporate or undergo secondary reactions in the intermediate liquid phase to new volatile vapor products. Additionally, the volatile products can further undergo degradation in the vapor phase through gas-phase reactions. Secondary reactions in the intermediate liquid phase can be eliminated by using thin film samples. Thin film samples (< 70 microns) allow for volatile products to diffuse to the melt-gas interface and evaporate at least an order of magnitude faster than the rate of melt phase reactions; thus, the reaction rate becomes constant as all volatile products are produced only via the primary reaction pathways.

To minimize the vapor phase reactions, the reactor sweep gas flow rate should be sufficiently high to reduce residence time of vapor products. Residence time of vapors in the furnace-type Frontier micropyrolyzer was experimentally measured using iodine crystal volatilization⁴⁵. Based on visual observation, it was found that vapor residence time can be as high as 85 seconds, which will lead to vapor phase reactions during pyrolysis experiments. The residence time was found to be dependent on geometry and type of sample cup holder.

The PHASR microreactor was designed to eliminate mixing, and gas flows and chamber design enable laminar flow with low residence times. For the selected sweep gas flow rates and the PHASR microreactor volume, the residence time of the flowing helium used to entrain volatile products across the heating element was fewer than 10 milliseconds. Laminar flow ensures that entrained volatile organic products only flow to the reactor exit. Additionally, the use of a heating element distinct from the reactor body ensures that the sweep gases and entrained vapors are not exposed to the maximum reaction temperature. As depicted in the temperature map of PHASR in Figure 4-1C, vapor products are exposed to high

temperature only above heating elements and are exposed to lower temperatures downstream which minimizes secondary reactions. At the same time the downstream temperature is high enough to avoid condensation of high molecular weight products.

In this chapter, five requirements for measuring biomass pyrolysis kinetics were identified as: a short sample length scale, fast heating and cooling rates (or minimal sample mixing for online detection), direct thermal measurement and control, and high product sweep gas flow rate. Performance of five different analytical pyrolysis reactors was compared with respect to the required criteria for each of the identified parameters. As depicted in Table 4-3, the PHASR technique demonstrated capability for achieving all five design criteria relative to other conventional reactors and is the most suitable for reaction kinetic measurements of biomass pyrolysis.

Table 4-3 Characteristics of High Temperature Biomass Pyrolysis Reactors

Pyrolysis Reactors	Sample Length	Heating Rate (°C /sec)	Cooling Rate (°C /sec)	Temperature Measurement	Gas-Phase Residence Time
Requirement	10-100 microns	7250	5236	Rapid, Direct	Milliseconds
Thermogravimetric Analyzer	millimeter	3.34	-	Slow, Indirect	Seconds
Frontier	millimeter	180	0.31	Slow, Indirect	Seconds
Micropyrolyzer	millimeter	216.4	-	Slow, Indirect	Seconds
Pyroprobe	millimeter	216.4	-	Slow, Indirect	Seconds
PHASR	< 70 microns	11875	3167	Fast, Direct	10 ms
Wire-Mesh Reactor	millimeter	6600	0.52	Fast, Direct	milliseconds

Chapter 5 Kinetics of Biomass Pyrolysis

Experiments of lignocellulosic biomass pyrolysis were conducted in the PHASR reactor. As described in Chapter 4, experimental data obtained by the PHASR method represent the kinetics of lignocellulose pyrolysis chemistry independent of measurement or physical artifacts. Samples of Loblolly pine were deposited as a thin film in the PHASR reactor, and experiments evaluated the extent of conversion with time at several temperatures.

5.1 Experimental methods

5.1.1 Biomass Characterization

Loblolly pine (*Pinus taeda*) was provided by FTX Consulting and harvested 2015 in Bamberg, South Carolina. Biomass samples were ground through a 2.0 mm screen size by the Idaho National Laboratories Feedstock Process Development Unit. Compositional analysis to determine structural carbohydrates, lignin, extractives, and protein was performed at the National Renewable Energy Laboratory (NREL) following the standard *Laboratory Analytical Procedure for Biomass Compositional Analysis*⁸³. Proximate and ultimate analysis of the biomass samples (Table 5-1) were carried out by Idaho National Laboratory after further comminution using a Retsch ZM 200 centrifugal mill with a 200 μm screen. This $<200\ \mu\text{m}$ material was then passed through a smaller set of screens using a Ro-Tap and separated into two groups of $x < 38\ \mu\text{m}$ and $38 < x < 58\ \mu\text{m}$. Proximate analysis utilized ASTM D5142. Ultimate analysis was performed using a LECO TruSpec CHN with a S add-on module using a modified ASTM D5373 method. This Flour and Plant Tissue Method uses a slightly different burn profile of 4 L/min for 40 seconds, 1 L/min for 30 seconds, and 4 L/min for 30 seconds of UHP O₂. Elemental sulfur content was determined using ASTM D4239-10, and oxygen content was determined by difference. Heating values (HHV, LHV) were determined with a LECO AC600 Calorimeter using ASTM D5865-10. Elemental ash analyses were carried out by Huffman-Hazen Laboratories (Golden, CO).

Table 5-1 Characterization of Loblolly Pine Biomass

Feedstock	Loblolly Pine
<i>Proximate analysis (wt% dry basis)</i>	
Ash	0.65
Volatile matter	83.71
Fixed carbon	15.64
HHV (BTU/lb)	9026
LHV (BTU/lb)	7692
<i>Ultimate analysis (wt% dry basis)</i>	
C	51.39
H	6.01
O (by diff.)	41.80
N	0.14
<i>Elemental analysis (ppm, dry basis)</i>	
Al	196
Ca	846
Fe	222
Mg	292
Mn	49
P	109
K	737
Si	1256
Na	39
S	62
Ti	13
<i>Compositional analysis (wt% dry basis)</i>	
Structural inorganics	0.28
Non-structural inorganics	0.18
Sucrose	0.00
Water extractable others	1.6
Ethanol extractives	2.92
Lignin	27.94
Glucan	38.30
Xylan	7.17
Galactan	2.68
Arabinan	1.21
Mannan	11.35
Acetyl	1.32
Mass closure	95.38

5.1.2 Sample Preparation

Loblolly pine biomass samples were prepared via aqueous deposition and drying on steel heating elements. PHASR heating elements were initially cleaned using a butane torch until they turned blue, after which they were allowed to sit in air for 24 hours. A 1.0 wt% solution of Loblolly pine biomass (provided by Idaho National Laboratory) in water was prepared and 5.0 μ l pipetted onto the center of the heating element, corresponding to 50 μ g of sample. Samples were then placed in a vacuum at 25 in Hg and held at 40 °C for three hours. To generate 200 μ g samples, four solvent depositions and drying procedures were performed in series. This film preparation method generated a uniform, circular film 3.0 mm in diameter and < 70 microns in thickness.

5.1.3 PHASR Experiments

Experiments were conducted using the following method. A prepared film of biomass on the resistive heating element was inserted into the upper chamber of the PHASR reactor, and both chambers were combined using a polytetrafluoroethylene (PTFE) compression seal such that the copper electrodes contacted the resistive heating element. Inert helium sweep gas was then turned on and flowed through the upper chamber, over the biomass sample film, and out of the reactor and into the inlet of a gas chromatograph (GC) to allow for identification and quantification of gas and volatile products. Cartridge heaters were then pre-heated to maintain the reactor at 260 °C. To initiate the experiment, a MATLAB code was used to set the experimental trial setpoints (reaction duration of 50 to 2000 milliseconds, and reaction temperature of 400 °C to 500 °C). Once the thermal pulse was applied to the biomass sample, the resistive heating power supply turned off and the sample was rapidly quenched in under 150 ms via high velocity sylterm coolant. Figure 5-1 depicts temperature profile of biomass samples at variable temperatures (400 °C to 500 °C) and reaction times 50 to 2000 milliseconds. The volatile gases and vapors produced by pyrolysis were swept by helium flow into the GC inlet; volatile compounds and gases were then captured in the GC column.

Product yields were reported as averages with a 90% confidence interval where each pyrolysis experiment was performed in triplicate. Initial rates of product formation (conversion < 20%) for six different products were measured at six temperatures to generate Arrhenius plots. Product formation rate is defined as,

$$rate = \frac{\mu\text{moles of product formed}}{\text{reaction time in seconds}} \quad (2)$$

Apparent activation of energy of product formation is calculated from the slope of Arrhenius plot.

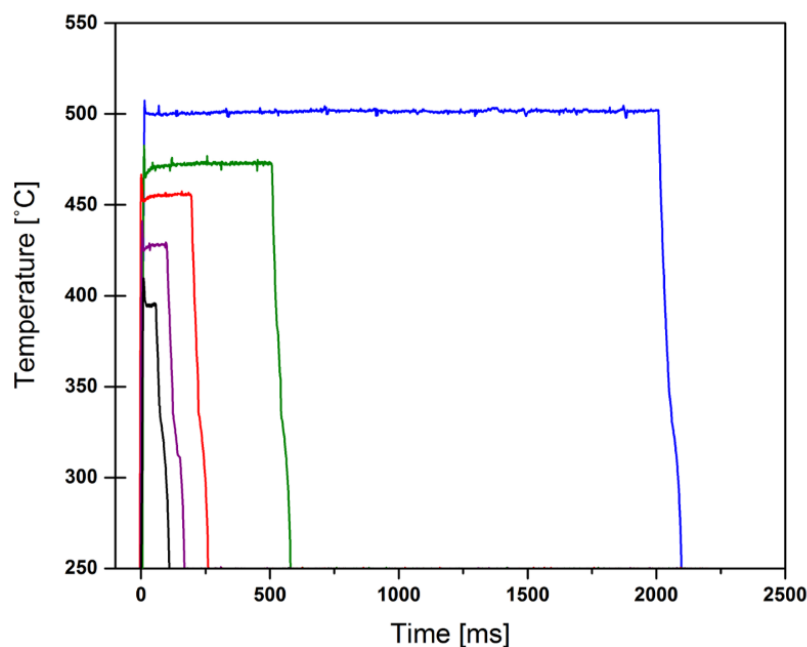


Figure 5-1 PHASR Reactor: heating, temperature control and cooling at millisecond timescale
Thin film samples of Loblolly biomass were pyrolyzed with thermal pulses varying from
50 to 2000 milliseconds at temperatures varying from 400 to 500 °C.

5.2 Results

The formation of volatile organic compounds from Loblolly pine was evaluated with time using the PHASR reactor combined with gas chromatography. Six key products were identified for tracking the temporal evolution of volatile organic product formation from lignocellulosic biomass.

5.2.1 Pyrolysis Product Distribution

Pyrolysis of Loblolly pine samples was conducted at three temperatures (400, 450, and 500 °C), and the produced vapors were identified with GC-MS (ion trap - chemical ionization). Chromatography analysis with the QCD-FID detection method (quantitative carbon detection - flame ionization detector)^{54, 84} permitted quantification of all volatile organic products without identification. By this method, the overall carbon balance at 500 °C at complete conversion (two seconds reaction pulse) was calculated to be 72 ± 4 percent; this includes all volatile organic compounds but not solid char residue. The measured carbon balance greater than 70% is comparable to other biomass pyrolysis studies aimed at evaluating the detailed distribution of organic vapor products^{52, 85, 70}. The analysis by combined chromatography and QCD-FID permits rapid evaluation of complex pyrolysis mixtures.

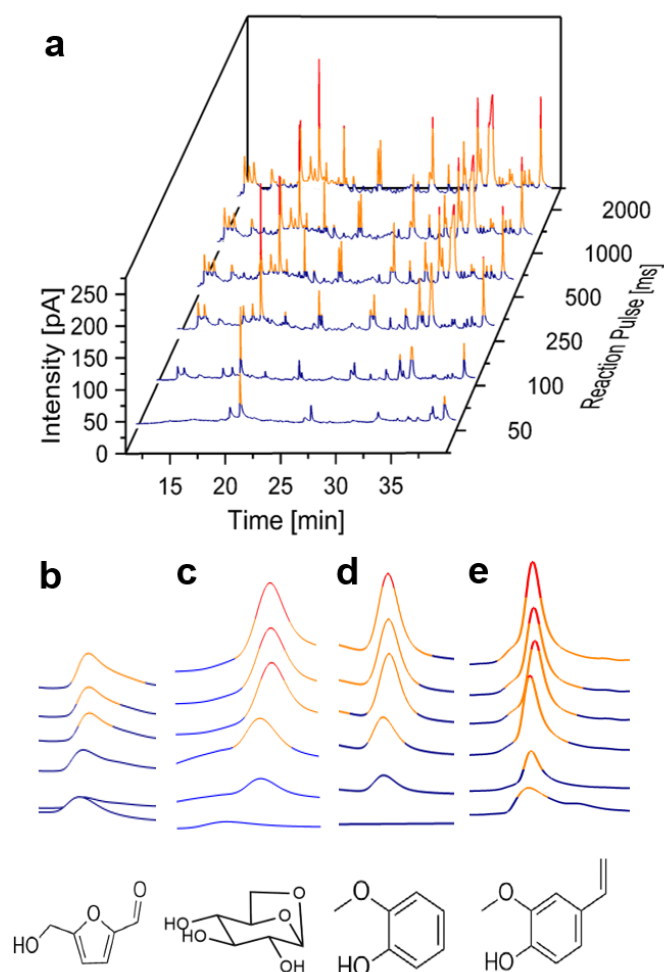


Figure 5-2 Three dimensionally arranged GC-QCD/FID chromatograms

Formation of individual pyrolysis species with increasing pulse time. a.) Pyrolysis of Loblolly pine at 500 °C with increasing reaction pulse duration of 50 - 2000 ms. b.) Hydroxy-methylfurfural - 27.5 min, c.) Levoglucosan - 33.8 min, d.) 2-methoxyphenol - 18.2 min, e.) 4-vinyl-2-methoxyphenol - 28.5 min.

The broad distribution of organic vapor products is apparent in the chromatograms of Figure 5-2. The pyrolysis vapors of lignocellulose include fragments of lignin, cellulose, hemicellulose and extractives. The breadth of products over GC elution times of 10 to 40 minutes is indicative of the immense complexity of pyrolysis of three major polymers interacting as part of the

lignocellulose composite. For this reason, one approach to determining the kinetics of biomass pyrolysis involves the identification of a few major compounds derived from the different biopolymers within Loblolly pine.

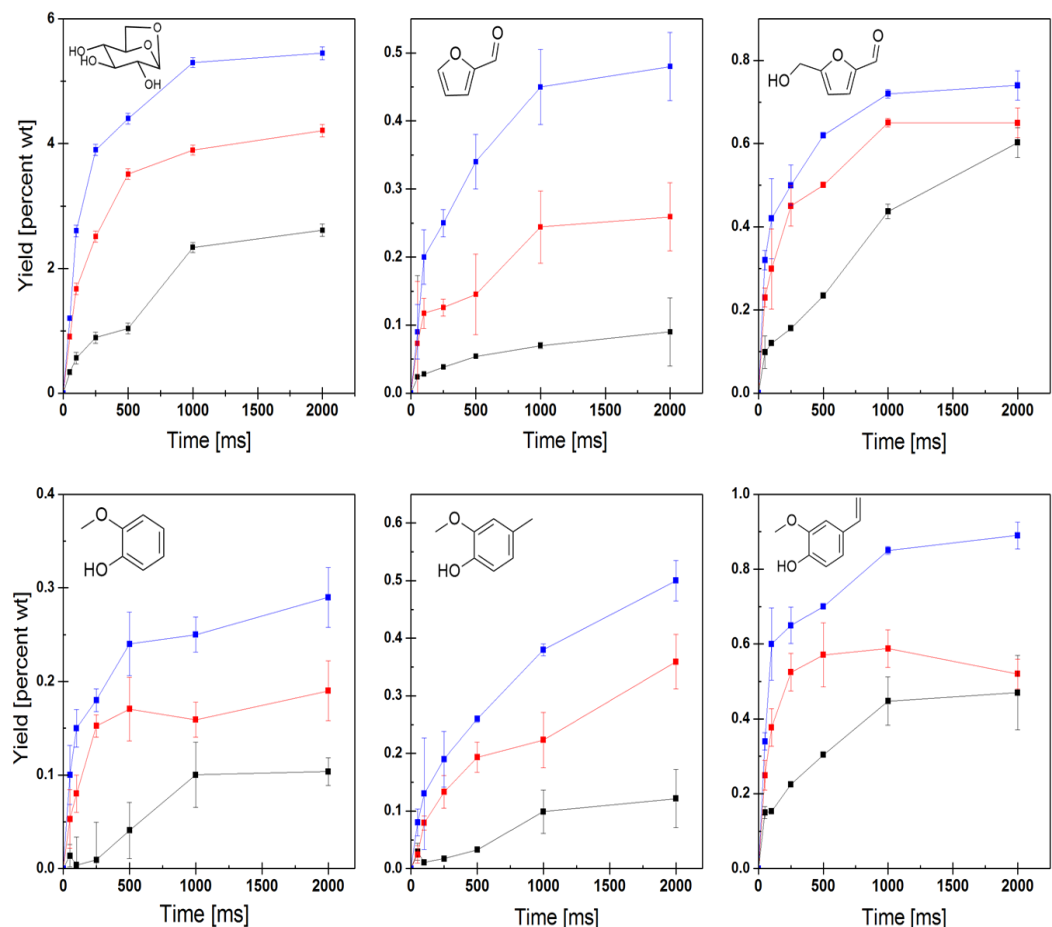


Figure 5-3 Time-resolved evolution of six major chemical products from Loblolly pine pyrolysis

As shown in Figure 5-3, we have selected six compounds that contribute 12 % of the overall carbon balance including three from lignin (2-methoxy phenol, 2-methoxy-4-methylphenol, and 2-methoxy-4-vinylphenol) and three from the carbohydrate biopolymers (levoglucosan, furfural, and hydroxymethylfurfural).

5.2.2 Effect of Biomass Particle Size

The measurement of reaction kinetics requires the elimination of alternative rate limitations, including diffusion and heat transfer. The fibrous nature of lignocellulose introduces the potential for both rate limitations that can be convoluted with apparent reaction kinetics. Using cellulose kinetics and thermal conductivity as a surrogate for lignocellulose, it is estimated in Figure 4-2 (and elsewhere^{68, 52}) that biomass samples must be in the range of 10-50 microns in length scale to achieve isothermal reaction control at 500 °C. This critical length scale was recently confirmed using the PHASR method by evaluating the reaction rate to form four products from cellulose at varying length scales; a clear transition at 60-70 μm was observed in product formation rates, indicating transport rate control above 70 μm at 500 °C²⁸.

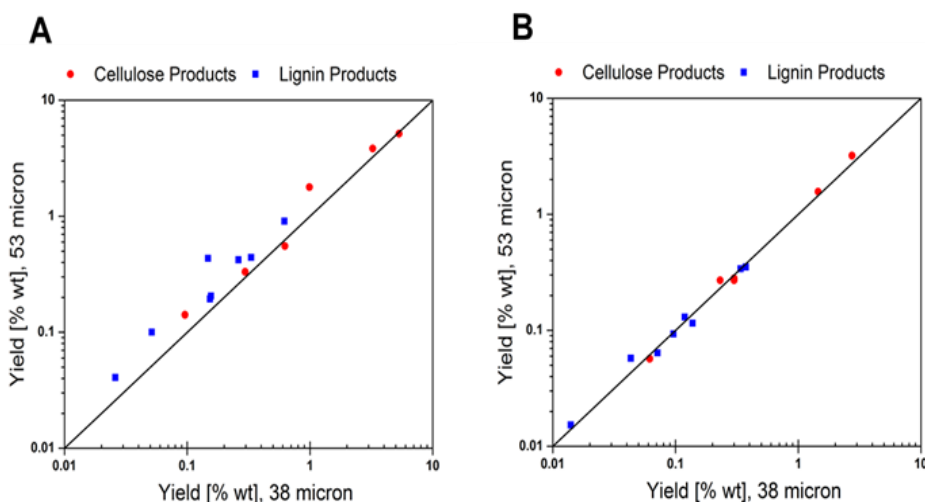


Figure 5-4 Comparison of product distribution from pyrolysis with varying sample particle size

(A) at complete conversion (2000 ms), and (B) at partial conversion (250 ms).

In this work, the evaluation of the reaction kinetics of Loblolly pine also requires isothermal reaction conditions free of transport limitations. Preparation of Loblolly pine led to two different samples: 58 μm and 38 μm nominal size. As depicted in Figure 5-4A, the product yields from the two sample sizes are compared

at full conversion (pulse duration of 2000 ms at 500 °C). Six chemical products derived from the lignin and six products derived from the carbohydrate fraction of Loblolly pine show the same product distribution, indicating that similar reaction conditions and chemistry occurred in the two different sample sizes. In Figure 5-4B, the same comparison between the products of two different Loblolly pine particles was made at only partial conversion (pulse duration of 250 ms at 500 °C); again, the product yields between the two samples are comparable indicating that the micron-scale samples are sufficiently small to achieve reaction control conditions. The product yield data represented in Figure 5-4 is tabulated in Table 5-2.

Table 5-2 Product yields for parity plots in Figure 5-4A-B

Compounds	Full Conversion		Partial Conversion	
	Yield % wt, 53 microns	Yield % wt, 38 microns	Yield % wt, 53 microns	Yield % wt, 38 microns
Levoglucosan	5.15	5.32	3.21	2.74
HMF	0.61	0.63	0.27	0.23
Furfural	0.45	0.30	0.28	0.3
Phenol-2-methoxy	0.43	0.14	0.07	0.06
Phenol-2-methoxy-4-methyl	0.42	0.26	0.13	0.11
2-methoxy, 4-vinyl-phenol	0.91	0.62	0.34	0.34
Furan + light oxygenates	3.8	3.2	1.57	1.45
Acetic acid	1.78	0.99	0.27	0.3
CPHM	0.14	0.1	0.057	0.061
Phenol-4ethyl2methoxy	0.1	0.05	0.058	0.043
Eugenol	0.21	0.15	0.093	0.096
Phenol-2-methoxy propyl	0.04	0.02	0.015	0.014
Vanillin	0.44	0.33	0.35	0.37
Phenol-2-methoxy propenyl	0.19	0.15	0.11	0.13

5.2.3 Time-Resolved Evolution of Pyrolysis Products

The isothermal Loblolly pine samples were subjected to varying pulse durations (50, 100, 250, 500, 1000, 2000 ms) at three different temperatures (400, 450 and 500 °C). For each pulse-duration/temperature combination, the produced vapors were evaluated by gas chromatography (GC-QCD/FID). A chromatogram

for each pulse duration at 500 °C is then presented in Figure 5-2, with the shortest pulse durations presented first. As presented, it is apparent that all the vapor products evolve over the course of two seconds of thermal pulse duration with varying rates of formation. From the complete set of product organic compounds, six compounds were further evaluated for temporal quantification (identified in Figure 5-3). In panels of Figure 5-2b-e, the resolution of four of the six compounds is depicted over two seconds of reaction duration at 500 °C.

Figure 5-3 depicts evolution profile for six products originating from different constituents of Loblolly pine obtained from PHASR kinetics experiments at three different temperatures. Levoglucosan, Furfural, and hydroxymethylfurfural are associated with cellulose whereas 2-methoxyphenol, 2-methoxy-4-methylphenol, and 2-methoxy-4-vinylphenol are associated with the lignin fraction of biomass. As expected, the rate of product formation increases with increasing temperature. The reaction goes to completion at 500 °C within one second, which is fast when compared to previously reported data^{31,86}.

5.2.4 Apparent Kinetics for product formation

The isothermal Loblolly samples were subjected to shortest reaction pulse duration (50 ms) at six different temperatures (400, 410, 420, 440, 450, and 460 °C) such that the conversion ($x < 20\%$). Initial rate of product formation for six different products is calculated as explained in section 5.1.3. Figure 5-5 depicts the Arrhenius plots for the formation of six different products. Apparent activation energies for the formation of levoglucosan, furfural, hydroxymethylfurfural, 2-methoxyphenol, 2-methoxy-4-methylphenol, and 2-methoxy-4-vinylphenol were calculated from the slope of the corresponding Arrhenius plot with E_a values of 16.8 ± 1.3 , 38.1 ± 3.1 , 22.3 ± 1.4 , 26.0 ± 1.6 , 44.5 ± 2.6 , and 23.6 ± 1.3 kcal/mol respectively. These values are comparable to the previously reported wide range of values (10-60 kcal/mol) for lumped activation energies of cellulose and lignin pyrolysis measured by TGA using single heating rate/multiple heating rate/distributed activation energy/model based^{87,88,89,90,91}. The apparent activation energies of product

formations obtained using PHASR satisfy the requirements of kinetic measurements and hence can be used as reactivity criteria for comparing different biomass feedstocks and relative rates of product formations. It should be noted that these barriers represent the convoluted effect of a series of reactions during biomass pyrolysis and, hence should not be directly used for mechanistic interpretations. Further kinetic investigation will be needed for the individual steps in addition to apparent barriers to develop a comprehensive micro-kinetic model.

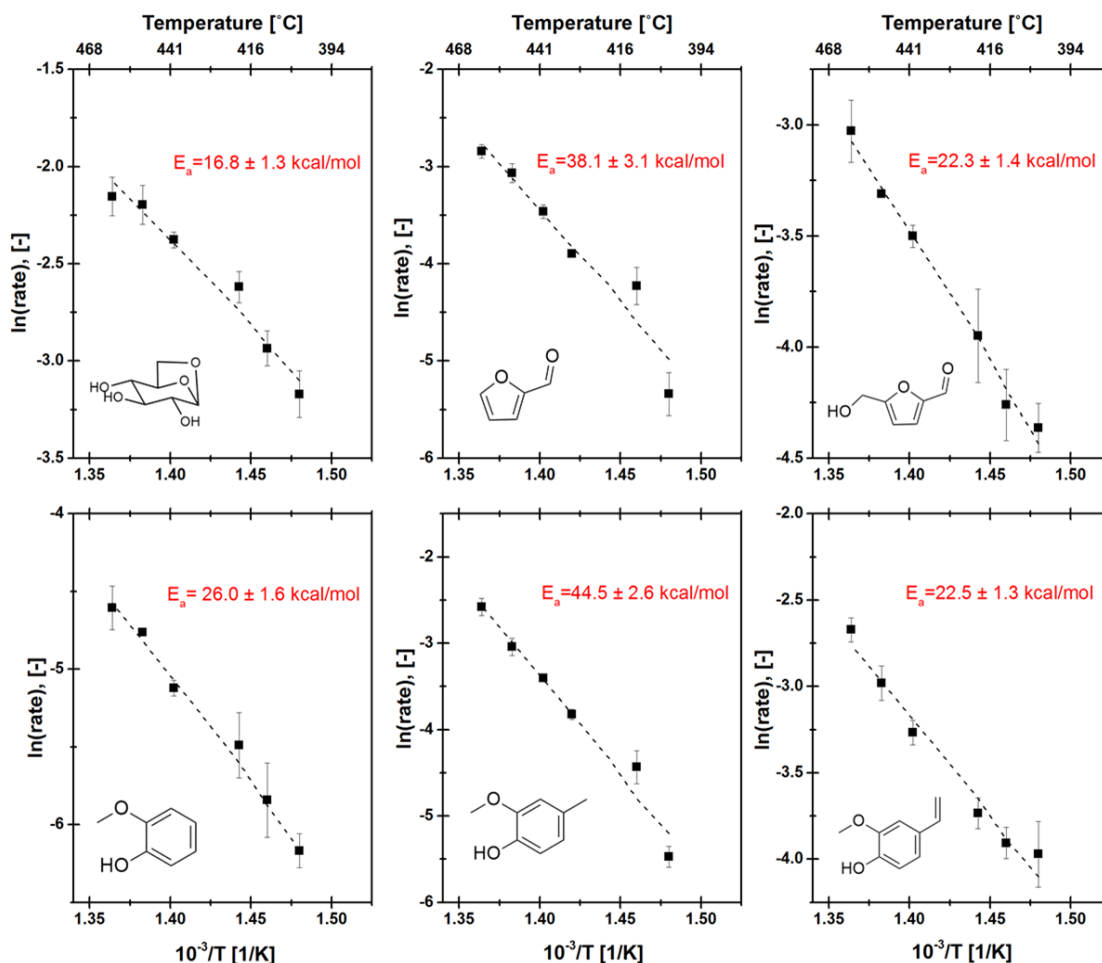


Figure 5-5 Arrhenius plots of six different products forming from pyrolysis of Loblolly pine
Initial reaction rates are calculated by analyzing product yields at short reaction time (50 milliseconds) for six different temperatures at low conversion ($x < 20\%$).

Chapter 6 Cellulose Fragmentation in PHASR

Cellulose is the most abundant biopolymer in the world. It is made up of large number of glucose monomers connected with an ether bond called glycosidic bond. During pyrolysis, cellulose chain depolymerizes to form smaller molecules such as anhydrosugars, pyrans, furans, light oxygenates, and permanent gases. The chemistry of this transformation is highly complex and still debated due to the lack of consistent, reliable experimental data. This chapter investigates the dependence of reported results for cellulose fragmentation on reactor configurations and experimental conditions. The conclusions from the investigation will help eliminating experimental artifacts and also lead to mechanistic understanding.

6.1 Levoglucosan yield from cellulose pyrolysis

Levoglucosan (1,6-Anhydro- β -D-glucopyranose) (LGA) is the most abundant primary product formed during pyrolysis of cellulose. LGA can be converted to ethanol for fuel production directly or through a glucose intermediate by biological processes⁹². It can also serve as a precursor to chemicals of interest such as diols⁹³, surfactants⁹⁴, food, and pharmaceutical additives⁹⁵. Improving LGA yield from cellulose will enhance the viability of LGA-derived products, but optimization of LGA synthesis is hindered by limited understanding of the fundamental mechanisms leading to LGA formation as well as an inconsistency in the reported LGA yields from experiments.

The first study to isolate LGA as a pyrolysis product from cotton cellulose was published a century ago in 1918 which reported 30% yield of LGA⁹⁶. In the 1950s, Russian research groups reported a maximum LGA yield from vacuum pyrolysis of cellulose of about 60% and observed that purity and physical properties of cellulose have a significant effect on the LGA yield⁹⁷. The values of LGA yield from cellulose reported in the literature since then are inconsistent and depend on reactor configuration, operating conditions, and the selected feedstock.

Reported values of LGA from cellulose pyrolysis are compiled in Table 6-1 for numerous research studies with different reactor configurations and experimental conditions. Figure 6-1 depicts the vast range of reported LGA yields (5-80 percent) in the publications listed in Table 6-1. The observed LGA yield from cellulose pyrolysis has been reported from various reactor types including the pilot-scale vacuum^{98,97,99}, fluidized bed¹⁰⁰, and conveyer-type¹⁰¹ reactors. Commercially available Frontier^{102,103,104,85} and CDS pyroprobe¹⁰⁵ microreactors produce LGA in the wide range of 40-80% yield in experiments in the range of 400-500 °C. The highest yield of 79.3 percent was reported by Dobeles et al. who studied pyrolysis of Munktel cellulose using CDS pyroprobe microreactor¹⁰⁶. Dauenhauer et al. observed significantly lower yields of LGA (10-30 percent) from thin-film (micrometer scale) cellulose samples as compared to conventional, powder (millimeter scale) cellulose samples using furnace-

based Frontier microreactors^{52,68}. Similar observations were made with wire-mesh reactors¹⁰⁰ and pretreated cellulose samples^{97,107,108}.

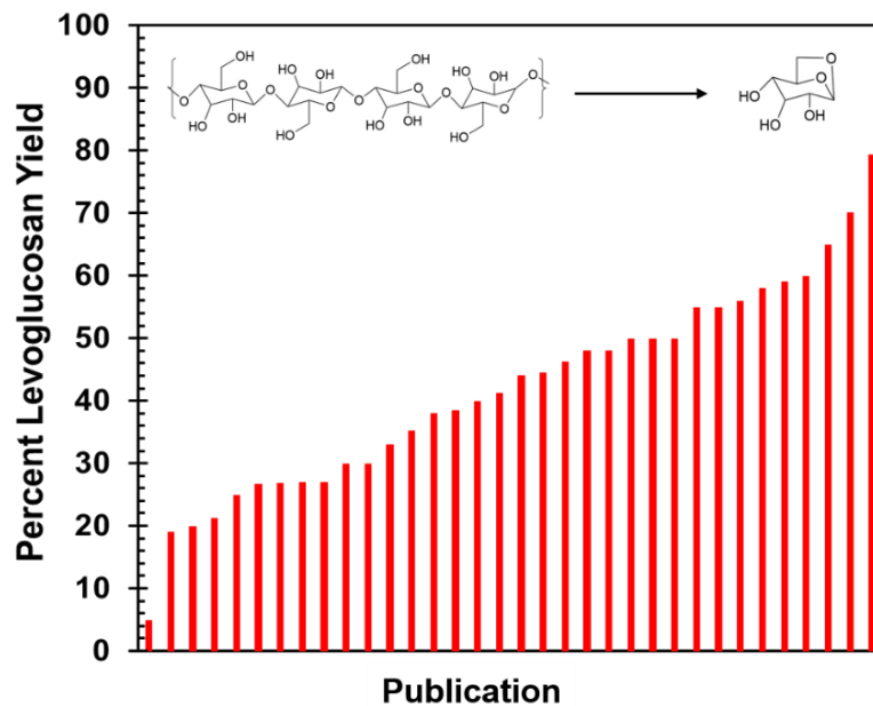


Figure 6-1 Reported Levoglucosan Yield from Cellulose Pyrolysis

Numerous research studies with different reactor configurations and experimental conditions reported LGA yields from 5 to 80 percent. Presented data is described in Table 6-1.

Table 6-1 Compilation of reported LGA yield from cellulose pyrolysis.

The yield of LGA from cellulose varies drastically from 5 to 80 percent carbon depending on reactor types, configuration, and operating conditions

Year	Objective	Reactor Type	Experimental Condition	LGA Yield	Reference
1956	Effect of pretreatment on cellulose pyrolysis	Vacuum	Vacuum Pyrolysis of regenerated cellulose	5	97
2016	Interplay between chemistry and heat/mass transfer during cellulose fast pyrolysis	Wire-Mesh reactor	Cellulose pyrolysis in screen heater at 5 mbar	19	100
2007	Effect of catalysts on cellulose pyrolysis	CDS pyroprobe	Uncatalyzed pyrolysis of cellulose	20	108
1993	Influence of acid pretreatment on vacuum pyrolysis of cellulose	Vacuum Quartz tube reactor	Vacuum pyrolysis of HCl pretreated cellulose with 10 °C/min heating rate at 380 °C	21.3	107
2013	Effect of sample dimension and temperature on pyrolysis	Frontier micropyrolyzer	Thin film samples of cellulose in microfurnace at different temperatures	25	68
1993	Influence of acid pretreatment on vacuum pyrolysis of cellulose	Vacuum Quartz tube reactor	Vacuum pyrolysis of H ₂ SO ₄ pretreated cellulose with 10 °C/min heating rate at 380 °C	26.7	107
2012	Effect of cellulose chain length on pyrolysis	Frontier micropyrolyzer	Thin film samples of cellulose in microfurnace	26.9	70
2012	Homolytic cleavage of cellulose chain	Frontier micropyrolyzer	Thin film samples of cellulose in microfurnace	27	52
1966	Effect of flame retardants on cellulose pyrolysis			27	109

1918	Isolated and Identified LGA	Vacuum	Vaccum Pyrolysis of Cotton Cellulose	30	96
2001	Pilot-scale vacuum pyrolysis of cotton cellulose	Vacuum pilot-scale reactor		30	99
2016	Interplay between chemistry and heat/mass transfer during cellulose fast pyrolysis	Wire-mesh reactor	Cellulose pyrolysis in screen heater at 1000 mbar	33	100
1993	Influence of acid pretreatment on vacuum pyrolysis of cellulose	Vacuum Quartz tube reactor	Vacuum pyrolysis of HNO ₃ pretreated cellulose with 10 °C/min heating rate at 380 °C	35.3	107
2014	Study of primary and secondary reactions in biomass pyrolysis	Frontier micropyrolyzer	Thin film samples of nanocellulose in microfurnace	38	104
1966	Mechanism of cellulose fragmentation	Electric furnace	Vacuum Pyrolysis of Cotton cellulose	38.5	98
2016	Interplay between chemistry and heat/mass transfer during cellulose fast pyrolysis	Fluidized bed	Cellulose pyrolysis in fluidized bed at 1000 mbar	40	100
2015	Effect of reducing ends on cellulose pyrolysis	CDS pyroprobe	Powder samples of pure cellulose at low heating rate	41.2	105
2015	Effect of natural catalysts on pyrolysis	Frontier micropyrolyzer	Thin film samples of cellulose in microfurnace	44	26
1970	Acid-catalyzed formation of LGA from starch	Electric kettle reactor	Pyrolysis of starch in acetic acid, steam	44.5	63
2008	Investigation of Levoglucosenone formation from cellulose	CDS pyroprobe	Pyrolysis of phosphoric acid treated Mukteell cellulose at 500 °C at high heating rate	46.2	106

2012	Homolytic cleavage of cellulose chain	Frontier micropyrolyzer	Powder samples of cellulose in microfurnace	48	52
2016	Effect of natural catalysts on pyrolysis	Frontier micropyrolyzer	Powder samples of cellulose in microfurnace	48	85
1982	Understand cellulose chain fragmentation	Vacuum	Vacuum pyrolysis of pure cellulose	50	98
2015	Effect of reducing ends on cellulose pyrolysis	CDS pyroprobe	Powder samples of reduced cellulose at low heating rate	50	105
2014	Study of primary and secondary reactions in biomass pyrolysis	Frontier micropyrolyzer	Powder samples of cellulose in microfurnace	55	104
2016	Heat and mass transfer effects during cellulose pyrolysis	Frontier micropyrolyzer	Deep cups	55	102
2013	To study mechanism of LGA formation from starch	Tubular furnace reactor	Pyrolysis at 400 °C under vacuum	56	64
2014	Study of primary and secondary reactions in biomass pyrolysis	Frontier micropyrolyzer	Thin film samples of cellulose in microfurnace	58	104
2010	Influence of inorganic salts on primary pyrolysis of cellulose	Frontier micropyrolyzer	Powder samples of cellulose in microfurnace	59	103
1956	Effect of pretreatment on cellulose pyrolysis	Vacuum	Vacuum Pyrolysis of Cotton Cellulose	60	97
2016	Heat and mass transfer effects during cellulose pyrolysis	Frontier micropyrolyzer	Shallow perforated cups	65	102

2007	Preparation of LGA from cellulose and starch	Conveyor-type pyrolyzer	Pyrolysis of microcrystalline cellulose under residual air of 5 kPa	70.1	101
2008	Investigation of Levoglucosanone formation from cellulose	CDS pyroprobe 100	Pyrolysis of Muktehl cellulose at 500 °C at high heating rate	79.3	106

In this chapter, the variation in the observed yield of LGA from cellulose pyrolysis was experimentally investigated. Cellulose pyrolysis experiments were conducted in two different reactors: (a) the Frontier Micropyrolyzer (2020-iS), and (b) the Pulse-Heated Analysis of Solid Reactions (PHASR) reactor system. The Frontier micropyrolyzer is a commercial furnace-based microreactor widely used in pyrolysis research. The PHASR reactor utilizes thin film biomass samples which are subjected to rapid thermal pulses with prescribed temperature and time control^{110,28}. Sample size was found to have a significant effect on the yield of LGA in the Frontier micropyrolyzer. Four hypotheses were evaluated to explain the relationship between observed LGA yield and the sample size of cellulose samples. Co-pyrolysis experiments of cellulose and fructose in the PHASR reactor presented indirect experimental evidence of previously postulated catalytic effects of hydroxyl groups in glycosidic bond cleavage in transport-limited pyrolysis systems.

6.2 Effect of Sample size on LGA yield

Cellulose pyrolysis experiments were conducted to understand the conditions leading to the variation in observed yield of LGA. Figure 6-2 depicts the observed percent carbon yield of LGA from three pyrolysis experiments with different reactors and sample preparation methods. Pyrolysis of powder samples of cellulose in the Frontier micropyrolyzer at 500 °C (blue in Figure 6-2) exhibited yields of LGA of 46-53% as the sample loading varied from 250 to 1500 micrograms. In contrast, a film of cellulose pyrolyzed at 500 °C (red in Figure 6-2) exhibited yields to cellulose of 11% to 20% as the film sample loading varied from 20 to 1500 micrograms. Finally, a film of cellulose pyrolyzed within the PHASR reactor with a loading of 20-250 micrograms at 500 °C (black in Figure 6-2) exhibited a yield of LGA of 6-8%. Thickness of the powder sample measured by SEM imagery was at the millimeter scale, while the thin film samples measured by optical profilometry were at the micrometer scale. Table 6-2 in the reports the measured thickness for both powder and thin film samples for different sample loadings.

Table 6-2 Thickness of Cellulose Samples. Thickness of powder samples in Frontier Pyrolyzer was measured by SEM imagery. Thickness of thin film samples in PHASR reactor was measured using optical pyrometry.

Type of Samples	Sample Loading (μg)	Sample Thickness (μm)
Powder	240	290
	460	490
	800	450
	1020	560
	1540	781
Thin Film PHASR	20	9.82
	50	24.55
	100	49.1
	200	98.2
	250	122.75

The yield of LGA from cellulose pyrolysis was significantly different between powder samples (millimeter scale) and thin film samples (micrometer scale) in the Frontier micropyrolyzer (in red) and PHASR reactor (black). The yield of LGA increased with the increasing sample loading for thin film samples in the Frontier micropyrolyzer. No such effect was observed in the PHASR reactor which facilitates isothermal reaction conditions without transport artifacts; this suggests that the variation in the observed LGA yield can be related to the characteristics of the reactor in which pyrolysis is conducted.

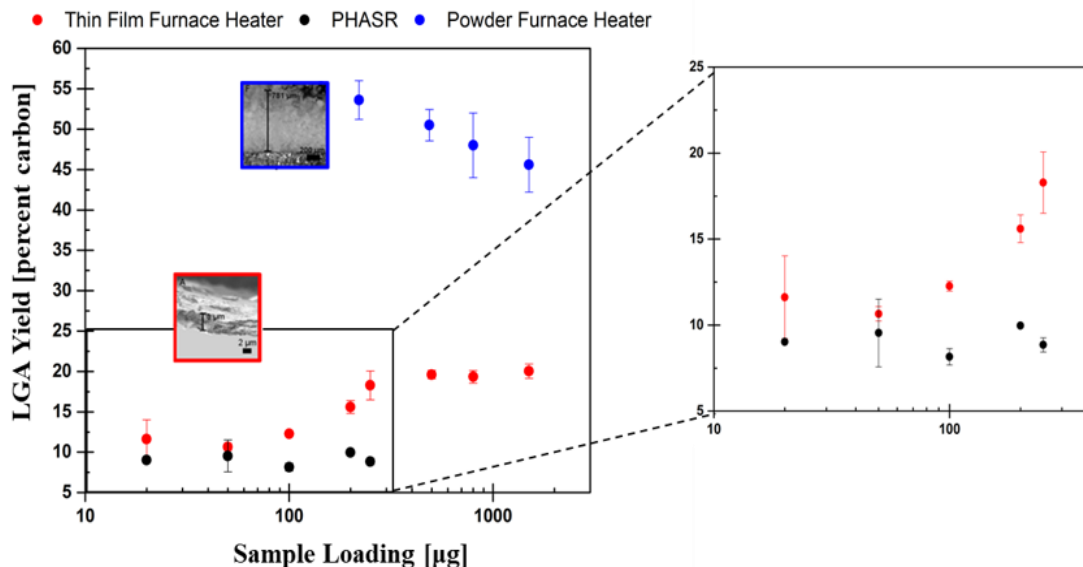


Figure 6-2 Cellulose Sample Loading: Key Descriptor for Levoglucosan yield

Percent carbon yield for levoglucosan from cellulose pyrolysis was found to be significantly different for powder samples (millimeter scale) (in blue) than thin film samples (micrometer scale) in Frontier micropyrolyzer (in red) and PHASR reactor (black). LGA yield was found to increase with the increasing sample loading for thin film samples in Frontier micropyrolyzer (as shown in zoomed in the region). No such effect was observed in PHASR reactor indicating the absence of any transport artifacts. All the experiments were carried out at 500 °C.

Four different hypotheses are proposed and evaluated a through series of experiments to understand the dependence of experimental conditions on the observed LGA yield.

6.2.1 Hypothesis I: Thermal Promotion of LGA Formation

It has previously been established that heating and reaction of cellulose (and biomass in general) can lead to the existence of thermal gradients within reacting particles. Lede' and co-workers showed that biomass pyrolysis obtains sufficiently high reaction rates that the external particle heating produces a transient propagating thermal and reacting front¹¹¹. Reacting thermal fronts within biomass have been predicted by reaction-transport particle models and observed by high

speed photography^{112,23}. Recent experiments with cyclodextrin, a reactive surrogate of cellulose⁵², have also measured fast reaction rates of cyclodextrin ($k \sim 20 \text{ s}^{-1}$) at 505°C ⁸⁰, consistent with reacting thermal gradients within biomass particles. The transition from isothermal reacting particles to particles with reacting thermal gradients has been described with dimensionless values which outline the order of magnitude ratios of cellulose reaction rates relative to conduction and convection heating⁵². For example, cellulose samples heated to 500°C must be as small as 50-100 microns to obtain isothermal reaction conditions²⁸.

The existence of thermal gradients within reacting particles should lower the effective reaction temperature and hence, alter the distribution of chemical reaction pathways in addition to the overall reaction rate. It has already been established that the conversion of cellulose and the formation of volatile products is strongly controlled by the reaction temperature⁶⁸. However, the distribution of pyrolysis products can vary with temperature as the dominant reaction pathways shift in rate and overall extent. One possible explanation for the broad range in observed yield of LGA from a large number of experiments (Table 6-1) is that the yield of LGA is strongly temperature dependent; particles with varying degrees of thermal gradients will, therefore, yield different amounts of LGA, even if the target reaction temperature is the same (e.g. 500°C).

To evaluate the thermal control of LGA yield from cellulose, the pyrolysis of cellulose was conducted with thin film samples (< 250 micrograms, $< 70 \mu\text{m}$) at varying temperature ($350, 400, 450, 500$ and 550°C) within two different pyrolysis reactors as shown in Figure 6-3. Experiments were conducted to fully convert cellulose samples at all temperatures. Within the Frontier reactor, the yield of cellulose was $\sim 25\text{-}30 \text{ C}\%$ at $350\text{-}500^\circ\text{C}$; the yield reduced to $\sim 22 \text{ C}\%$ at 550°C ⁶⁸. Alternatively, the yield of LGA from cellulose within the PHASR reactor was substantially lower ($\sim 4\text{-}9\%$). The reaction to produce LGA also exhibited a steadily increasing yield with increasing temperature.

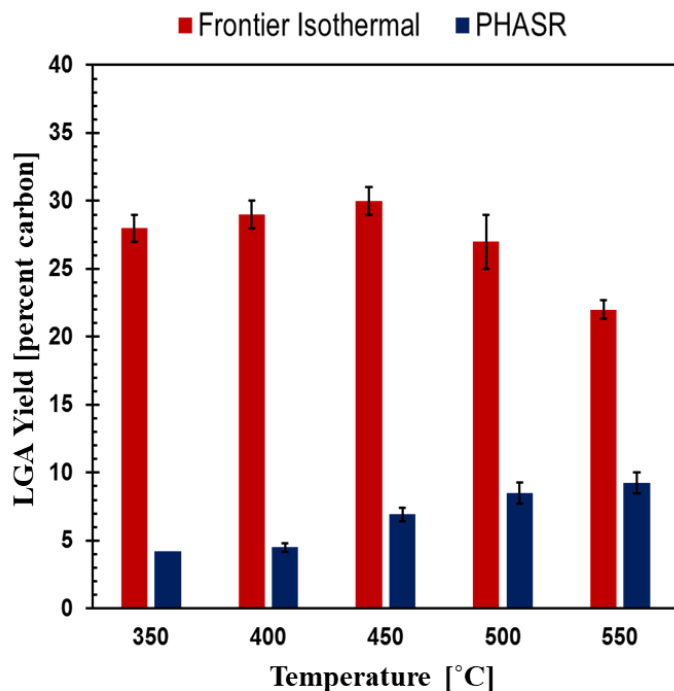


Figure 6-3 Pyrolysis Temperature and LGA yield

Isothermal pyrolysis experiments with cellulose samples were conducted at a different temperature in both Frontier (red) and PHASR (blue) reactors. Levoglucosan yield does not change significantly with temperature. Cellulose loading in frontier isothermal samples was 250 micrograms and the results are replicated from a previously published data⁶⁸. Cellulose loading for PHASR samples was 200 micrograms with sample thickness less than 70 microns.

The experimental data of Figure 6-3 indicate that the yield of LGA is only moderately affected by the reaction temperature. The yield only varied a few percent between 350 and 550 °C, while the yield observed between reactor types varied substantially (20 to 60%). The depicted values of the yield of LGA in Figure 6-3 are consistent with previous publications describing LGA production with these reactors, and variation in the reaction temperature cannot explain the significant variation of the yield of LGA reported in the literature.

6.2.2 Hypothesis II: Crystallinity of Cellulose

Cellulose is a semi-crystalline polymer with regions of high and low crystallinity; while cellulose crystals form several polymorphs (IA, IB and II), the dominant crystal structure in plants (e.g. wood, cotton) is IB^{113–115}. Analytical techniques like XRD, solid-state ¹³C NMR are widely used to determine crystallinity of cellulose. A parameter termed the ‘crystallinity index’ (CI) is used to quantify the relative quantity of crystalline regions in cellulose, and the CI of cellulose is often used to interpret changes in cellulose structure after physicochemical and biological treatments¹¹⁶. The impact of the crystallinity of cellulose on pyrolysis chemistry has been debated in the literature. Katô et al. observed that in TGA analysis, the threshold temperature for pyrolysis is higher for microcrystalline cellulose than amorphous tobacco cellulose¹¹⁷. Recently, Wang et al. observed drastic differences in solid-liquid phase reactions, liquid intermediate formation, and vapor phase product distribution during pyrolysis of Avicel cellulose (CI of 60.5%) and ball-milled Avicel cellulose (CI of 6.5%) using TGA and Py-GC/MS analyses^{118,119}. Similar observations were made by Mukurate et al. who showed that both crystal allomorph and relative crystallinity of cellulose impact the slate of primary products produced by fast pyrolysis with only the most highly crystalline cellulose samples yielding vapors dominated by LGA¹²⁰.

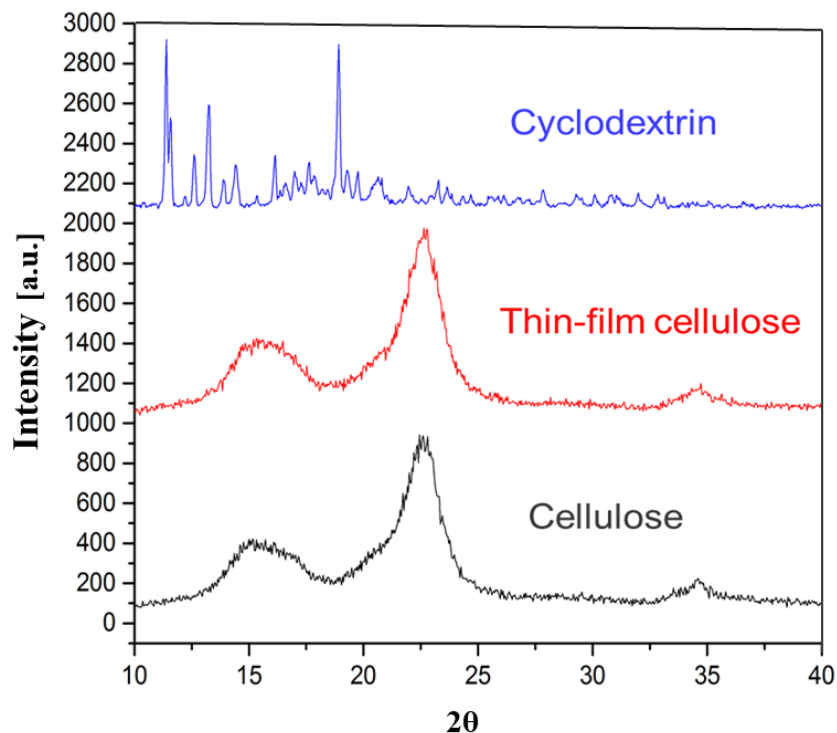


Figure 6-4 Crystallinity of Cellulose and Cyclodextrin Samples

The crystallinity of cellulose and cyclodextrin samples prepared was compared by XRD analysis. Powder cellulose samples (in black) have identical crystallinity index as compared to thin film cellulose samples (in red). α -Cyclodextrin, a known surrogate of cellulose, has a highly crystalline structure (in blue) as compared to cellulose.

Figure 6-4 depicts the X-ray diffraction spectra of α -cyclodextrin powder, cellulose powder, and cellulose thin film samples. The crystallinity indices for thin-film and powder cellulose samples calculated using their respective XRD spectra (red and black in Figure 6-4) were found to be the same within experimental error. From the measured spectra, the crystallinity of both the powder and thin-film cellulose samples was calculated as 74% by the XRD peak height method developed by Segal et al¹²¹. In this method, the crystallinity index (CrI) of the cellulose from X-ray diffraction (XRD) spectrum is calculated using the ratio between the intensity of the crystalline peak (I002 - IAM) and total intensity (I002) after subtraction of the background signal measured without cellulose in X-ray diffraction spectrum. I002

is the maximum intensity (in arbitrary units) of the [002] lattice diffraction and IAM is the intensity of diffraction in the same units at $2\theta = 18^\circ$ as shown in the XRD spectrum in Figure 6-5. XRD spectra of cellulose were compared with the spectrum of α -cyclodextrin, a known reactive and kinetic surrogate of cellulose. The spectrum of cyclodextrin exhibiting numerous well-defined peaks is consistent with a high degree of crystallinity, which is in sharp contrast to the broader peaks and lower crystallinity of cellulose.

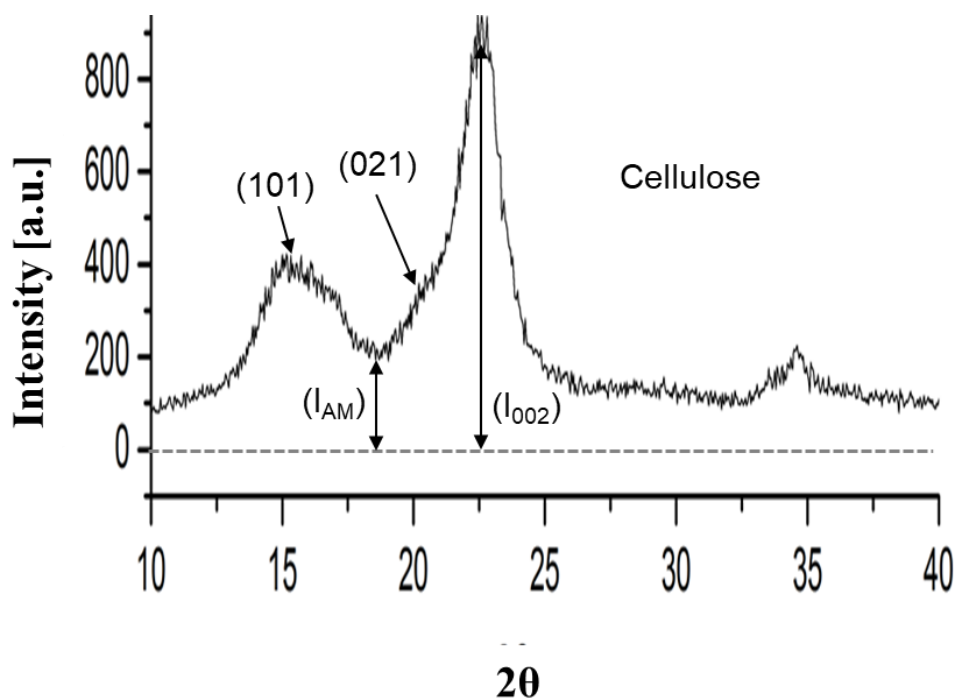


Figure 6-5 X-ray diffraction (XRD) spectrum of thin film cellulose samples and calculation of crystallinity index.

The experimental data indicates that there is no direct relationship between crystallinity of the cellulose sample and corresponding observed yield of cellulose. Powder and thin-film cellulose exhibits nearly identical XRD spectra while producing significantly different yields of LGA. Moreover, highly crystalline films of cyclodextrin exhibit the same yield of LGA as semi-crystalline films of cellulose. This conclusion is consistent with previous experimental and computational studies related to crystallinity and hydrogen bonding structures of cellulose. Watanabe et

al demonstrated using IR studies that hydrogen bonding structure in cellulose IA and IB drastically changes at about 220 °C which is much lower than the typical pyrolysis temperature (>400 °C)^{72,122}. Computational studies from Matthews et al and Agrawal et al. also predicted a drastic change in hydrogen bonding network of cellulose at 500 K and 440 K respectively indicating that the initial crystal structure may not be important at higher reaction temperatures relevant to pyrolysis technologies^{123,124}.

6.2.3 Hypothesis III: Secondary and Gas-Phase Reactions

In the complex reaction network of cellulose thermal degradation, the primary products formed by glycosidic bond cleavage can evaporate or undergo secondary reactions in the intermediate liquid phase to form new volatile vapor products. Additionally, the volatile products can further degrade in the vapor phase through gas-phase chemistry. The extent of secondary reactions can differ based on both reactor and experimental design and hence, can alter the observed product yield. For example, LGA produced from cellulose by transglycosylation can further decompose to form furans, light oxygenates and secondary char^{85,125,126,127} in the intermediate liquid phase.

Secondary reactions of LGA can alter the apparent product yield and potentially explain the broad range of yields reported for different reactor types. LGA is formed only as a primary product; therefore, high yields of LGA could result from systems devoid of secondary and gas-phase reactions where LGA could further decompose. To evaluate this hypothesis, pyrolysis of cellulose was evaluated in the PHASR reactor, which was designed to eliminate both secondary liquid-phase chemistry and gas-phase decomposition. The PHASR reactor uses thin films of cellulose to promote rapid evaporation of primary products; additionally, vapor products have minimal residence time (< 10 ms) in the heated reaction zone which reduces the extent of vapor phase chemistry. The PHASR design was evaluated by varying the thickness of cellulose films, and it was shown that the yield of products became fixed for films smaller than 70 microns²⁸.

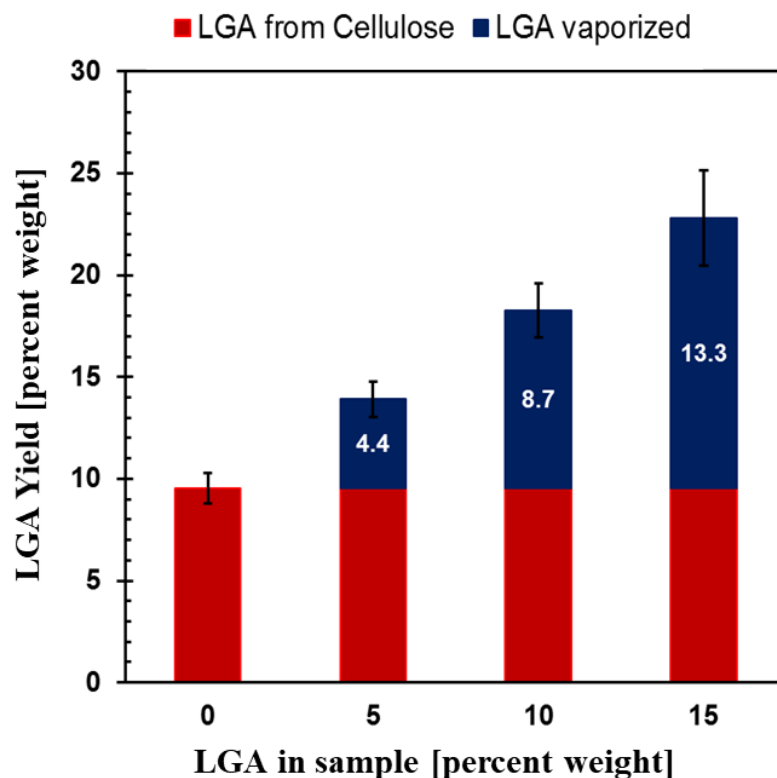


Figure 6-6 Co-Pyrolysis of Cellulose and Levoglucosan

Copyrolysis experiments with cellulose and levoglucosan were performed in the PHASR reactor by varying the amount of levoglucosan (% weight) added to thin film samples of cellulose. Added levoglucosan in the sample was recovered indicating that the secondary and gas-phase reactions of LGA in the reactor were negligible. All the experiments were performed at 500 °C using total loading of 200 micrograms.

Further evaluation of the extent of secondary and gas-phase reactions of LGA was performed in the PHASR reactor by co-pyrolysis experiments. As shown in Figure 6-6, pyrolysis of cellulose was conducted in the PHASR reactor at 500 °C with the addition of LGA comprising 5, 10, and 15 wt% of the sample. The pyrolysis products were then analyzed and the yield of LGA is depicted in Figure 6-6. It is evident from the data in Figure 6-6 that the fraction of LGA in the co-pyrolysis sample matches with the increase in the observed LGA yield after pyrolysis. This suggests that the LGA fraction of the sample evaporates and does

not undergo liquid phase secondary reactions or vapor phase reactions. In other words, the observed LGA yield from a pure cellulose sample in PHASR can be concluded to be purely from the primary reaction of cellulose degradation.

The interpretation of the Figure 6-6 data that negligible secondary liquid phase and gas-phase reactions occur within the PHASR reactor indicates that secondary chemistry is unlikely to account for the broad range of yields of LGA reported in the literature. If secondary chemistry was reducing the yield of LGA, then the PHASR reactor should provide the highest yield of LGA, while other reactors with substantial secondary chemistry should exhibit lower yields. The data in Figure 6-3 show the opposite result; the PHASR reactor results in the lowest reported yield of LGA at 400-500 °C.

6.2.4 Hypothesis IV: Catalytic Promotion of LGA with Reactive Hydroxyl Groups

Primary reactions in cellulose degradation can be influenced by the presence of reactive species in the reaction mixture. The extent of these interactions depends on the residence time of the reaction mixture in the liquid intermediate phase. Reactive hydroxyl groups in oxygenated products and intermediates can catalyze the glycosidic bond cleavage and influence the observed yield of products. Seshadri et al. proposed that explicit hydroxyl groups can catalyze condensed phase reactions of glucose and its polymers using quantum chemical calculations^{128,129}. Hosoya et al also showed that bimolecular reaction between hydroxyl groups of methyl – β – glycoside can lower the activation barrier for glycosidic bond cleavage¹³⁰. During the pyrolysis of thick “powder” samples, mobile chemical species can interact with the active sites of cellulose (i.e., glycosidic bonds) and act as catalysts; the longer diffusional paths in these samples increase their residence time and the probability of interacting with cellulose. In contrast, pyrolysis of cellulose in reacting thin films should rapidly remove mobile, volatile compounds capable of catalyzing LGA formation and can limit their catalytic effect.

To probe the catalytic effect of volatile organic compounds, co-pyrolysis experiments were performed which combined cellulose and one of several potential organic ‘catalysts’ as a thin-film within the PHASR reactor. The resulting yield of pyrolysis product LGA was then measured for each mixture at 500 °C. As depicted in Figure 6-7A, the yield of LGA from pure cellulose (~8%) was the same as the co-pyrolysis with water, adipic acid, and glycerol. Glycerol and water are volatile components (boiling points of 290 and 100 °C, respectively); volatile species within the PHASR reactor should immediately evaporate and have a negligible impact on cellulose pyrolysis chemistry, which is consistent with the experimental results. Adipic acid decomposes before volatilizing, and it should reside within the sample during cellulose decomposition; however, no catalytic promotion was observed in the co-pyrolysis of cellulose and adipic acid.

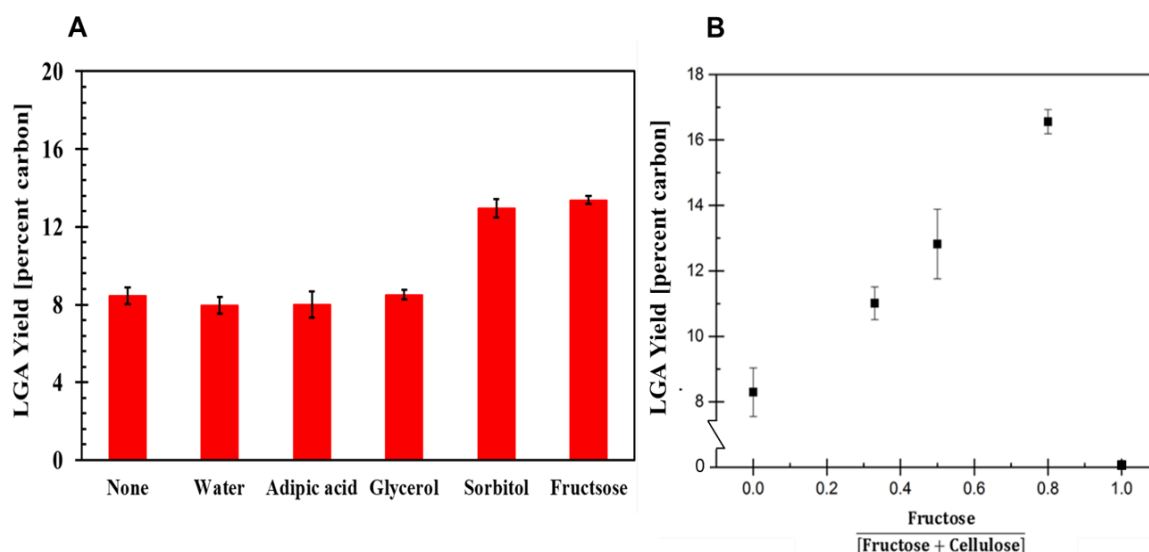


Figure 6-7 LGA Yield from Co-Pyrolysis of Cellulose and Small Oxygenates

A. Co-pyrolysis experiments with cellulose and and small oxygenates were conducted in the PHASR reactor by varying the fraction of fructose in the sample. B. Yield of LGA from fructose and cellulose mixtures. All the experiments were carried out at 500 °C with the total loading of 200 micrograms in all the samples.

Catalytic promotion of LGA was observed in the co-pyrolysis of cellulose with sorbitol and fructose, as shown in Figure 6-7A. Fructose was used as a co-

reactant, because it does not form LGA when pyrolyzed alone; additionally, fructose is a non-volatile sugar which increases the residence time of reactive hydroxyl groups within the reaction mixture. As shown in Figure 6-7B, the observed yield of LGA increases from 8.3 percent carbon to 16 percent carbon with the increasing fraction of fructose in the co-pyrolysis samples. This evidence of an increase in the observed LGA yield with the increased interaction of reactive hydroxyl groups in the reaction mixture supports the hypothesis that catalytic hydroxyl groups promote LGA formation within the melt-phase of cellulose.

In this chapter, the conditions leading to LGA formation were evaluated the effect of experimental parameters including reactor configuration and cellulose sample size on the chemistry of cellulose pyrolysis. Four different hypotheses were proposed and tested to investigate the relationship between cellulose sample size and the observed LGA yield. Hypotheses based on the thermal promotion of LGA, the crystallinity of cellulose samples, gas-phase degradation, and liquid-phase secondary reactions were negated based on the experiments performed in Frontier and PHASR reactors which indicated limited impact on the yield of levoglucosan. In contrast, experiments which combined cellulose and fructose indicated a strong correlation between yield of LGA product and fructose composition; this provided indirect experimental support of the previously postulated catalytic effect of hydroxyl groups in glycosidic bond cleavage.

Chapter 7 Mechanism of Levoglucosan Formation

7.1 Overview of Cellulose Fragmentation

Cellulose is the major constituent of biomass and the most abundant biopolymer in the world. During high temperature pyrolysis, cellulose chain fragments to yield small monomers like levoglucosan (LGA). Figure 7-1 is a simplified reaction scheme for cellulose fragmentation to yield LGA. Cellulose is partially crystalline solid containing glucose monomers connected through glycosidic bonds. Intrachain and interchain interactions of the monomers through Hydrogen bonding networks of hydroxyl groups provide the crystalline structure to the cellulose matrix. In the initial stages of the pyrolysis, cellulose matrix loses crystallinity and evaporates water. As discussed in the previous chapter, these physical transformations are kinetically irrelevant at high reaction temperatures.

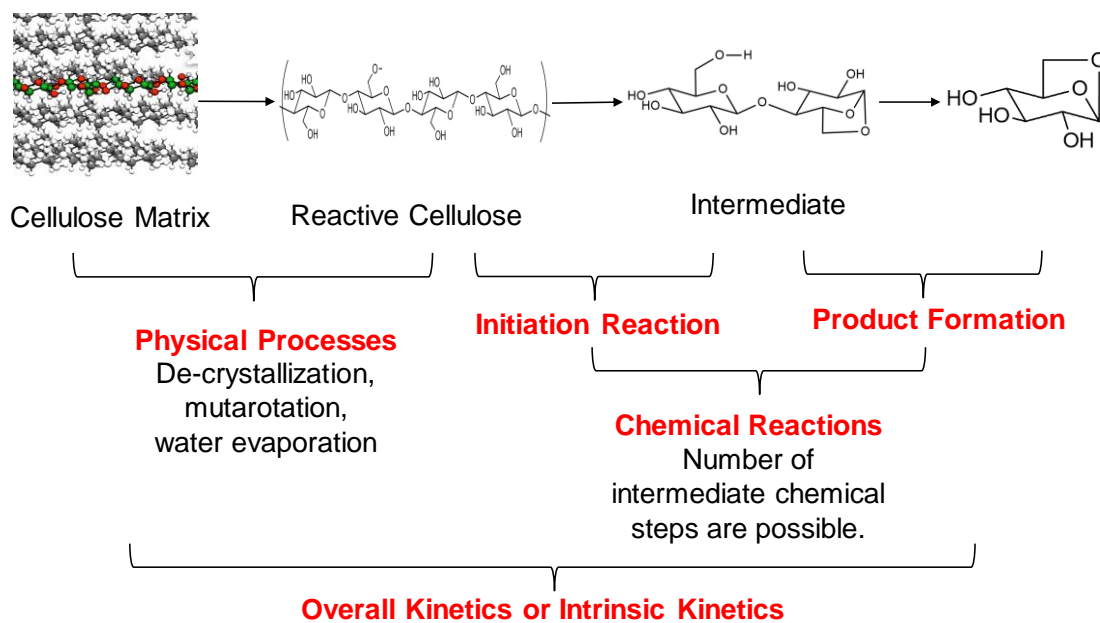


Figure 7-1 Simplified Reaction Scheme for Cellulose Fragmentation

Reactive cellulose chain then depolymerizes to form a liquid intermediate phase which further decomposes to form multiphase product mixture. The chemical transformation

of reactive cellulose chain to final products can be represented as a two-step process. The initial reaction to form intermediate liquid phase is followed by product formation reactions.

Glucose monomers in cellulose are bound to each other through β -1-4 linkages called as glycosidic bonds. During initiation reactions, these glycosidic bonds break to form smaller polymers which constitute intermediate liquid phase. The glycosidic bonds can break randomly through mid-chain cleavage or unzip one monomer at a time through end-chain cleavage. Even after years of research, considerable debate still exists on the topic of mechanisms of these initial glycosidic bond cleavages. The lack of reaction-limited kinetic data and the ability to decouple the elemental reactions in the cellulose transformation hinder the experimental validation of various proposed mechanisms. Recent studies with PHASR kinetics experiments have elucidated the mechanisms of initiation reactions. Krumm et al. revealed that rate of depolymerization for α -cyclodextrin (α -CD), a kinetic and reactive surrogate for cellulose, showed a transition from slow rates to rapid rates as temperature increased with the transition being noted at $T = 467^\circ\text{C}$. Zhu et al. by fitting rates of α -CD consumption to a first order model extracted experimental pre-factors and activation barriers for pyrolysis initiation. Their findings showed a low activation barrier (23.2 ± 1.9 kcal/mol) and pre-factor ($2 \times 10^7 \text{ s}^{-1}$) leading to very slow rates at temperatures below 467°C in contrast to a high activation barrier (53.7 ± 1.1 kcal/mol) and pre-factor ($2.4 \times 10^{16} \text{ s}^{-1}$) at higher temperatures.

In this chapter, PHASR kinetics experiments were performed for measuring kinetics of cellulose fragmentation with the focus of understanding the mechanism of levoglucosan (LGA) formation. Apparent kinetics were measured by tracking LGA formation from cellulose at 400 - 500°C . Additionally, product formation step was decoupled from the initiation reaction by identifying cellobiosan, a simple anhydrosugars, as kinetic surrogate for the cellulose pyrolysis intermediate. The kinetic parameters extracted from the pyrolysis of cellulose intermediate to LGA using cellobiosan and were compared to the computed parameters for various mechanisms proposed. The kinetic information of the overall transformation, initiation reaction, and

product formation step will complete the entire reaction spectrum and develop an experimentally validated microkinetic model.

7.2 Experimental Methods

7.2.1 Sample Preparation.

Microcrystalline cellulose was purchased from Alfa Aesar (product # A17730). Cellobiosan was purchased from Santa Cruz Biotechnology Inc. (Product # sc-221413). Other anhydropolysaccharides Cellotriosan, Cellotetrosan, and Cellopentosan were purchased from Synthos Inc. (Product # AG807, AG809, and AG811 respectively). $^{13}\text{C}_1$ LGA was synthesized from $^{13}\text{C}_1$ glucose (Sigma Aldrich product # 389374) through one-step synthesis using 2-chloro-1,3-dimethylimidazolinium chloride (DMC) as a dehydrative condensing agent as shown in [Figure 7-2](#)^{131,132}. $^{13}\text{C}_1$ -glucose (500 mg, 2.76 mmol, 1 equiv) and trimethylamine (11.6 mL, 83.2 mmol, 30 equiv) were dissolved in water (50 mL) in a 100 mL rb flask with stirring. The flask was cooled to 0 °C in an ice bath and a solution of DMC in water (4.67 g, 27.6 mmol, 10 equiv, 5.5 mol L⁻¹) was added dropwise to the reaction. The flask was allowed to warm slowly to room temperature overnight. After 20 h, an aliquot was removed to determine the conversion (>99% conv. observed). The remaining solution was concentrated via rotary evaporation to remove water and trimethylamine. Upon drying the concentrate, acetone (50 mL) was added to dissolve the product, stirred, and filtered (repeated 4×). The combined filtrates were concentrated *in vacuo* and the resulting solid was dissolved in a minimal amount of ethanol. Subsequent addition of diethyl ether (100 mL) and cooling in a freezer facilitated precipitation of the remaining trimethylamine salts. The filtrate was concentrated *in vacuo* and the solid was recrystallized from ethanol aided by cooling in the freezer to yield colorless needles (59 mg, 13%). $^{13}\text{C}_1$ -levoglucosan was confirmed by ^1H and ^{13}C NMR analysis of the sample. NMR spectra of the sample are depicted in [Figure 7-3](#)[Figure 7-4](#) and [Figure 7-4](#).

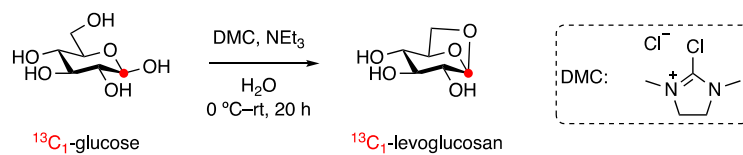


Figure 7-2 Synthesis of $^{13}\text{C}_1$ LGA from $^{13}\text{C}_1$ glucose

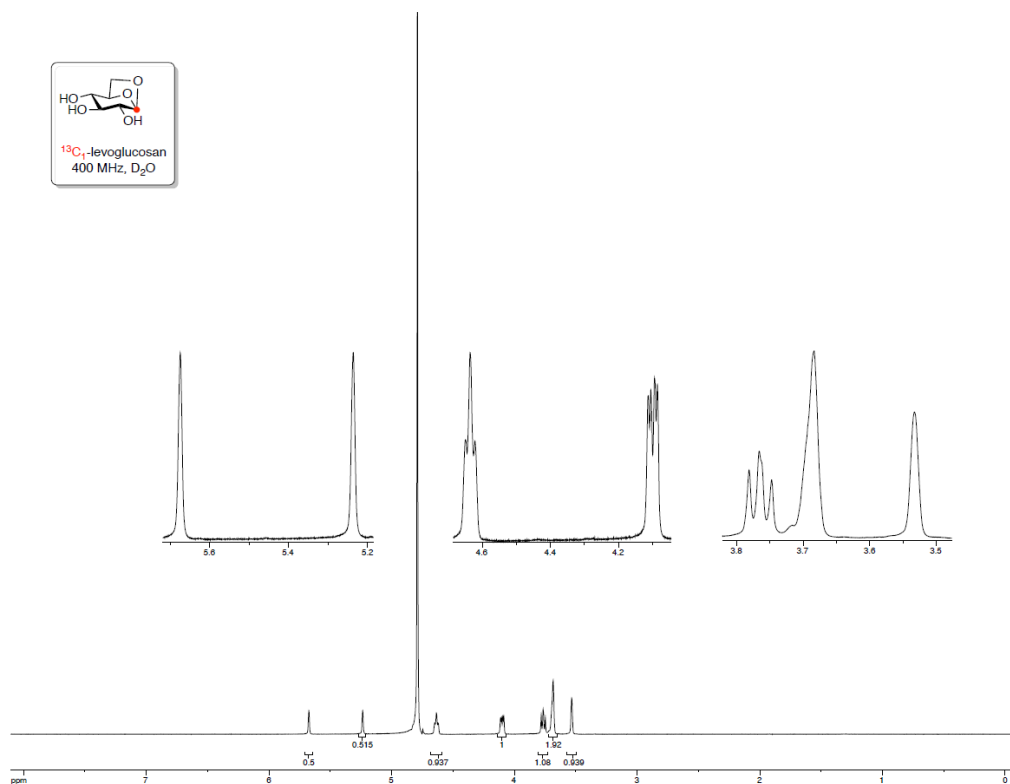


Figure 7-3 ^1H NMR of the sample.

^1H NMR (400 MHz, D_2O): δ 5.67 (s, 0.5H, H-1), 5.24 (s, 0.5H, H-1), 4.64 (t, $J = 5.6$ Hz, 1H, H-5), 4.10 (dd, $J = 7.5, 3.2$ Hz, 1H, H-6a), 3.77 (dd, $J = 7.7, 5.8$ Hz, 1H, H-6b), 3.72-3.68 (m, 2H, H-3, H-4), 3.53 (s, 1H, H-2).

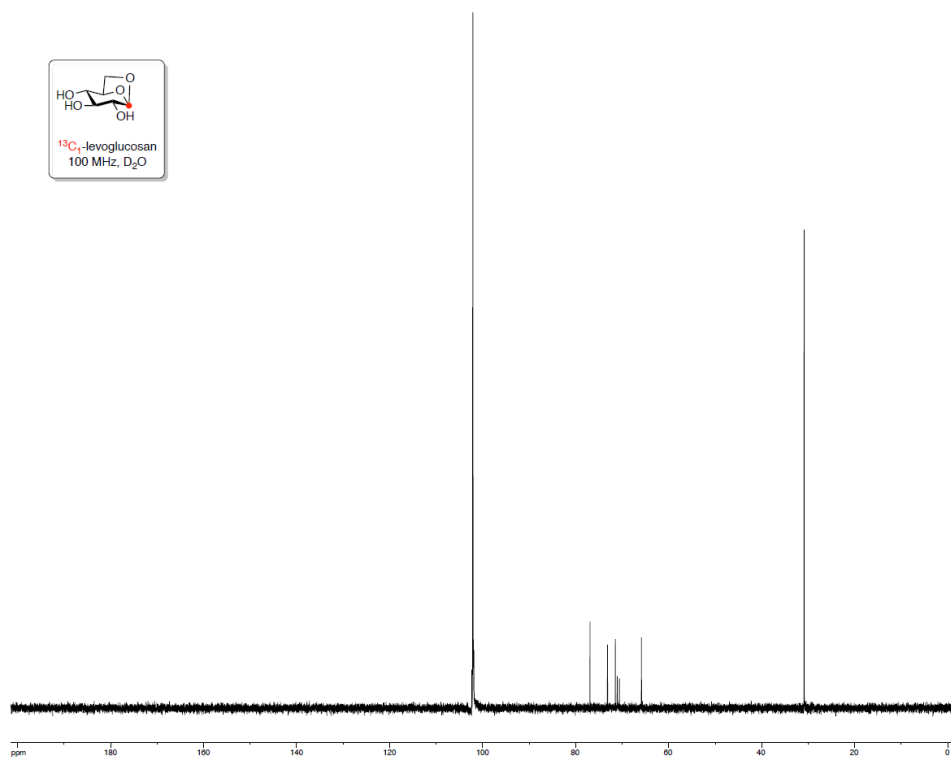


Figure 7-4 ¹³C NMR of the sample.

¹³C NMR (100 MHz, D₂O): δ 102.0 (C-1), 76.9 (H-5), 73.2 (H-3), 71.5 (H-4), 70.9 (H-2), 65.9 (H-6).

Custom synthesized ¹³C₁ cellobiosan was purchased from Omicron Biochemicals and was also characterized using ¹H and ¹³C NMR analysis as shown in Figure 7-5 and Figure 7-6.

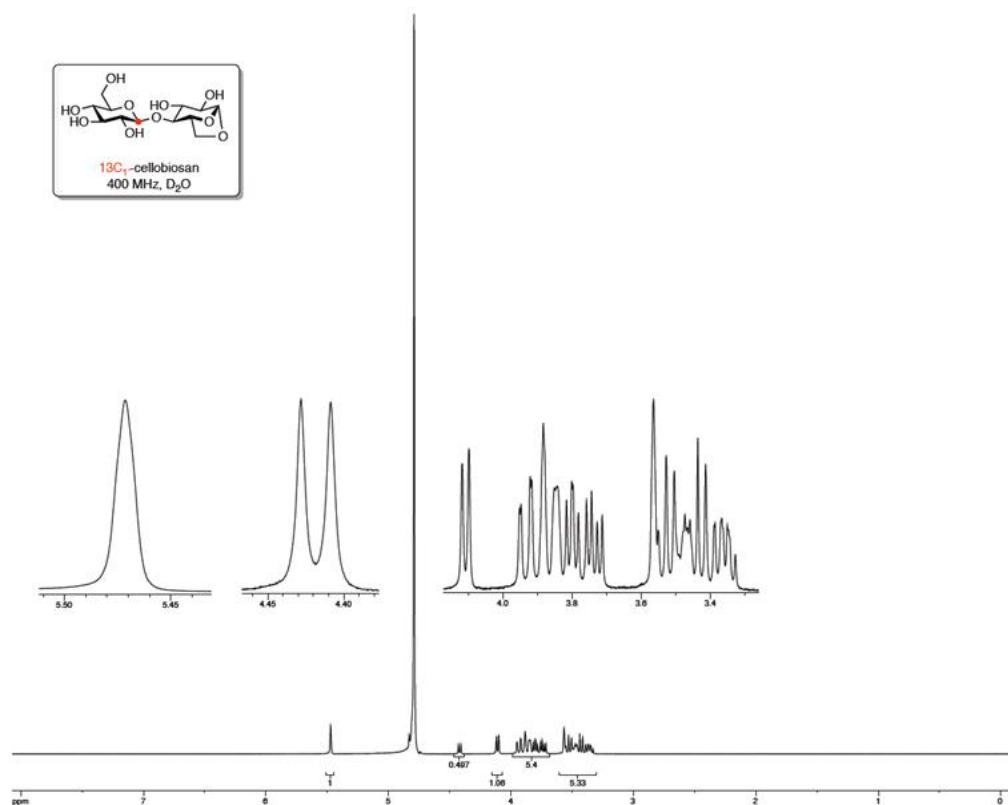


Figure 7-5 ^1H NMR of the sample provided by Omicron Biochemicals

^1H NMR (400 MHz, D_2O): δ 5.47 (s, 1H, H-1)), 4.70 (1H, H-5, buried under HOD), 4.42 (d, $J = 7.8$ Hz, 0.5H, H-1'), 4.11 (d, $J = 7.7$ Hz, 1H, H-6a), 3.95-3.71 (m, 5H, H-3, H-4, H-6b, H-6'a, H-6'b), 3.57-3.33 (m, 5H, H-2, H-2', H-3', H-4', H-5').

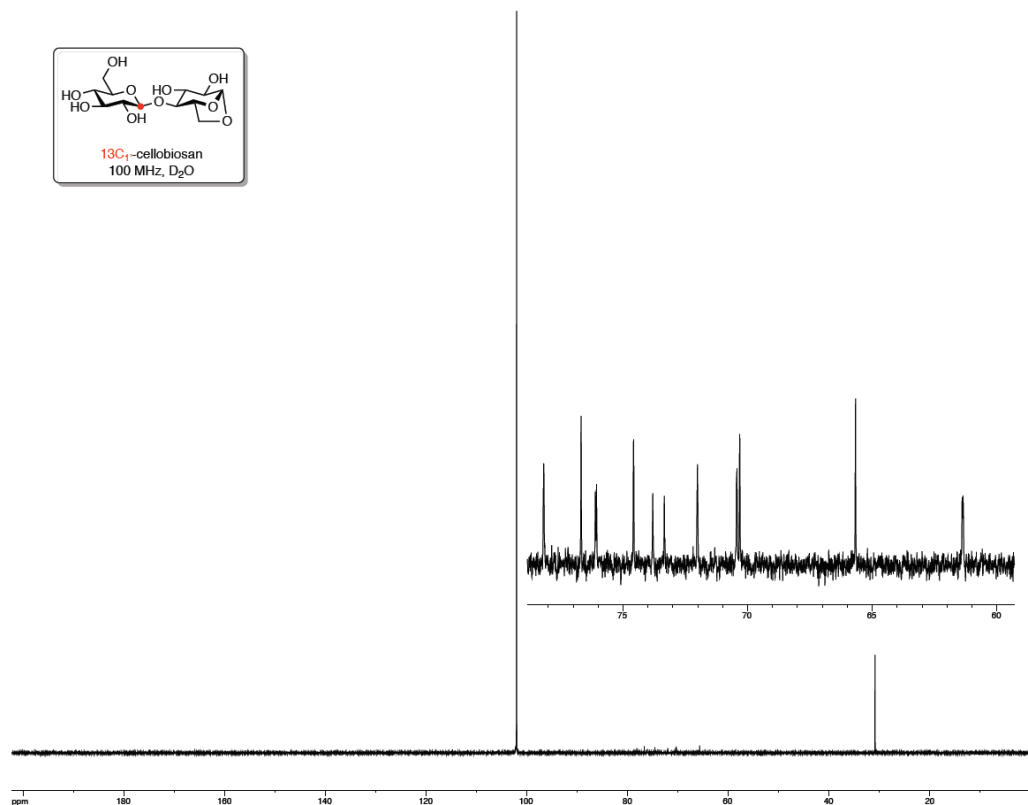


Figure 7-6 ¹³C NMR of the sample provided by Omicron Biochemicals

¹³C NMR (100 MHz, D₂O): δ 102.0 (C-1, C-1'), 78.2 (C-4), 76.7 (C-5'), 76.1 (C-3'), 74.6 (C-5), 73.6 (C-2'), 72.0 (C-3), 70.4 (C-2), 70.3 (C-4'), 65.7 (C-6), 61.3 (C-6').

Thin-film samples for PHASR reactor were prepared by depositing 50-250 microliters of reactant suspension (one weight percent) on carbon steel heating elements.

7.2.2 PHASR kinetics of cellulose.

A thin film sample of cellulose on the resistive heating element was placed between the two chambers of the PHASR reactor. Both the chambers were combined using a polytetrafluoroethylene (PTFE) compression seal such that the copper electrodes contacted the resistive heating element. Inert helium sweep gas was then turned on and flowed through the upper chamber, over the thin film samples, and out of the reactor and into the inlet of a gas chromatograph (GC) to

allow for identification and quantification of gas and volatile products. Cartridge heaters were used to maintain the reactor at 260 °C. Once the thermal pulse was applied to the sample, the resistive heating power supply turned off and the sample was rapidly quenched in under 180 milliseconds via high velocity sylterm coolant. Similar procedure was followed for PHASR kinetics experiments of anhydrosugars. The temperature profiles of the cellulose samples during PHASR experiments at five different temperatures (400, 425, 450, 475, and 500 °C) subjected to varying pulse durations (50, 100, 250, 500, 1000, 2000 ms) were recorded. The experiments were designed to meet the requirements of measuring kinetics of high temperature reactions without any transport artifacts⁵⁵. PHASR reactor was used to pyrolyze thin-film samples, while volatile products were identified and quantified using downstream gas chromatograph with integrated Polyarc™ detector^{54,84} and mass spectrometer.

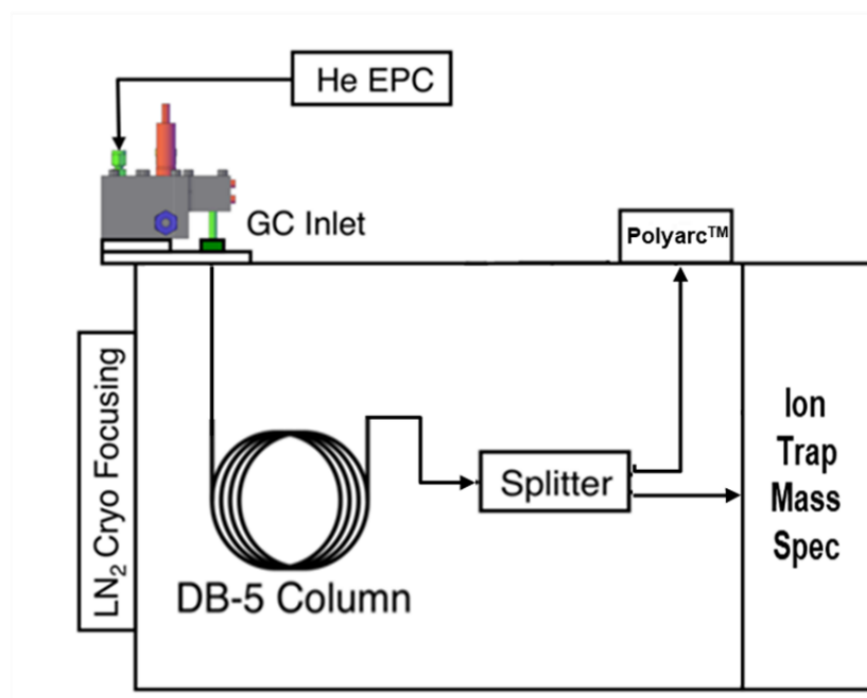


Figure 7-7 Schematic of PHASR-GC-polyarc/MS

Figure 7-7 represents schematic diagram of the experimental setup. All pyrolysis experiments were performed at least in triplicate, and the product yields are reported as averages with a 90% confidence interval to illustrate experimental error. Carbon closure with GC detectable products from pyrolysis experiments with complete conversion was approximately about 65-70 percent. Isotopic product mixture of LGA from $^{13}\text{C}_1$ cellobiosan was quantified using Agilent 220 ion trap mass spectrometer with methanol as a chemical ionization agent. Isotopic fractions of LGA were quantified by measuring intensity fraction of the corresponding parent ion.

7.2.3 Kinetics of $^{13}\text{C}_1$ cellobiosan

PHASR kinetics experiments were performed with thin film samples of $^{13}\text{C}_1$ cellobiosan at six different temperatures (380, 390, 400, 410, 420, and 420 °C). The samples were subjected to the shortest reaction pulse of 50 milliseconds to limit the conversion to < 10%. Unreacted $^{13}\text{C}_1$ cellobiosan was dissolved in HPLC grade water and quantified using a high-performance liquid chromatograph (HPLC, Shimadzu Prominence). Figure 7-8 depicts the temperature profiles of the $^{13}\text{C}_1$ cellobiosan samples during PHASR experiments at three different temperatures

(380, 400, 420 °C) subjected to the shortest possible thermal pulse (50 ms) such that the conversion is less than 10%.

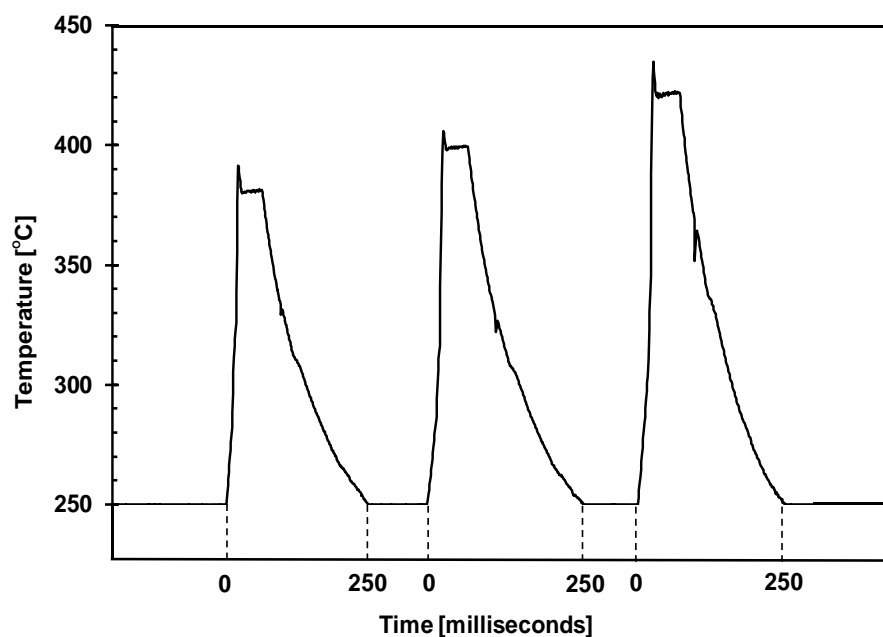


Figure 7-8 Temperature profile of thin film samples of $^{13}\text{C}_1$ cellobiosan

The $^{13}\text{C}_1$ LGA yield was quantified using GC/MS-CI quantification. With the initial reaction rate approximation, first order reaction rate coefficient (k) was calculated for $^{13}\text{C}_1$ LGA formation from $^{13}\text{C}_1$ cellobiosan as follows,

$$k (\text{sec}^{-1}) = \frac{\text{mass of } ^{13}\text{C}_1 \text{ LGA formed } (\mu\text{gms})}{\{\text{Initial mass of } ^{13}\text{C}_1 \text{ glucose monomer } (\mu\text{gms})\} \times \{\text{reaction time (sec)}\}}$$

7.3 Results and Discussion

7.3.1 Apparent kinetics of cellulose pyrolysis

Pyrolysis of cellulose samples was conducted at five different temperatures (400, 425, 450, 475, and 500 °C), and the resultant gas/vapor products were analyzed with GC-Polyarc/MS (ion trap with chemical ionization). During fragmentation, cellulose transforms into reactive liquid intermediate which decomposes further to yield final products.

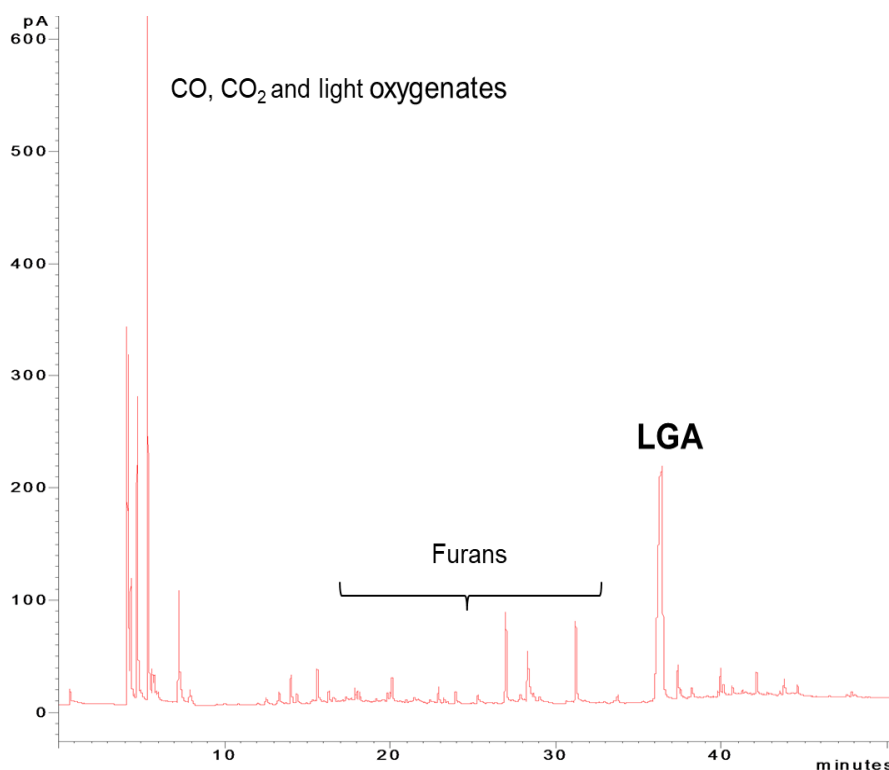


Figure 7-9 Sample Chromatogram of cellulose pyrolysis through PHASR at 500 °C.

Figure 7-9 depicts a sample chromatogram from cellulose pyrolysis highlighting major pyrolysis products formed. LGA is the most abundant primary product of cellulose fragmentation. Figure 7-10 **Error! Reference source not found.** depicts millisecond-scaled evolution profile for LGA from cellulose at 400-500 °C at 50-2000 milliseconds.

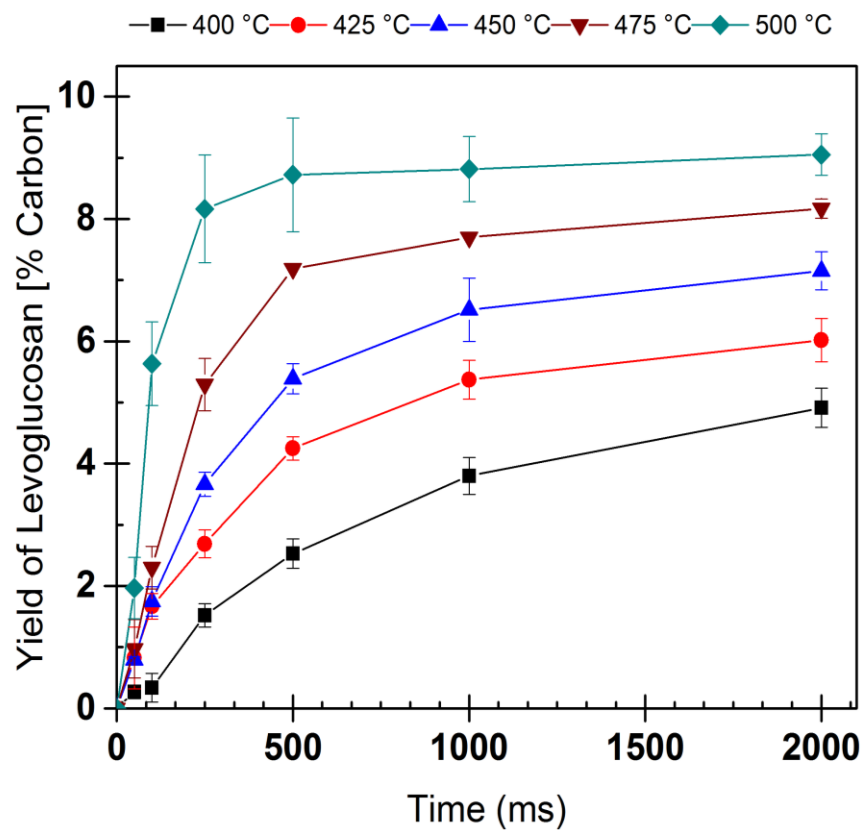
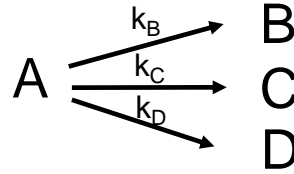


Figure 7-10 Millisecond-scaled evolution profile for LGA from cellulose at 400-500 °C at 50-2000 milliseconds.

Apparent activation energy of formation of LGA from this one reactant-multiproduct system was extracted using a coupled reactant-product evolution model. LGA is one of many products that are formed during the cellulose fragmentation reaction. The apparent kinetic parameters for the LGA formation can be extracted from coupling evolution profile of cellulose consumption and LGA formation. A simplified lumped kinetic model used for the analysis was as follows,



where, A represents reactive cellulose, B is LGA, and C, D represent other cellulose fragmentation products. k_B , k_C , and k_D are the corresponding first order rate coefficients. For simplicity, only three fragmentation products are considered in the model above. The rate of consumption of A can be represented as,

$$\frac{dC_A}{dt} = -(k_A + k_B + k_C)C_A$$

Integrating the above equation with initial time conditions of $C_A = C_{A0}$ at $t = 0$ yields,

$$C_A = C_{A0} e^{-k_g t}$$

$$C_A = C_{A0} e^{-(k_A + k_{lump}) t}$$

where, C_A is concentration of A, k_g is global kinetic rate constant and k_{lump} is a lumped kinetic rate constant of all the products except B (LGA). Similarly, rate of formation of B (LGA) can be represented as,

$$\frac{dC_B}{dt} = k_B C_A$$

Integrating the above equation with initial time conditions of $C_B = C_{B0}$ at $t = 0$ yields,

$$C_B = \frac{k_B C_{A0}}{(k_B + k_{lump})} (1 - e^{-(k_B + k_{lump})t})$$

where, C_B is the concentration of B (LGA) and k_B is the rate coefficient of LGA formation. Zhu et al measured reactant consumption profile for cellulose (C_A versus time) using cyclodextrin, a kinetic and reactive surrogate of cellulose⁸⁰. A first order reaction model with two kinetic parameters (k_B and k_{lump}) was fitted to both experimental data sets $C_A(t)$ shown in Figure 7-11 adapted from previous study⁸⁰ and $C_B(t)$ shown in Figure 7-10.

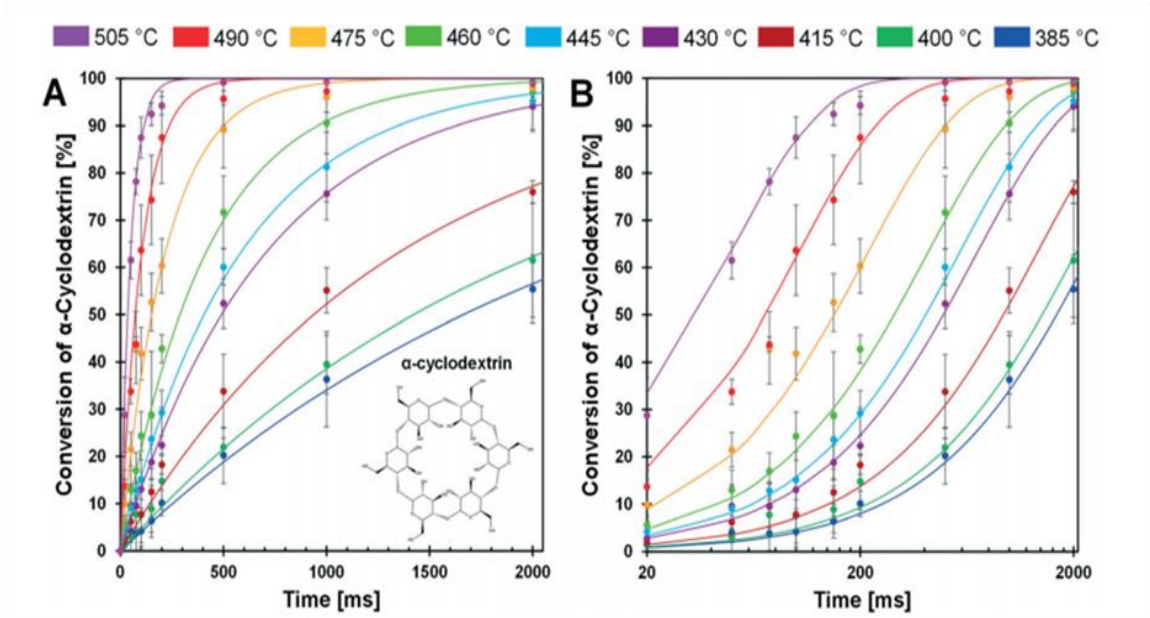


Figure 7-11 PHASR kinetics of α-cyclodextrin. Conversion of α-cyclodextrin at temperatures 385 to 505 °C.

Figure 7-12A shows that the model with k_B as a kinetic parameter is in good agreement with the experimental data of the LGA evolution profile. The rate coefficient extracted at five different temperatures are plotted on the Arrhenius plot

shown in Figure 7-12B. The apparent activation energy for LGA formation calculated from the slope of the Arrhenius plot was 34 kcal/mol.

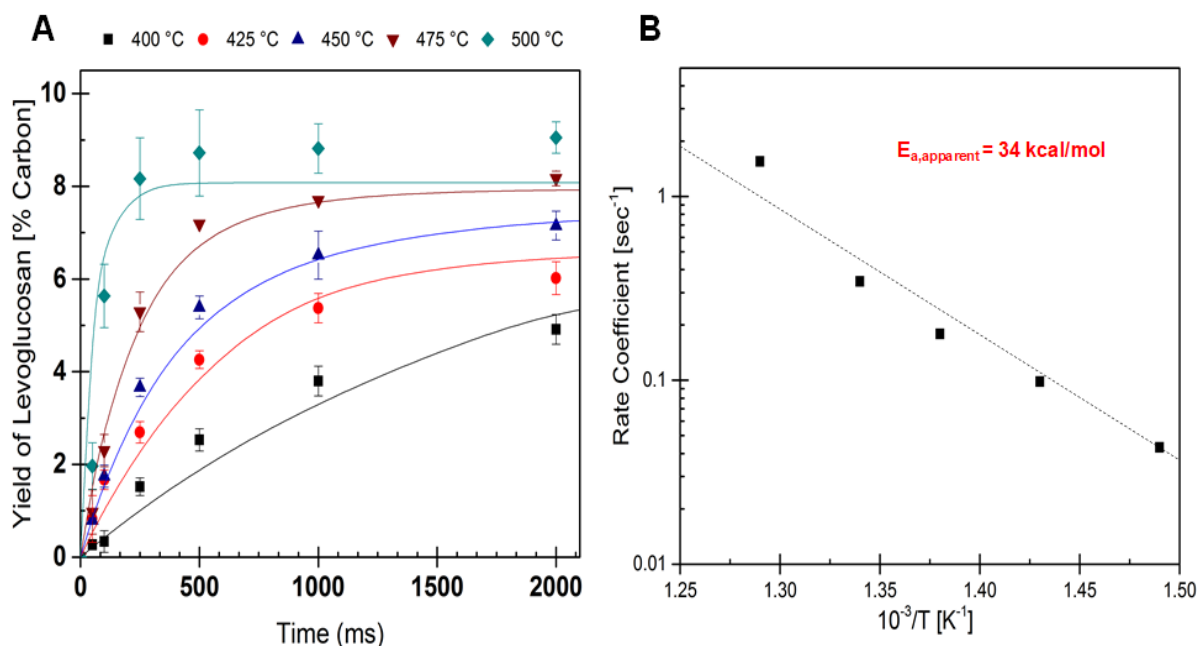


Figure 7-12 Apparent kinetics of LGA formation

A. Coupled reactant-product evolution model was fitted to time resolved experimental LGA formation profile from cellulose from 400-500 °C B. Arrhenius plot from first-order apparent kinetic rate coefficients for LGA formation.

It should be noted that the apparent barrier measured represents the convoluted effect of a series of reactions and catalysis during cellulose fragmentation and, hence cannot be directly used for mechanistic interpretations. Kinetic investigation for the individual steps in addition to apparent barriers is essential to develop a comprehensive micro-kinetic model. Recently, Zhu et al measured kinetics of initiation reaction of cellulose through glycosidic bond cleavage⁸⁰. Kinetics of intermediate cellulose melt to the final product will complete the comprehensive understanding of the overall mechanism.

7.3.2 Intermediates from cellulose pyrolysis

Anhydropolysaccharides are small chained glucose polymers with anhydrous reducing, LGA-end group. Smaller anhydrosugars such as cellobiosan and cellotriosan were observed in the volatile product fraction from cellulose pyrolysis most likely through aerosol ejection mechanism^{51,75,133}. Degenstein et al used cellotriosan as a small molecule surrogate for cellulose to study reaction pathways¹³⁴. Recently, Xu et al detected anhydropolysaccharides with degree of polymerization up to 7 in water-soluble fraction of cellulose pyrolysis intermediates¹³⁵.

Figure 7-13 depicts the LGA yield from complete pyrolysis of different anhydropolysaccharides with increasing number of glucose monomers in PHASR reactor at 500°C. The LGA yield from anhydropolysaccharides decreases from 35.5 percent carbon for cellobiosan (LGA end to Glucose monomer ratio of 1) to 13.4 percent carbon for cellopentosan (LGA end to glucose monomer ratio of 0.25). The LGA yield decreases for the anhydropolysaccharides with the increasing number of glucose monomers and approaches that of cellulose and cyclodextrin with LGA end group to glucose monomer ratio of zero. This suggests that glucose moiety in anhydropolysaccharides is chemically similar to glucose moiety in the reactive cellulose intermediate.

LGA yield from cellobiosan with glucose to LGA end ratio of 0.5 was less than 50%. This suggests that both the glucose and LGA end contributes to the product formation. The contribution of glucose monomers to the product formation becomes more prominent for the higher anhydropolysaccharides with lower LGA to glucose monomer ratios.

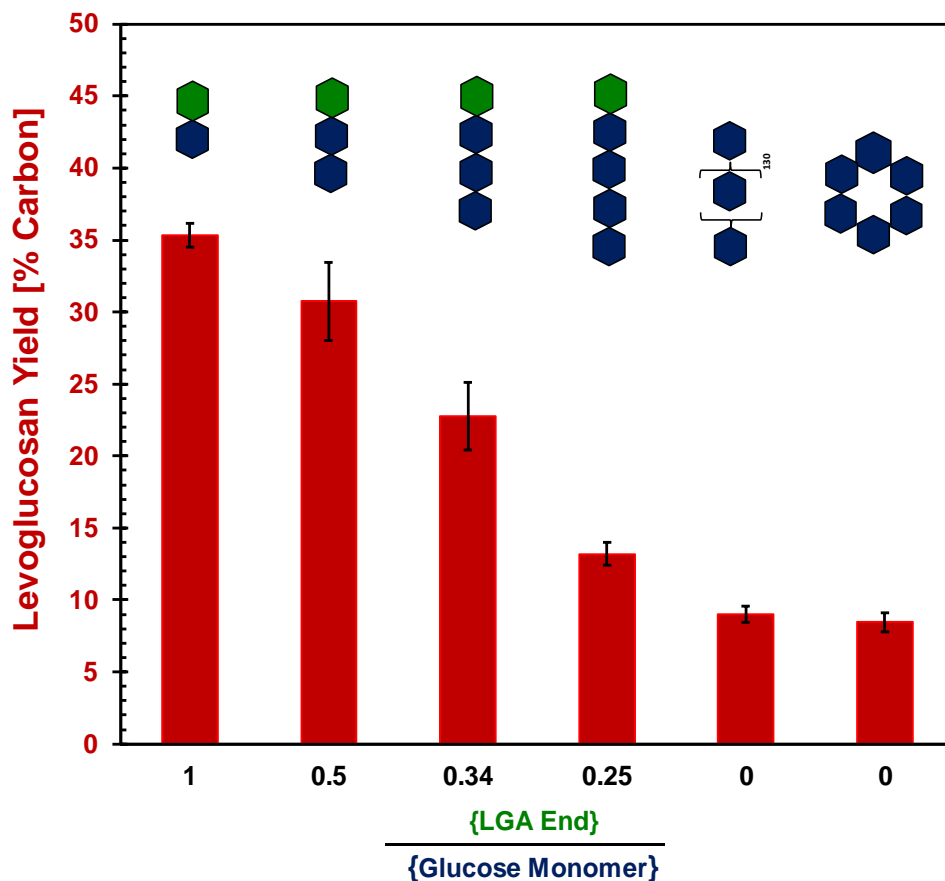


Figure 7-13 Anhydropolysaccharides: Surrogate for cellulose intermediate

7.3.3 $^{13}\text{C}_1$ Cellobiosan: a kinetic surrogate

Glucose monomer in cellobiosan was used as a chemical surrogate for cellulose intermediate to study LGA formation. To decouple the contribution of glucose and LGA end in cellobiosan, $^{13}\text{C}_1$ cellobiosan was used. Pyrolysis of $^{13}\text{C}_1$ cellobiosan yields isotopic mixture of products. For example, glucose monomer of $^{13}\text{C}_1$ cellobiosan yields $^{13}\text{C}_1$ LGA and LGA-end of $^{13}\text{C}_1$ cellobiosan yields unlabeled LGA. The contribution of glucose monomer towards LGA formation was calculated from the fraction of $^{13}\text{C}_1$ LGA in the isotopic mixture. Ion trap mass spectrometer was used with methanol as a chemical ionization agent for quantification of isotopic mixture of LGA. Fragmentation pattern of LGA from MS-CI system is shown in Figure 7-14.

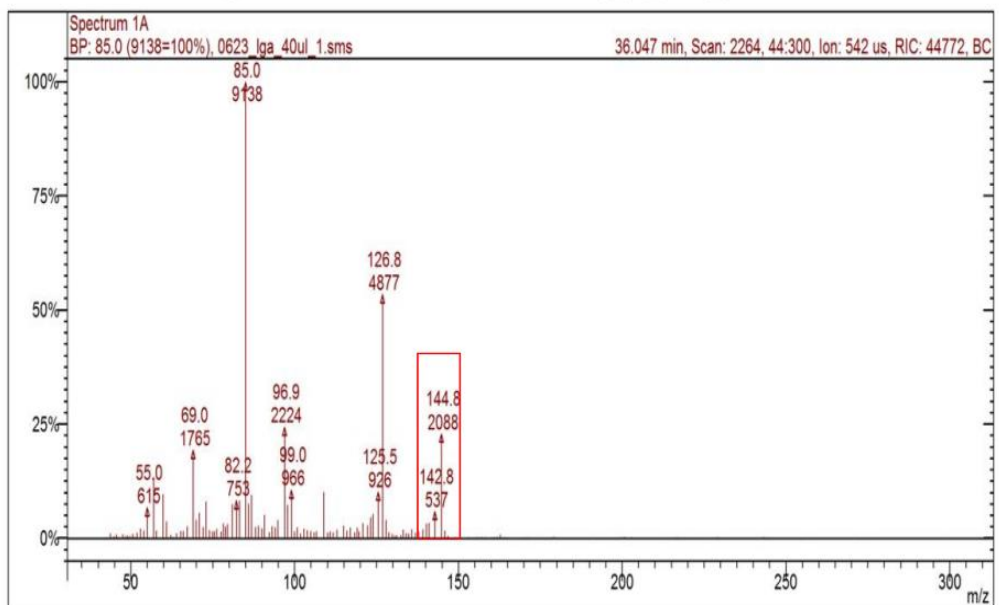


Figure 7-14 Ion fragmentation pattern of LGA peak from cellobiosan fragmentation over $40 < m/z < 300$.

In MS-CI quantification, concentration of a compound is correlated to the intensity of the corresponding ionic fragments. Therefore, the molar fraction of an isotope in its isotopic mixture can be correlated to the fraction of intensity of the corresponding ionic fragments. In case of LGA with molar mass [M] of 162, ion fragment with m/z ratio of 145 was selected for quantification which corresponds [M-17] peak resulting from a hydroxyl group removal in presence of methanol. For $^{13}\text{C}_1$ LGA with molar mass of 163, the same peak is shifted by one unit to the m/z ratio of 146.

To validate the MS-CI isotopic quantification method, thin film samples of isotopic mixtures of LGA and $^{13}\text{C}_1$ LGA were prepared with five different molar fractions. Molar fraction of $^{13}\text{C}_1$ LGA in the isotopic mixture (α) is defined as,

$$\alpha_{\text{sample}} = \frac{[^{13}\text{C}_1\text{LGA}]}{[^{13}\text{C}_1\text{LGA}] + [\text{LGA}]}$$

where, $[^{13}\text{C}_1 \text{ LGA}]$ and $[\text{LGA}]$ are the moles of $^{13}\text{C}_1$ LGA and LGA in the sample. Thin film samples of the isotopic mixture were pyrolyzed through PHASR coupled with MS-CI system at 500 °C. LGA evaporates without decomposition when pyrolyzed alone¹³⁶. LGA and $^{13}\text{C}_1$ LGA are chemically similar and cannot be resolved through gas chromatographic separation. This is evident from the sample chromatograph of LGA isotopic mixture in Figure 7-15 which shows a single peak corresponding to both LGA and $^{13}\text{C}_1$ LGA.

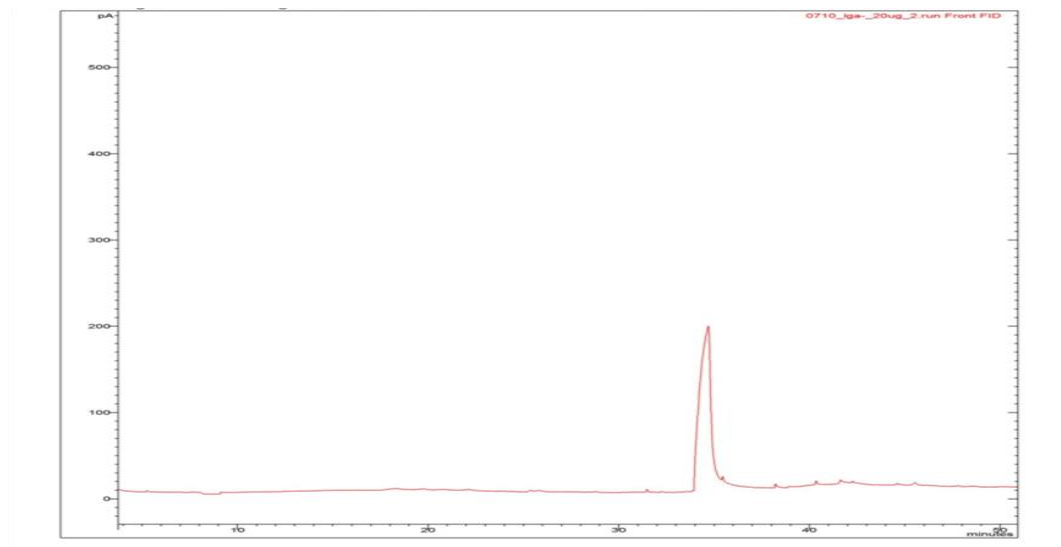


Figure 7-15 Sample GC Chromatogram of LGA isotopic mixture

Figure 7-16B depicts the ion fragmentation pattern ($142 < m/z < 148$) for all five isotopic mixture with $\alpha = 0, 0.25, 0.50, 0.75$ and 1.00 . Molar fraction of $^{13}\text{C}_1$ LGA measured from the intensity of ionic fragments is,

$$\alpha_{measured} = \frac{I_{146}}{I_{146} + I_{145}}$$

where, I_{145} and I_{146} are the intensity of the ionic fragments with m/z ratio of 145 and 146 respectively. A parity plot of α_{sample} versus $\alpha_{measured}$ for all the samples represented in Figure 7-16C shows a good agreement between the molar ratio of the sample and the measured molar ratio from MS-CI quantification over the entire

range of α_{sample} . The corresponding gas chromatographic responses (in red) indicated on secondary y axis in Figure 7-16C are consistent for all the samples which verifies complete vaporization of the sample without any losses through PHASR reactor.

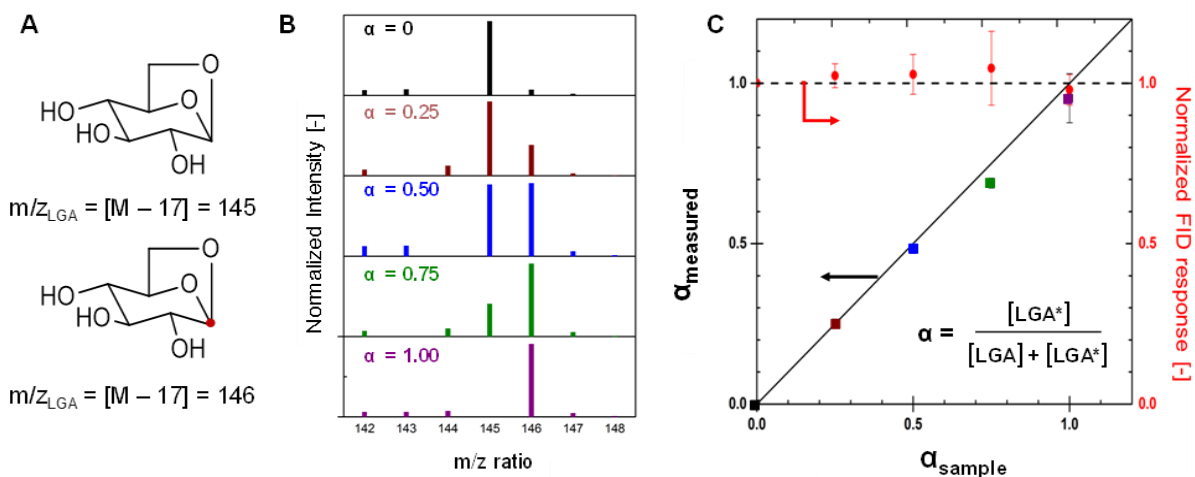


Figure 7-16 Parity plot validating MS-CI quantification method

7.3.4 Kinetics of $^{13}C_1$ LGA formation from $^{13}C_1$ Cellobiosan

PHASR kinetics experiments were performed with thin film samples of $^{13}C_1$ cellobiosan at six different temperatures (380, 390, 400, 410, 420, and 420 °C). Samples were subjected to the shortest reaction pulse of 50 milliseconds to limit the conversion to less than 10%. Figure 7-17 and Figure 7-18 depict sample GC chromatogram and ion fragmentation pattern of the isotopic mixture of LGA peak from cellobiosan (top) and $^{13}C_1$ cellobiosan (bottom). Non-LGA peaks in GC chromatogram in Figure 7-17 indicate that both glucose monomer and LGA-end of cellobiosan can yield non-LGA products like furans, light oxygenates. The intensity of the peak at m/z of 146 for LGA from cellobiosan in Figure 7-18 (top) was found to be approximately 5% of the intensity of the peak at m/z of 145. This was consistent for all unlabeled LGA fragmentation (Figure 7-16B with $\alpha = 0$) and was taken into account during the quantification of the isotopic fractions.

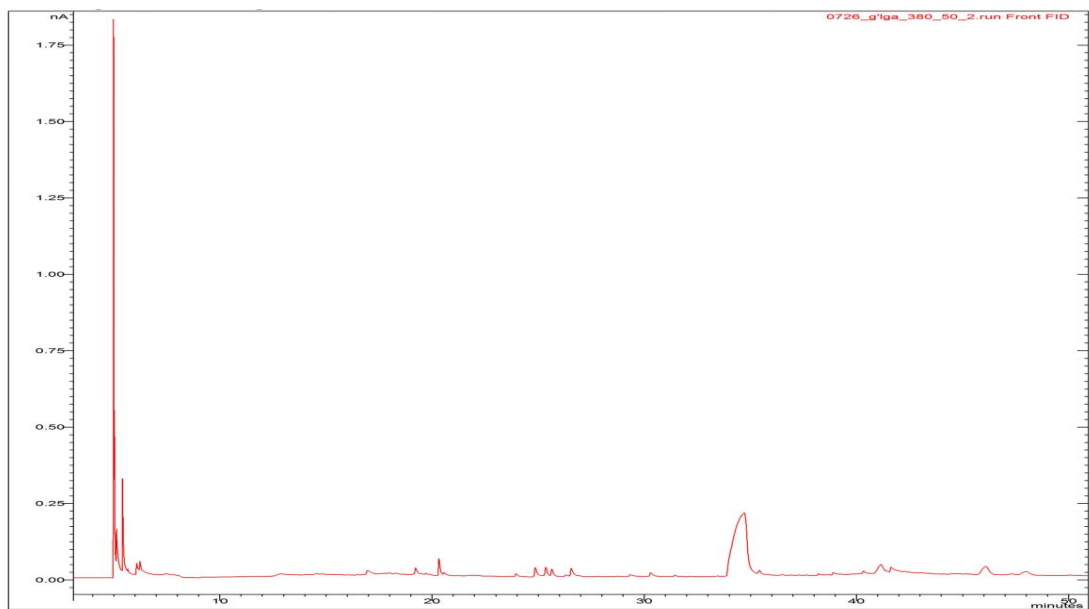


Figure 7-17 Sample GC Chromatogram of $^{13}\text{C}_1$ Cellobiosan pyrolysis at 380C

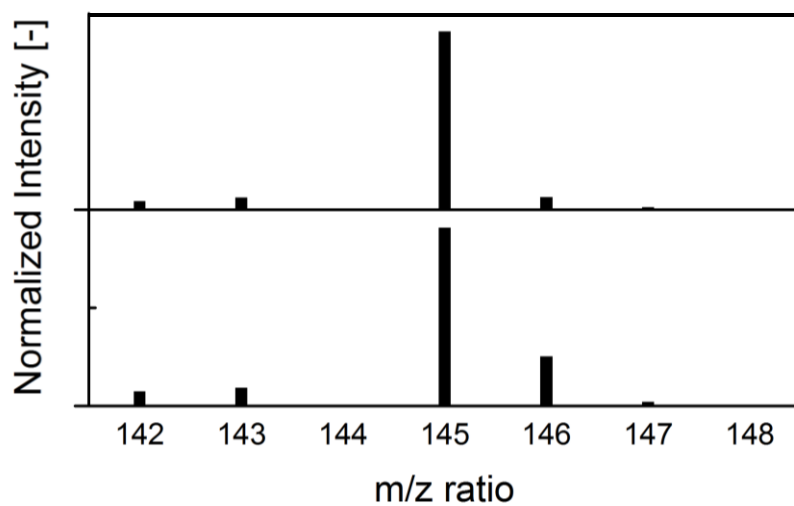


Figure 7-18 Mass spec fragmentation pattern of the LGA isotopic mixture after pyrolysis of cellobiosan (top) and $^{13}\text{C}_1$ cellobiosan (bottom).

Initial rates of reaction for $^{13}\text{C}_1$ LGA formation from $^{13}\text{C}_1$ cellobiosan was calculated from MS-CI quantification method. The conversions were less than 10% and hence through initial rate approximation, first order rate constant was

calculated as per equation in Section 7.2.3. Figure 7-19 represents the Arrhenius plot for the $^{13}\text{C}_1$ LGA formation from $^{13}\text{C}_1$ cellobiosan. The activation energy, E_a , calculated from the slope of the plot was 26.9 ± 1.9 kcal/mol and the pre-exponential factor, k_0 , calculated from the intercept was $4.2 \times 10^7 \text{ sec}^{-1}$. The activation energy represents the energy barrier for LGA formation with contribution only from glucose part of cellobiosan. The kinetic parameters extracted here have contribution from only the product formation reaction step without any transport artifacts and other convoluted reactions. Therefore, these experimental values of kinetic parameters can be compared directly to the corresponding values of different proposed mechanisms calculated through density functional theory (DFT) studies.

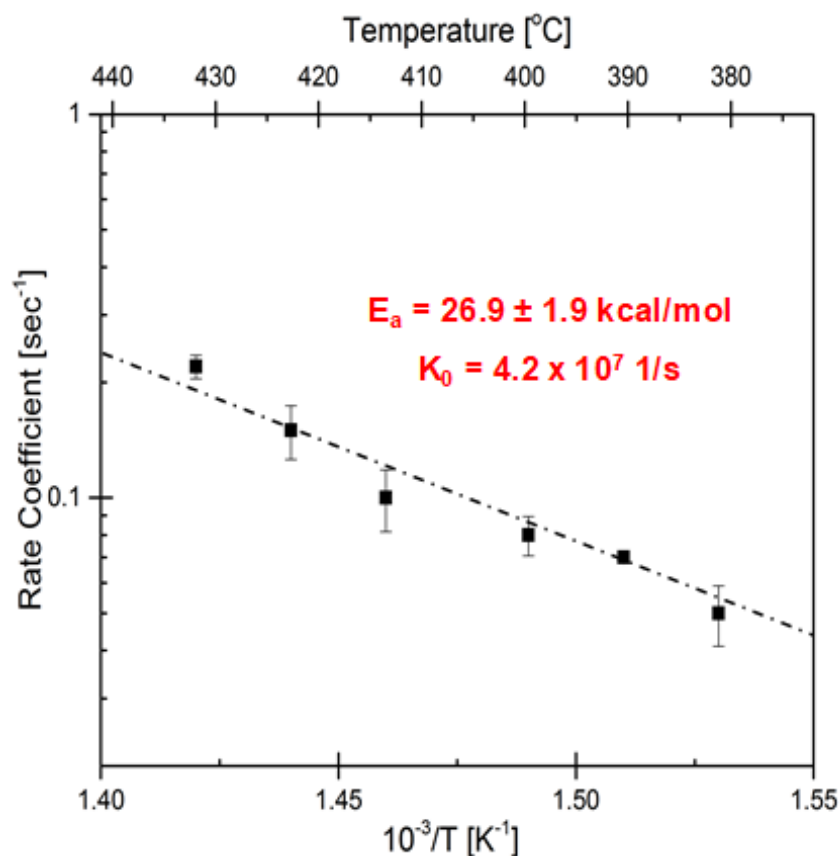


Figure 7-19 Arrhenius plot for the $^{13}\text{C}_1$ LGA formation from $^{13}\text{C}_1$ cellobiosan

Glycosidic bond in cellobiosan is the reactive site in the molecule. There are two ways to form monomers from cellobiosan either via glycosidic bond cleavage to form intermediates species or through concerted mechanism.

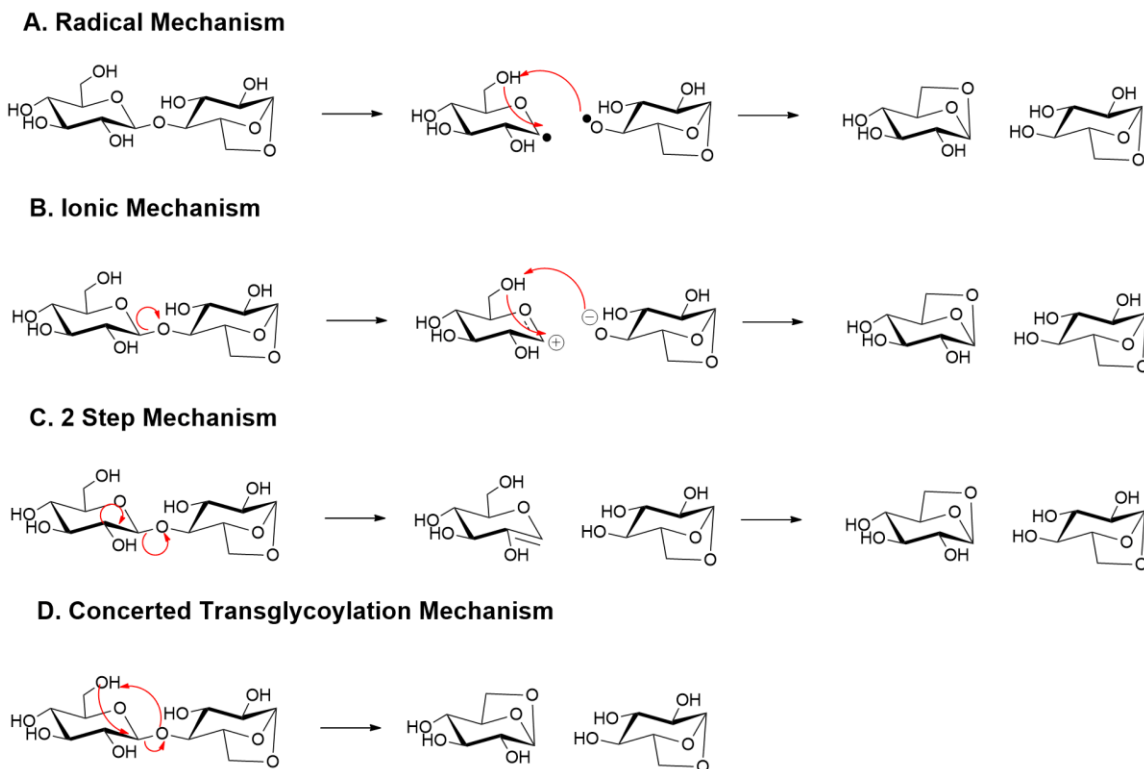


Figure 7-20 Proposed Mechanisms of LGA formation from Cellobiosan

Figure 7-20 depicts four proposed mechanisms for LGA formation from cellobiosan. Radical mechanism involves initial homolytic cleavage of the glycosidic bond of cellobiosan to result in two reactive radical species⁹⁷. Ponder et al. proposed a mechanism with an ionic intermediate to yield LGA¹³⁷. Assary and Curtiss recently proposed a two-step mechanism for formation of levoglucosan from cellobiose. In the first step, the glycosidic bond is broken and a carbon-carbon double bond is formed. Recent work done by the Broadbelt group^{29,31} and Hosoya et al.^{36,130} has led to a concerted mechanism, transglycosylation, which results in formation of LGA from cellobiosan. A comparative study by Mayes et al.²⁹ using DFT showed that this mechanism will have a significantly lower barrier than either

homolytic or heterolytic cleavage. The barrier for transglycosylation mechanism for cellobiose calculated by Mayes et al was 52.7 kcal/mol which is still significantly higher as compared to experimentally measured value of 26.9 kcal/mol. This disparity in the experimental and computational energy barrier of the reaction suggests the possibility of new or modified version of the proposed mechanisms.

One such possible mechanism is the hydroxyl catalyzed transglycosylation. Reactive hydroxyl groups present in cellobiosan can activate the glycosidic bond cleavage and catalyze LGA formation. This hypothesis is analogous to the previously postulated mechanism by Seshadri et al.¹²⁸ and Hosoya et al.¹³⁰ who considered hydroxyl groups assisting in reactions with glucose to form LGA using water molecules to represent hydroxyl groups. The mechanism was indirectly validated from the co-pyrolysis experiment of cellulose and fructose discussed in the previous chapter which resulted in the increased LGA yield in presence of hydroxyl group in transport limited reactors. Detailed computational analysis with density functional theory calculations will be performed to validate the mechanism.

Chapter 8 Conclusions

Lignocellulosic biomass pyrolyzes at high temperatures to thermally fragment biopolymers like cellulose to volatile organic compounds. The fragmentation process is complex, multi-phase and includes myriad of reactions occurring on millisecond timescale. The primary goal of this thesis was to develop mechanistic insights of biomass fragmentation using novel microreactor systems, **a.** Quantitative Carbon Detector (QCD) **b.** Pulse Heated Analysis of Solid Reactions (PHASR).

QCD is an integrated microreactor system for the for use with current gas chromatography technique for calibration-free quantitation of complex biomass pyrolysis products. QCD was designed with combined heating, catalytic combustion, methanation and gas co-reactant mixing within a single modular reactor fully converts all analytes to methane (>99.9%) within a thermodynamic operable regime. Residence time distribution of the QCD revealed negligible loss in chromatographic resolution consistent with fine separation of complex mixtures including biomass pyrolysis products.

In the PHASR (Pulse-Heated Analysis of Solid Reactions) method, thin film biomass samples are subjected to millisecond thermal pulses of square waves with prescribed temperature and time interval. PHASR reactor allows Implementation of the PHASR technique employing *seperando* principles enabled decoupling of reaction kinetics from chemical analysis. The technique was compared with conventional analytical reactors and was validated using five requirements of measuring biomass pyrolysis kinetics. PHASR capabilities were demonstrated by measuring the time-resolved evolution of six major chemical products from Loblolly pine pyrolysis over a temperature range of 400 °C to 500 °C.

PHASR kinetics experiments were used to understand cellulose fragmentation chemistry to form Levoglucosan (LGA). The variation of the observed yield of LGA from cellulose pyrolysis was experimentally investigated. The reactor configuration and experimental conditions including cellulose sample size were found to have a significant effect on the yield of LGA. Co-pyrolysis experiments of cellulose and fructose in the PHASR reactor presented indirect experimental evidence of previously postulated catalytic

effects of hydroxyl groups in glycosidic bond cleavage for LGA formation in transport-limited reactor systems. Apparent kinetic parameters were extracted from the time resolved data of LGA formation from cellulose.

The elemental step towards LGA formation was decoupled from the initiation reaction during cellulose fragmentation by identifying cellobiosan as a surrogate for cellulose pyrolysis intermediate. Contribution from glucose monomer in cellobiosan towards LGA formation was measured using $^{13}\text{C}_1$ cellobiosan and MS-CI quantification method. First order rate coefficients for LGA formation from glucose monomer of cellobiosan were measured from the initial rate approximation at six different temperatures. The activation energy E_a calculated from the slope of the plot was 26.9 ± 1.9 kcal/mol and the preexponential factor k_0 . Calculated from the intercept was $4.2 \times 10^7 \text{ sec}^{-1}$. These kinetic parameters were found to be lower than the corresponding values for the proposed mechanisms or LGA formation calculated from DFT studies.

8.1 Future work

8.1.1 Computational analysis

A significant mismatch between the experimentally measured value of activation energy of LGA formation and DFT based values of activation energies of various proposed mechanisms of LGA formation suggests a possibility of new or modified mechanism of LGA formation. XRD^{115,138–143} studies on the crystalline forms suggest that cellulose chains are arranged parallel to each other forming sheets. The presence of such a well packed structure indicates that it is possible for hydroxyl groups in adjoining layers to have an influence on pyrolysis chemistry particularly at low temperatures when breakdown of the crystal structure is not as severe. Seshadri et al.¹²⁸ and Hosoya et al.¹³⁰ were the first to consider hydroxyl groups assisting in reactions with glucose to form LGA using water molecules to represent hydroxyl groups. They reported activation energies dropping from ~47 kcal/mol to 36-40 kcal/mol. While this is a significant drop it is still not as low as reported in experiments (~27 kcal/mol), indicating the need for further studies.

8.1.2 Mechanism of non-LGA products

Cellulose pyrolysis leads to formation of high value products like LGA and furans as well as relatively low value products like light oxygenates such as glycolaldehyde and formaldehyde. This thesis gave insights into the mechanism for initiation and LGA formation which can serve as a benchmark for investigation of mechanism of formation of other class of products from cellulose fragmentation. Subsequently mechanisms of pyrolysis of other components of biomass such as lignin and hemicellulose can be investigated. Catalytic effects of naturally present alkali and alkaline earth metal salts on pyrolysis chemistry can be quantified. Comparing kinetics of biomass decomposition to that of individual components can elucidate the possible interactions between the components and their effect on the fragmentation reactions. These studies would help us predict conditions that would be optimal for maximizing yields of desired products.

8.1.3 Other applications

Analytical microreactor techniques discussed in this thesis have wide applications apart from biomass pyrolysis. The QCD technique can be used for the analysis of unresolved complex mixtures apart from bio-oil. The performance of QCD (now commercialized as Polyarc detector) was found to be unaffected in presence of heteroatoms such as Silicon and Sulfur typically present in the analysis of consumer products, environmental contaminants, and fossil fuels. Similarly, PHASR experiments can be used to measure kinetics of other rapid, complex reaction systems involving solid or viscous fluids.

Chapter 9 Bibliography

- (1) Huber, G. W.; Iborra, S.; Corma, A. Synthesis of Transportation Fuels from Biomass: Chemistry, Catalysts, and Engineering. *Chemical Reviews*. 2006, pp 4044–4098.
- (2) Dang, Q.; Hu, W.; Rover, M.; Brown, R. C.; Wright, M. M. Economics of Biofuels and Bioproducts from an Integrated Pyrolysis Biorefinery. *Biofuels, Bioprod. Biorefining* **2016**, 10 (6), 790–803.
- (3) Huber, G. W.; Brown, R. C. Prospects and Challenges of Pyrolysis Technologies for Biomass Conversion. *Energy Technology*. 2017, pp 5–6.
- (4) Kan, T.; Strezov, V.; Evans, T. J. Lignocellulosic Biomass Pyrolysis: A Review of Product Properties and Effects of Pyrolysis Parameters. *Renewable and Sustainable Energy Reviews*. May 2016, pp 126–1140.
- (5) Umeki, K.; Yamamoto, K.; Namioka, T.; Yoshikawa, K. High Temperature Steam-Only Gasification of Woody Biomass. *Appl. Energy* **2010**, 87 (3), 791–798.
- (6) Zanzi, R.; Sjöström, K.; Björnbom, E. Rapid Pyrolysis of Agricultural Residues at High Temperature. *Biomass and Bioenergy* **2002**, 23 (5), 357–366.
- (7) Bridgwater, A. V.; Meier, D.; Radlein, D. An Overview of Fast Pyrolysis of Biomass. *Org. Geochem.* **1999**, 30 (12), 1479–1493.
- (8) Karagöz, S.; Bhaskar, T.; Muto, A.; Sakata, Y.; Oshiki, T.; Kishimoto, T. Low-Temperature Catalytic Hydrothermal Treatment of Wood Biomass: Analysis of Liquid Products. *Chem. Eng. J.* **2005**, 108 (1–2), 127–137.
- (9) Parthasarathy, P.; Narayanan, K. S. Hydrogen Production from Steam Gasification of Biomass: Influence of Process Parameters on Hydrogen Yield - A Review. *Renewable Energy*. Pergamon June 1, 2014, pp 570–579.
- (10) Heidenreich, S.; Foscolo, P. U. New Concepts in Biomass Gasification. *Progress in Energy and Combustion Science*. Pergamon February 1, 2015, pp 72–95.

- (11) Stefanidis, S. D.; Kalogiannis, K. G.; Iliopoulou, E. F.; Michailof, C. M.; Pilavachi, P. A.; Lappas, A. A. A Study of Lignocellulosic Biomass Pyrolysis via the Pyrolysis of Cellulose, Hemicellulose and Lignin. *J. Anal. Appl. Pyrolysis* **2014**, *105*, 143–150.
- (12) Chen, W. H.; Peng, J.; Bi, X. T. A State-of-the-Art Review of Biomass Torrefaction, Densification and Applications. *Renewable and Sustainable Energy Reviews*. Pergamon April 1, 2015, pp 847–866.
- (13) Batidzirai, B.; Mignot, A. P. R.; Schakel, W. B.; Junginger, H. M.; Faaij, A. P. C. Biomass Torrefaction Technology: Techno-Economic Status and Future Prospects. *Energy* **2013**, *62*, 196–214.
- (14) Carlson, T. R.; Vispute, T. P.; Huber, G. W. Green Gasoline by Catalytic Fast Pyrolysis of Solid Biomass Derived Compounds. *ChemSusChem* **2008**, *1* (5), 397–400.
- (15) Bridgwater, A. V. Renewable Fuels and Chemicals by Thermal Processing of Biomass. *Chem. Eng. J.* **2003**, *91* (2–3), 87–102.
- (16) Iea, I. E. A. Biofuels for Transport. *Transport* **2004**, No. December, 216.
- (17) Demirbaş, A.; Arin, G. An Overview of Biomass Pyrolysis. *Energy Sources* **2002**, *24* (5), 471–482.
- (18) Demirbas, M. F.; Balat, M. Biomass Pyrolysis for Liquid Fuels and Chemicals: A Review. *J. Sci. Ind. Res.* **2007**.
- (19) Dauenhauer, P. J.; Colby, J. L.; Balonek, C. M.; Suszynski, W. J.; Schmidt, L. D. Reactive Boiling of Cellulose for Integrated Catalysis through an Intermediate Liquid. *Green Chem.* **2009**, *11* (10), 1555.
- (20) Sharma, A.; Pareek, V.; Zhang, D. Biomass Pyrolysis - A Review of Modelling, Process Parameters and Catalytic Studies. *Renewable and Sustainable Energy Reviews*. Elsevier 2015, pp 1081–1096.

- (21) Anca-Couce, A. Reaction Mechanisms and Multi-Scale Modelling of Lignocellulosic Biomass Pyrolysis. *Prog. Energy Combust. Sci.* **2016**, *53*, 41–79.
- (22) Shurong Wang*, Bin Ru, Haizhou Lin, Gongxin Dai, Y. W. and Z. L.; State. Kinetic Study on Pyrolysis of Biomass Components: A Critical Review. *Curr. Org. Chem.* **2016**, *20*, 2489–2513.
- (23) Di Blasi, C. Modeling Chemical and Physical Processes of Wood and Biomass Pyrolysis. *Progress in Energy and Combustion Science*. February 2008, pp 47–90.
- (24) Lédé, J. Cellulose Pyrolysis Kinetics: An Historical Review on the Existence and Role of Intermediate Active Cellulose. *J. Anal. Appl. Pyrolysis* **2012**, *94*, 17–32.
- (25) Williams, C. L.; Emerson, R. M.; Tumuluru, J. S. Biomass Compositional Analysis for Conversion to Renewable Fuels and Chemicals. In *Biomass Volume Estimation and Valorization for Energy*; Tumuluru, J. S., Ed.; InTech: Rijeka, 2017.
- (26) Mettler, M. S.; Vlachos, D. G.; Dauenhauer, P. J. Top Ten Fundamental Challenges of Biomass Pyrolysis for Biofuels. *Energy Environ. Sci.* **2012**, *5* (7), 7797.
- (27) Burnham, A. K.; Zhou, X.; Broadbelt, L. J. Critical Review of the Global Chemical Kinetics of Cellulose Thermal Decomposition. *Energy & Fuels* **2015**, *29* (5), 2906–2918.
- (28) Krumm, C.; Pfaendtner, J.; Dauenhauer, P. J. Millisecond Pulsed Films Unify the Mechanisms of Cellulose Fragmentation. *Chem. Mater.* **2016**, *28* (9), 3108–3114.
- (29) Mayes, H. B.; Broadbelt, L. J. Unraveling the Reactions That Unravel Cellulose. *J. Phys. Chem. A* **2012**, *116* (26), 7098–7106.
- (30) Mayes, H. B.; Nolte, M. W.; Beckham, G. T.; Shanks, B. H.; Broadbelt, L. J. The Alpha-Bet(a) of Glucose Pyrolysis: Computational and Experimental Investigations of 5-Hydroxymethylfurfural and Levoglucosan Formation Reveal

- Implications for Cellulose Pyrolysis. *ACS Sustain. Chem. Eng.* **2014**, 2 (6), 1461–1473.
- (31) Zhou, X.; Nolte, M. W.; Shanks, B. H.; Broadbelt, L. J. Experimental and Mechanistic Modeling of Fast Pyrolysis of Neat Glucose-Based Carbohydrates. 2. Validation and Evaluation of the Mechanistic Model. *Ind. Eng. Chem. Res.* **2014**, 53 (34), 13290–13301.
- (32) Agarwal, V.; Dauenhauer, P. J.; Huber, G. W.; Auerbach, S. M. Ab Initio Dynamics of Cellulose Pyrolysis: Nascent Decomposition Pathways at 327 and 600 °C. *J. Am. Chem. Soc.* **2012**, 134 (36), 14958–14972.
- (33) Robinson, P. J.; Holbrook, K. a. Chemical Kinetics and Reaction Mechanisms. **1972**.
- (34) Wiberg, K. B. The Deuterium Isotope Effect. *Chem. Rev.* **1955**, 55 (4), 713–743.
- (35) Westheimer, F. H. The Magnitude of the Primary Kinetic Isotope Effect for Compounds of Hydrogen and Deuterium. *Chem. Rev.* **1961**, 61 (3), 265–273.
- (36) Hosoya, T.; Sakaki, S. Levoglucosan Formation from Crystalline Cellulose: Importance of a Hydrogen Bonding Network in the Reaction. *ChemSusChem* **2013**, 6 (12), 2356–2368.
- (37) Williams, C. L.; Westover, T. L.; Petkovic, L. M.; Matthews, A. C.; Stevens, D. M.; Nelson, K. R. Determining Thermal Transport Properties for Softwoods under Pyrolysis Conditions. *ACS Sustain. Chem. Eng.* **2017**, 5 (1), 1019–1025.
- (38) SJÖSTRÖM, E. WOOD-BASED CHEMICALS AND PULPING BY-PRODUCTS. In *Wood Chemistry*; 1993.
- (39) Mochidzuki, K.; Sakoda, A.; Suzuki, M. Liquid-Phase Thermogravimetric Measurement of Reaction Kinetics of the Conversion of Biomass Wastes in Pressurized Hot Water: A Kinetic Study. *Advances in Environmental Research*. Pergamon January 1, 2003, pp 421–428.

- (40) El-Sayed, S. A.; Mostafa, M. E. Pyrolysis Characteristics and Kinetic Parameters Determination of Biomass Fuel Powders by Differential Thermal Gravimetric Analysis (TGA/DTG). *Energy Convers. Manag.* **2014**, *85*, 165–172.
- (41) Pecha, M. B.; Montoya, J. I.; Ivory, C.; Chejne, F.; Garcia-Perez, M. Modified Pyroprobe Captive Sample Reactor: Characterization of Reactor and Cellulose Pyrolysis at Vacuum and Atmospheric Pressures. *Ind. Eng. Chem. Res.* **2017**, *56* (18), 5185–5200.
- (42) Thangalazhy-Gopakumar, S.; Adhikari, S.; Gupta, R. B.; Tu, M.; Taylor, S. Production of Hydrocarbon Fuels from Biomass Using Catalytic Pyrolysis under Helium and Hydrogen Environments. *Bioresour. Technol.* **2011**, *102* (12), 6742–6749.
- (43) Li, J.; Li, X.; Zhou, G.; Wang, W.; Wang, C.; Komarneni, S.; Wang, Y. Catalytic Fast Pyrolysis of Biomass with Mesoporous ZSM-5 Zeolites Prepared by Desilication with NaOH Solutions. *Appl. Catal. A Gen.* **2014**, *470*, 115–122.
- (44) Zmiewski, A. M.; Hammer, N. L.; Garrido, R. A.; Misera, T. G.; Coe, C. G.; Satrio, J. A. Exploring the Products from Pinewood Pyrolysis in Three Different Reactor Systems. *Energy and Fuels* **2015**, *29* (9), 5857–5864.
- (45) Proano-Aviles, J.; Lindstrom, J. K.; Johnston, P. A.; Brown, R. C. Heat and Mass Transfer Effects in a Furnace-Based Micropyrolyzer. *Energy Technol.* **2017**, *5* (1), 189–195.
- (46) Patwardhan, P. R.; Satrio, J. A.; Brown, R. C.; Shanks, B. H. Product Distribution from Fast Pyrolysis of Glucose-Based Carbohydrates. *J. Anal. Appl. Pyrolysis* **2009**, *86* (2), 323–330.
- (47) Xue, Y.; Kelkar, A.; Bai, X. Catalytic Co-Pyrolysis of Biomass and Polyethylene in a Tandem Micropyrolyzer. *Fuel* **2015**, *166*, 227–236.
- (48) Sophonrat, N.; Sandström, L.; Johansson, A. C.; Yang, W. Co-Pyrolysis of Mixed Plastics and Cellulose: An Interaction Study by Py-GC×GC/MS. *Energy and Fuels*

2017, *31* (10), 11078–11090.

- (49) Hoekstra, E.; van Swaaij, W. P. M.; Kersten, S. R. A.; Hogendoorn, K. J. A. Fast Pyrolysis in a Novel Wire-Mesh Reactor: Design and Initial Results. *Chem. Eng. J.* **2012**, *191*, 45–58.
- (50) Hoekstra, E.; Van Swaaij, W. P. M.; Kersten, S. R. A.; Hogendoorn, K. J. A. Fast Pyrolysis in a Novel Wire-Mesh Reactor: Decomposition of Pine Wood and Model Compounds. *Chem. Eng. J.* **2012**, *187*, 172–184.
- (51) Gong, X.; Yu, Y.; Gao, X.; Qiao, Y.; Xu, M.; Wu, H. Formation of Anhydro-Sugars in the Primary Volatiles and Solid Residues from Cellulose Fast Pyrolysis in a Wire-Mesh Reactor. *Energy and Fuels* **2014**, *28* (8), 5204–5211.
- (52) Mettler, M. S.; Mushrif, S. H.; Paulsen, A. D.; Javadekar, A. D.; Vlachos, D. G.; Dauenhauer, P. J. Revealing Pyrolysis Chemistry for Biofuels Production: Conversion of Cellulose to Furans and Small Oxygenates. *Energy Environ. Sci.* **2012**, *5*, 5414.
- (53) Bradbury, A. G. W.; Sakai, Y.; Shafizadeh, F. A Kinetic Model for Pyrolysis of Cellulose. *J. Appl. Polym. Sci.* **1979**, *23* (11), 3271–3280.
- (54) Maduskar, S.; Teixeira, A. R.; Paulsen, A. D.; Krumm, C.; Mountziaris, T. J.; Fan, W.; Dauenhauer, P. J. Quantitative Carbon Detector (QCD) for Calibration-Free, High-Resolution Characterization of Complex Mixtures. *Lab Chip* **2015**, *15* (2), 440–447.
- (55) Maduskar, S.; Facas, G. G.; Papageorgiou, C.; Williams, C. L.; Dauenhauer, P. J. *Five Rules for Measuring Biomass Pyrolysis Rates: Pulse-Heated Analysis of Solid Reaction Kinetics of Lignocellulosic Biomass*; 2018; Vol. 6.
- (56) Maduskar, S.; Maliekkal, V.; Neurock, M.; Dauenhauer, P. J. On the Yield of Levoglucosan from Cellulose Pyrolysis. *ACS Sustain. Chem. Eng.* **2018**, *6* (5), acssuschemeng.8b00853.

- (57) Bridgwater, A. V. Principles and Practice of Biomass Fast Pyrolysis Processes for Liquids. *J. Anal. Appl. Pyrolysis* **1999**, *51* (1), 3–22.
- (58) Oasmaa, A.; Meier, D. Norms and Standards for Fast Pyrolysis Liquids: 1. Round Robin Test. *J. Anal. Appl. Pyrolysis* **2005**, *73* (2), 323–334.
- (59) Li, H. Q.; Jiku, F.; Schröder, H. F. Assessment of the Pollutant Elimination Efficiency by Gas Chromatography/mass Spectrometry, Liquid Chromatography-Mass Spectrometry and -Tandem Mass Spectrometry. Comparison of Conventional and Membrane-Assisted Biological Wastewater Treatment Processes. In *Journal of Chromatography A*; 2000; Vol. 889, pp 155–176.
- (60) Heberer, T. Occurrence, Fate, and Removal of Pharmaceutical Residues in the Aquatic Environment: A Review of Recent Research Data. *Toxicology Letters*. 2002, pp 5–17.
- (61) Van De Weghe, H.; Vanermen, G.; Gemoets, J.; Lookman, R.; Bertels, D. Application of Comprehensive Two-Dimensional Gas Chromatography for the Assessment of Oil Contaminated Soils. *J. Chromatogr. A* **2006**, *1137* (1), 91–100.
- (62) Booth, A. M.; Sutton, P. A.; Lewis, C. A.; Lewis, A. C.; Scarlett, A.; Chau, W.; Widdows, J.; Rowland, S. J. Unresolved Complex Mixtures of Aromatic Hydrocarbons: Thousands of Overlooked Persistent, Bioaccumulative, and Toxic Contaminants in Mussels. *Environ. Sci. Technol.* **2007**, *41* (2), 457–464.
- (63) Melbye, A. G.; Brakstad, O. G.; Hokstad, J. N.; Gregersen, I. K.; Hansen, B. H.; Booth, A. M.; Rowland, S. J.; Tollefsen, K. E. Chemical and Toxicological Characterization of an Unresolved Complex Mixture-Rich Biodegraded Crude Oil. *Environ. Toxicol. Chem.* **2009**, *28* (9), 1815–1824.
- (64) Gordon, B. M.; Uhrig, M. S.; Borgerding, M. F.; Chung, H. L.; Coleman 3rd, W. M.; Elder Jr., J. F.; Giles, J. A.; Moore, D. S.; Rix, C. E.; White, E. L. Analysis of Flue-Cured Tobacco Essential Oil by Hyphenated Analytical Techniques. *J Chromatogr Sci* **1988**, *26* (4), 174–180.

- (65) Kersten, S.; Garcia-Perez, M. Recent Developments in Fast Pyrolysis of Ligno-Cellulosic Materials. *Current Opinion in Biotechnology*. 2013, pp 414–420.
- (66) Oasmaa, A.; Czernik, S. Fuel Oil Quality of Biomass Pyrolysis Oils - State of the Art for the End Users. *Energy and Fuels* **1999**, 13 (4), 914–921.
- (67) Mortensen, P. M.; Grunwaldt, J. D.; Jensen, P. A.; Knudsen, K. G.; Jensen, A. D. A Review of Catalytic Upgrading of Bio-Oil to Engine Fuels. *Applied Catalysis A: General*. 2011, pp 1–19.
- (68) Paulsen, A. D.; Mettler, M. S.; Dauenhauer, P. J. The Role of Sample Dimension and Temperature in Cellulose Pyrolysis. *Energy and Fuels* **2013**, 27, 2126–2134.
- (69) Mettler, M. S.; Paulsen, A. D.; Vlachos, D. G.; Dauenhauer, P. J. Tuning Cellulose Pyrolysis Chemistry: Selective Decarbonylation via Catalyst-Impregnated Pyrolysis. *Catal. Sci. Technol.* **2014**.
- (70) Mettler, M. S.; Paulsen, A. D.; Vlachos, D. G.; Dauenhauer, P. J. The Chain Length Effect in Pyrolysis: Bridging the Gap between Glucose and Cellulose. *Green Chem.* **2012**, 14, 1284.
- (71) Watanabe, T.; Kato, K.; Matsumoto, N.; Maeda, T. Development of a Precise Method for the Quantitative Analysis of Hydrocarbons Using Post – Column Reaction Capillary Gas Chromatography with Flame Ionization Detection. *Chromatography* **2006**, 27 (2), 49–55.
- (72) Watanabe, A.; Morita, S.; Ozaki, Y. Temperature-Dependent Changes in Hydrogen Bonds in Cellulose I α Studied by Infrared Spectroscopy in Combination with Perturbation-Correlation Moving-Window Two-Dimensional Correlation Spectroscopy: Comparison with Cellulose I β . *Biomacromolecules* **2007**, 8 (9), 2969–2975.
- (73) Watanabe, T.; Kato, K.; Tsunoda, K. ichi; Maeda, T. Metrological Effectiveness of an Analytical Method for Volatile Organic Compounds Standard Materials Using Post-Column Reaction GC/FID System. *Anal. Chim. Acta* **2008**, 619 (1), 26–29.

- (74) Verga, G. R.; Sironi, A.; Schneider, W.; Frohne, J. C. Selective Determination of Oxygenates in Complex Samples with the O-FID Analyzer. *J. High Resolut. Chromatogr.* **1988**, *11* (3), 248–252.
- (75) Teixeira, A. R.; Mooney, K. G.; Kruger, J. S.; Williams, C. L.; Suszynski, W. J.; Schmidt, L. D.; Schmidt, D. P.; Dauenhauer, P. J. Aerosol Generation by Reactive Boiling Ejection of Molten Cellulose. *Energy Environ. Sci.* **2011**, *4*, 4306.
- (76) Di Blasi, C. Kinetic and Heat Transfer Control in the Slow and Flash Pyrolysis of Solids. *Ind. Eng. Chem. Res.* **1996**, *35* (1), 37–46.
- (77) Lédé, J. Biomass Pyrolysis: Comments on Some Sources of Confusions in the Definitions of Temperatures and Heating Rates. *Energies* **2010**, *3* (4), 886–898.
- (78) Ronsse, F.; Dalluge, D.; Prins, W.; Brown, R. C. Optimization of Platinum Filament Micropyrolyzer for Studying Primary Decomposition in Cellulose Pyrolysis. *J. Anal. Appl. Pyrolysis* **2012**, *95* (June 2015), 247–256.
- (79) Hamilton, L. H.; Ayling, A. B.; Shibaoka, M. A New Experimental Device for Pyrolysing Coal Particles under Controlled Conditions over a Wide Range of Heating Rates. *Fuel* **1979**, *58* (12), 873–876.
- (80) Zhu, C.; Krumm, C.; Facas, G. G.; Neurock, M.; Dauenhauer, P. J. Energetics of Cellulose and Cyclodextrin Glycosidic Bond Cleavage. *React. Chem. Eng.* **2017**, *2* (2), 201–214.
- (81) Ojha, D. K.; Vijju, D.; Vinu, R. Fast Pyrolysis Kinetics of Alkali Lignin: Evaluation of Apparent Rate Parameters and Product Time Evolution. *Bioresour. Technol.* **2017**, *241*, 142–151.
- (82) Frontier Laboratories Ltd. *Double-Shot Pyrolyzer PY-2020iD, Operation Manual*.
- (83) Sluiter, J.; Sluiter, A. Summative Mass Closure: Laboratory Analytical Procedure (LAP) Review and Integration: Feedstocks; Issue Date: April 2010; Revision Date: July 2011 (Version 07-08-2011). *Nrel L.* **2010**, *2011* (April), 1–10.

- (84) Beach, C. A.; Krumm, C.; Spanjers, C. S.; Maduskar, S.; Jones, A. J.; Dauenhauer, P. J. Quantitative Carbon Detector for Enhanced Detection of Molecules in Foods, Pharmaceuticals, Cosmetics, Flavors, and Fuels. *Analyst* **2016**, *141* (5), 1627–1632.
- (85) Zhu, C.; Maduskar, S.; Paulsen, A. D.; Dauenhauer, P. J. Alkaline-Earth-Metal-Catalyzed Thin-Film Pyrolysis of Cellulose. *ChemCatChem* **2016**, *8* (4), 818–829.
- (86) Zhou, X.; Nolte, M. W.; Mayes, H. B.; Shanks, B. H.; Broadbelt, L. J. Experimental and Mechanistic Modeling of Fast Pyrolysis of Neat Glucose-Based Carbohydrates. 1. Experiments and Development of a Detailed Mechanistic Model. *Ind. Eng. Chem. Res.* **2014**, *53* (34), 13274–13289.
- (87) Carrier, M.; Auret, L.; Bridgwater, A.; Knoetze, J. H. Using Apparent Activation Energy as a Reactivity Criterion for Biomass Pyrolysis. *Energy and Fuels* **2016**, *30* (10), 7834–7841.
- (88) Cho, J.; Chu, S.; Dauenhauer, P. J.; Huber, G. W. Kinetics and Reaction Chemistry for Slow Pyrolysis of Enzymatic Hydrolysis lignin and Organosolv Extracted Lignin Derived from Maplewood. *Green Chem.* **2012**, *14* (2), 428–439.
- (89) Jauhiainen, J.; Conesa, J. A.; Font, R.; Martín-Gullón, I. Kinetics of the Pyrolysis and Combustion of Olive Oil Solid Waste. *J. Anal. Appl. Pyrolysis* **2004**, *72* (1), 9–15.
- (90) Gašparovič, L.; Koreňová, Z.; Jelemenský, L. Kinetic Study of Wood Chips Decomposition by TGA. *Chem. Pap.* **2010**, *64* (2), 174–181.
- (91) Grønli, M. G.; Várhegyi, G.; Di Blasi, C. Thermogravimetric Analysis and Devolatilization Kinetics of Wood. *Ind. Eng. Chem. Res.* **2002**, *41* (17), 4201–4208.
- (92) Layton, D. S.; Ajjarapu, A.; Choi, D. W.; Jarboe, L. R. Engineering Ethanologenic *Escherichia Coli* for Levoglucosan Utilization. *Bioresour. Technol.* **2011**, *102* (17), 8318–8322.

- (93) He, J.; Huang, K.; Barnett, K. J.; Krishna, S. H.; Alonso, D. M.; Brentzel, Z. J.; Burt, S. P.; Walker, T.; Banholzer, W. F.; Maravelias, C. T.; et al. New Catalytic Strategies for A, ω -Diols Production from Lignocellulosic Biomass. *Faraday Discuss.* **2017**.
- (94) Galletti, P.; Moretti, F.; Samorì, C.; Tagliavini, E. Enzymatic Acylation of Levoglucosan in Acetonitrile and Ionic Liquids. *Green Chem.* **2007**, 9 (9), 987.
- (95) Longley, C. J.; Fung, D. P. C. Potential Applications and Markets for Biomass-Derived Levoglucosan. In *Advances in Thermochemical Biomass Conversion*; Bridgwater, A. V, Ed.; Springer Netherlands: Dordrecht, 1993; pp 1484–1494.
- (96) Pictet, A.; Sarasin, J. Sur La Distillation de La Cellulose et de L'amidon Sous Pression Réduite. *Helv. Chim. Acta* **1918**, 1 (1), 87–96.
- (97) Ivanov, V. I.; Golova, O. P.; Pakhomov, A. M. Main Direction of Reaction in the Thermal Decomposition of Cellulose in a Vacuum. *Bull. Acad. Sci. USSR Div. Chem. Sci.* **1956**, 5 (10), 1295–1296.
- (98) Shafizadeh, F. Introduction to Pyrolysis of Biomass. *J. Anal. Appl. Pyrolysis* **1982**, 3 (4), 283–305.
- (99) Zhuang, X. L.; Zhang, H. X.; Yang, J. Z.; Qi, H. Y. Preparation of Levoglucosan by Pyrolysis of Cellulose and Its Citric Acid Fermentation. *Bioresour. Technol.* **2001**, 79 (1), 63–66.
- (100) Westerhof, R. J. M.; Oudenhoven, S. R. G.; Marathe, P. S.; Engelen, M.; Garcia-Perez, M.; Wang, Z.; Kersten, S. R. A. The Interplay between Chemistry and Heat/mass Transfer during the Fast Pyrolysis of Cellulose. *React. Chem. Eng.* **2016**, 1 (5), 555–566.
- (101) Kwon, G. J.; Kim, D. Y.; Kimura, S.; Kuga, S. Rapid-Cooling, Continuous-Feed Pyrolyzer for Biomass Processing. Preparation of Levoglucosan from Cellulose and Starch. *J. Anal. Appl. Pyrolysis* **2007**, 80 (1), 1–5.

- (102) Proano-Aviles, J.; Lindstrom, J. K.; Johnston, P. A.; Brown, R. C. Heat and Mass Transfer Effects in a Furnace-Based Micropyrolyzer. *Energy Technol.* **2017**, 5 (1), 189–195.
- (103) Patwardhan, P. R.; Satrio, J. a.; Brown, R. C.; Shanks, B. H. Influence of Inorganic Salts on the Primary Pyrolysis Products of Cellulose. *Bioresour. Technol.* **2010**, 101 (12), 4646–4655.
- (104) Zhang, J.; Nolte, M. W.; Shanks, B. H. Investigation of Primary Reactions and Secondary Effects from the Pyrolysis of Different Celluloses. *ACS Sustain. Chem. Eng.* **2014**, 2 (12), 2820–2830.
- (105) Zhang, B.; Leng, E.; Wang, P.; Gong, X.; Zhang, J.; Zhang, Y.; Xu, M. Effect of Reducing Ends on the Pyrolysis Characteristics and Product Distribution of Cellulose. *J. Anal. Appl. Pyrolysis* **2015**, 114 (MAY 2015), 119–126.
- (106) Dobeles, G.; Rossinskaja, G.; Telysheva, G.; Meier, D.; Radtke, S.; Faix, O. Levoglucosenone - A Product of Catalytic Fast Pyrolysis of Cellulose. In *Progress in Thermochemical Biomass Conversion*; 2008; pp 1500–1508.
- (107) Julien, S.; Chornet, E.; Overend, R. P. Influence of Acid Pretreatment (H₂SO₄, HCl, HNO₃) on Reaction Selectivity in the Vacuum Pyrolysis of Cellulose. *J. Anal. Appl. Pyrolysis* **1993**, 27 (1), 25–43.
- (108) Fabbri, D.; Torri, C.; Baravelli, V. Effect of Zeolites and Nanopowder Metal Oxides on the Distribution of Chiral Anhydrosugars Evolved from Pyrolysis of Cellulose: An Analytical Study. *J. Anal. Appl. Pyrolysis* **2007**, 80 (1), 24–29.
- (109) Byrne, G. A.; Gardiner, D.; Holmes, F. H. The Pyrolysis of Cellulose and the Action of Flame-Retardants. *J. Appl. Chem.* **2007**, 16 (3), 81–88.
- (110) Maduskar, S.; Facas, G. G.; Papageorgiou, C.; Williams, C. L.; Dauenhauer, P. J. Five Rules for Measuring Biomass Pyrolysis Rates: Pulse-Heated Analysis of Solid Reaction Kinetics of Lignocellulosic Biomass. *ACS Sustain. Chem. Eng.* **2018**, 6 (1), 1387–1399.

- (111) Lédé, J.; Li, H. Z.; Villermaux, J.; Martin, H. Fusion-like Behaviour of Wood Pyrolysis. In *Journal of Analytical and Applied Pyrolysis*; 1987; Vol. 10, pp 291–308.
- (112) Paulsen, A. D.; Hough, B. R.; Williams, C. L.; Teixeira, A. R.; Schwartz, D. T.; Pfaendtner, J.; Dauenhauer, P. J. Fast Pyrolysis of Wood for Biofuels: Spatiotemporally Resolved Diffuse Reflectance Insitu Spectroscopy of Particles. *ChemSusChem* **2014**, 7 (3), 765–776.
- (113) Nishiyama, Y.; Sugiyama, J.; Chanzy, H.; Langan, P. Crystal Structure and Hydrogen Bonding System in Cellulose I α from Synchrotron X-Ray and Neutron Fiber Diffraction. *J. Am. Chem. Soc.* **2003**, 125 (47), 14300–14306.
- (114) Langan, P.; Nishiyama, Y.; Chanzy, H. X-Ray Structure of Mercerized Cellulose II at 1 Å Resolution. *Biomacromolecules* **2001**, 2 (2), 410–416.
- (115) Nishiyama, Y.; Langan, P.; Chanzy, H. Crystal Structure and Hydrogen-Bonding System in Cellulose I β from Synchrotron X-Ray and Neutron Fiber Diffraction. *J. Am. Chem. Soc.* **2002**, 124 (31), 9074–9082.
- (116) Park, S.; Baker, J. O.; Himmel, M. E.; Parilla, P. A.; Johnson, D. K. Cellulose Crystallinity Index: Measurement Techniques and Their Impact on Interpreting Cellulase Performance. *Biotechnol. Biofuels* **2010**, 3, 1–10.
- (117) Katō, K. Pyrolysis of Cellulose. *Agric. Biol. Chem.* **1967**, 31 (6), 657–663.
- (118) Wang, Z.; Pecha, B.; Westerhof, R. J. M.; Kersten, S. R. A.; Li, C. Z.; McDonald, A. G.; Garcia-Perez, M. Effect of Cellulose Crystallinity on Solid/liquid Phase Reactions Responsible for the Formation of Carbonaceous Residues during Pyrolysis. *Ind. Eng. Chem. Res.* **2014**, 53 (8), 2940–2955.
- (119) Wang, Z.; McDonald, A. G.; Westerhof, R. J. M.; Kersten, S. R. A.; Cuba-Torres, C. M.; Ha, S.; Pecha, B.; Garcia-Perez, M. Effect of Cellulose Crystallinity on the Formation of a Liquid Intermediate and on Product Distribution during Pyrolysis. *J. Anal. Appl. Pyrolysis* **2013**, 100, 56–66.

- (120) Mukarakate, C.; Mittal, A.; Ciesielski, P. N.; Budhi, S.; Thompson, L.; Iisa, K.; Nimlos, M. R.; Donohoe, B. S. Influence of Crystal Allomorph and Crystallinity on the Products and Behavior of Cellulose during Fast Pyrolysis. *ACS Sustain. Chem. Eng.* **2016**, *4* (9), 4662–4674.
- (121) Segal, L.; Creely, J. J.; Martin, A. E.; Conrad, C. M. An Empirical Method for Estimating the Degree of Crystallinity of Native Cellulose Using the X-Ray Diffractometer. *Text. Res. J.* **1959**, *29* (10), 786–794.
- (122) Watanabe, A.; Morita, S.; Ozaki, Y. Study on Temperature-Dependent Changes in Hydrogen Bonds in Cellulose I β by Infrared Spectroscopy with Perturbation-Correlation Moving-Window Two-Dimensional Correlation Spectroscopy. *Biomacromolecules* **2006**, *7* (11), 3164–3170.
- (123) Matthews, J. F.; Bergenstr hle, M.; Beckham, G. T.; Himmel, M. E.; Nimlos, M. R.; Brady, J. W.; Crowley, M. F. High-Temperature Behavior of Cellulose I. *J. Phys. Chem. B* **2011**, *115* (10), 2155–2166.
- (124) Agarwal, V.; Huber, G. W.; Conner, W. C.; Auerbach, S. M. Simulating Infrared Spectra and Hydrogen Bonding in Cellulose I β at Elevated Temperatures. *J. Chem. Phys.* **2011**, *135* (13), 0–13.
- (125) Zhang, X.; Yang, W.; Blasiak, W. Thermal Decomposition Mechanism of Levoglucosan during Cellulose Pyrolysis. *J. Anal. Appl. Pyrolysis* **2012**, *96*, 110–119.
- (126) Ronsse, F.; Bai, X.; Prins, W.; Brown, R. C. Secondary Reactions of Levoglucosan and Char in the Fast Pyrolysis of Cellulose. *Environ. Prog. Sustain. Energy* **2012**, *31* (2), 256–260.
- (127) Kawamoto, H.; Murayama, M.; Saka, S. Pyrolysis Behavior of Levoglucosan as an Intermediate in Cellulose Pyrolysis: Polymerization into Polysaccharide as a Key Reaction to Carbonized Product Formation. *J. Wood Sci.* **2003**, *49* (5), 469–473.
- (128) Seshadri, V.; Westmoreland, P. R. Roles of Hydroxyls in the Noncatalytic and

- Catalyzed Formation of Levoglucosan from Glucose. *Catal. Today* **2016**, 269, 110–121.
- (129) Seshadri, V.; Westmoreland, P. R. Concerted Reactions and Mechanism of Glucose Pyrolysis and Implications for Cellulose Kinetics. *J. Phys. Chem. A* **2012**, 116 (49), 11997–12013.
- (130) Hosoya, T.; Nakao, Y.; Sato, H.; Kawamoto, H.; Sakaki, S. Thermal Degradation of Methyl β -D-Glucoside. A Theoretical Study of Plausible Reaction Mechanisms. *J. Org. Chem.* **2009**, 74 (17), 6891–6894.
- (131) Alexander, L.; Hoyt, C.; Michalczyk, R.; Wu, R.; Thorn, D. L.; Silks, L. A. P. Gram-Scale Synthesis and Efficient Purification of ^{13}C -Labeled Levoglucosan from ^{13}C Glucose. *J. Label. Compd. Radiopharm.* **2013**, 56 (1), 27–29.
- (132) Tanaka, T.; Huang, W. C.; Noguchi, M.; Kobayashi, A.; Shoda, S. ichiro. Direct Synthesis of 1,6-Anhydro Sugars from Unprotected Glycopyranoses by Using 2-Chloro-1,3-Dimethylimidazolinium Chloride. *Tetrahedron Lett.* **2009**, 50 (18), 2154–2157.
- (133) Teixeira, A. R.; Gantt, R.; Joseph, K. E.; Maduskar, S.; Paulsen, A. D.; Krumm, C.; Zhu, C.; Dauenhauer, P. J. Spontaneous Aerosol Ejection: Origin of Inorganic Particles in Biomass Pyrolysis. *ChemSusChem* **2016**, 9 (11), 1322–1328.
- (134) Degenstein, J. C.; Hurt, M.; Murria, P.; Easton, M.; Choudhari, H.; Yang, L.; Riedeman, J.; Carlsen, M. S.; Nash, J. J.; Agrawal, R.; et al. Mass Spectrometric Studies of Fast Pyrolysis of Cellulose. *Eur. J. Mass Spectrom.* **2015**, 21 (3).
- (135) Zhang, B.; Leng, E.; Wang, Y.; Gong, X.; Zhang, Y.; Xu, M. Characterization of Water-Soluble Intermediates and Solid Residues from Fast Pyrolysis of Cellulose in a Wire-Mesh Reactor. *BioResources* **2017**.
- (136) Mettler, M. S.; Paulsen, A. D.; Vlachos, D. G.; Dauenhauer, P. J. Pyrolytic Conversion of Cellulose to Fuels: Levoglucosan Deoxygenation via Elimination and Cyclization within Molten Biomass. *Energy Environ. Sci.* **2012**, 5 (7), 7864.

- (137) Ponder, G. R.; Richards, G. N.; Stevenson, T. T. Influence of Linkage Position and Orientation in Pyrolysis of Polysaccharides: A Study of Several Glucans. *J. Anal. Appl. Pyrolysis* **1992**, 22 (3), 217–229.
- (138) Zugenmaier, P.; Sarko, A. Packing Analysis of Carbohydrates and Polysaccharides. II. B-amylase. *Biopolymers* **1973**, 12 (2), 435–444.
- (139) Finkenstadt, V. L.; Millane, R. P. Crystal Structure of Valonia Cellulose I Beta. *Macromolecules* **1998**, 31 (22), 7776–7783.
- (140) Nishiyama, Y.; Sugiyama, J.; Chanzy, H.; Langan, P. Crystal Structure and Hydrogen Bonding System in Cellulose I(alpha) from Synchrotron X-Ray and Neutron Fiber Diffraction. *J. Am. Chem. Soc.* **2003**, 125 (47), 14300–14306.
- (141) Langan, P.; Sukumar, N.; Nishiyama, Y.; Chanzy, H. Synchrotron X-Ray Structures of Cellulose I β and Regenerated Cellulose II at Ambient Temperature and 100 K. *Cellulose* **2005**, 12 (6), 551–562.
- (142) Nishiyama, Y.; Johnson, G. P.; French, A. D.; Forsyth, V. T.; Langan, P.; Langan, P. Neutron Crystallography , Molecular Dynamics , and Quantum Mechanics Studies of the Nature of Hydrogen Bonding in Cellulose I Neutron Crystallography , Molecular Dynamics , and Quantum Cellulose I. *Biomacromolecules* **2008**, 9 (11), 3133–3140.
- (143) VanderHart, D. L.; Atalla, R. H. Studies of Microstructure in Native Celluloses Using Solid-State ^{13}C NMR. *Macromolecules* **1984**, 17 (8), 1465–1472.